LBL--14262

DE83 016109

PION PRODUCTION AT 180° IN NUCLEUS-NUCLEUS COLLISIONS

Stephen Alan Chessin
(Ph.D. Thesis)

Lawrence Berkeley Laboratory
University of California
Berkeley, California 94720

May 1983

DISCLAIMER

This report was prepared as an account of work sponsored by an agency of the United States Government. Neither the United States Government nor any agency thereof, nor any of their employees, makes any warranty, express or implied, or assumes any legal liability or responsibility for the accuracy, completeness, or usefulness of any information, apparatus, product, or process disclosed, or represents that its use would not infringe privately owned rights. Reference herein to any specific commercial product, process, or service by trade name, trademark, manufacturer, or otherwise does not necessarily constitute or imply its endorsement, recommendation, or favoring by the United States Government or any agency thereof. The views and opinions of authors expressed herein do not necessarily state or reflect those of the United States Government or any agency thereof.

The United States Department of Energy has the right to use this thesis for any purpose whatsoever including the right to reproduce all or any part thereof.

Pion Production at 180° in Nucleus-Nucleus Collisions

Copyright © 1983

by

Stephen Alan Chessin

The Government reserves for itself and others acting on its behalf a royalty free, nonexclusive, irrevocable, world-wide license for governmental purposes to publish, distribute, translate, duplicate, exhibit, and perform any such data copyrighted by the contractor.

TABLE OF CONTENTS

Chapter I: INTRODUCTION 1

Chapter II: *THEORY AND PHENOMENOLOGY* 6

A. Kinematics 6

B. Models 8

B.1. Hard Scattering Models 8

B.1.a. Schmidt and Blankenbecler 10

B.1.b. Landau and Gyulassy 11

B.1.c. Wong and Blankenbecler 13

B.1.d. Quasi-Two-Body Scaling 14

B.2. Statistical Models 16

B.2.a. Firestreak 17

B.2.b. Bohrmann and Knoll 20

B.2.c. Meng Ta-Chung 24

Chapter III: METHOD 30

A. Primary Beam 30

B. Targets 31

C. Beam Flux Monitor 32

D. Spectrometer 33

E. Particle ID 35

F. Electronics and Computer 36

G. Running Plan 37

Chapter IV: DATA ANALYSIS 39

Chapter V: RESULTS 42

A. Systematics 42

B. Comparison With Other Data 51

C. Comparison With Models 52

C.1. Schmidt and Blankenbecler 52

C.2. Landau and Gyulassy 52

C.3. Wong and Blankenbecler 53

C.4. Quasi-Two-Body Scaling 54

C.5. Firestreak and Rows-on-Rows 55

C.6. Meng Ta-Chung 55

D. Kaon Search 56

Chapter VI: SUMMARY AND CONCLUSIONS 59

A. Systematics 59

A.1. T_0 Energy Dependence 59

A.2. AB Dependence of $d\sigma/d\Omega$ 60

A.3. Mock-up Implications 60

B. Model Comparisons 61

C. Future Work 62

Appendix A: OTHER TARGETS 64

REFERENCES 66

LIST OF TABLES 72

TABLES 74

LIST OF FIGURES 119

FIGURES 123

ACKNOWLEDGMENTS

While the one hundred or so pages that follow are the product of my own hand, the work they represents is by no means the result of the efforts of a single individual. Many people worked on the experiment on which this dissertation is based, and I wish to thank them here.

First and foremost I want to thank my advisor, Lee Schroeder, for his trust, guidance, and infinite patience. It has been a long seven years since he first said to me, "We need a spectrometer to look at backward pions. Go design one." Without his support, I never would have made it.

Jorge Geaga wrote the data acquisition and analysis programs and did much of the electronics. Kay Kinoshita and Gloria Lascowich assisted with the data analysis. Jean-Yves Grossiord, John Harris, Dave Hendrie, Bob Treuhaft, Karl Van Bibber, Craig Wuest, and Arthur Zinger all helped staff the data-taking shifts.

I also want to thank those that provided support of a different kind. Carol Morrison and Amy Schoenenberger of the University of California, Berkeley, Counseling Center led a dissertation group that helped me get through the most difficult period. William Goldman provided similar assistance. And I am grateful to Leonora Sea, Allison Hershey, and Carla Woodworth for their love and support during various portions of my career as a graduate student.

Finally, I thank the IBM Corporation for indulging my request for a nine-year leave of absence to pursue a Ph.D. in physics.

This work was supported by the Director, Office of Energy Research, Division of Nuclear Physics of the Office of High Energy and Nuclear Physics of the

U.S. Department of Energy under Contract Number DE-AC03-76SF00098.

ABSTRACT

Pion Production at 180° in Nucleus-Nucleus Collisions

by

Stephen Alan Chessin

A survey experiment of pion production at 180° in nucleus-nucleus collisions is presented. Beams of 1.05 GeV/A and 2.1 GeV/A protons, alphas, and carbon were used, as well as proton beams of 0.80 GeV, 3.5 GeV, and 4.89 GeV, and argon beams of 1.05 GeV/A and 1.83 GeV/A. This is the first such experiment to use the heavier beams. Targets used ranged from carbon to lead. An in-depth review of the literature, both experimental and theoretical, is also presented. The systematics of the data are discussed, and comparisons are made both with prior experiments and with the predictions of the models reviewed. The cross sections appear consistent with a simple single nucleon-nucleon collision picture, without the need for collective or other exotic effects. Suggestions for future work are made.

CHAPTER I

INTRODUCTION

This dissertation is a report of a survey experiment of charged pion production in the backward direction (180°). As Table I indicates, various combinations of beam energy, beam type, and target species were used. This allowed for a systematic study of the dependence of pion production on these parameters. A search for positive kaons was also made and results of that search will be reported.

The production of pions in nuclear collisions has long been used as a probe into the nature of the nuclear force. Unlike the nuclear fragments produced in a collision (i.e., protons, deuterons, and heavier fragments), pions do not exist in the nucleus prior to the collision, but must be created in the collision process. Thus they provide a different perspective into nuclear dynamics than the production of nuclear fragments. For example, pion production can give insight into the existence of clusters or collective effects in the nucleus[1]. As kinematics puts a strict upper limit on the energy of a pion produced in a simple nucleon-nucleon (N-N) collision, observation of pions with energies greater than the N-N kinematic limit may indicate the presence of such clusters.

Three reasons make it interesting to concentrate one's study of pion production on the backward direction. Firstly, the backward direction provides a cleaner environment for observing high-energy pions than does the forward direction. In the center of mass system in which the pion is created, and assuming isotropy, it will of course go forward or backward with equal likelihood. When transformed into the laboratory frame, however, the high energy of

the collision throws everything forward to such an extent that the forward-going pions have to compete with other beam fragments (and unscattered beam) for detection. In contrast, there is a lot less clutter in the backward direction to interfere with the detection of high-energy pions. As these high-energy pions may indicate the collective effects mentioned above, the usefulness of the backward direction becomes apparent.

Secondly, it is easier to study the effects of large A-values (A is the number of nucleons in the nucleus) on pion production in the backward direction. In the regime of limiting fragmentation, forward-going pions are projectile-related whereas backward-going ones are target-related. As heavier targets are presently more accessible than heavy projectiles, effects due to large A-values, such as clustering, can be more easily studied in the (heavier) target fragmentation region, and in particular, in the backward direction.

Thirdly, certain models[1c,2] that were developed to explain forward pion production also make predictions for the backward direction. These can be tested by looking at the backward-going high-energy pions measured in this experiment.

Up until the time of the present work, most of the experiments on pions had looked only at forward pion production[3]. Those that looked at backward production had not used projectiles heavier than alphas[4, 5]. As this experiment was the first to use beams with $A>4$, it provided not only the first possibility for studying the effects mentioned above, it also allowed for the opportunity to explore any systematic dependence on the A-value of the beam.

Previous experiments of interest that helped motivate the present work have been those of Baldin, *et al.*[4], and Papp, *et al.*[3]. Also of interest is the earlier work of Cochran, *et al.*[6]. I will briefly describe their experiments and

findings below. The interested reader is encouraged to consult the original references.

Baldin, *et al.*, studied the process $\begin{bmatrix}p\\d\end{bmatrix}+A\rightarrow\pi^{\pm}(180^{\circ})+X$ for 5.1 and 7.5 GeV protons, and 3.4 GeV/A deuterons, corresponding to momenta of 6 and 8.4 GeV/c for the protons, and 8.4 GeV/c for the deuterons. They observed backward-going pions with energies up to four times greater than the free N-N kinematic limit, and claimed that this gave evidence for collective effects. Figure 1(a)-1(d) shows their data for π^- production from 8.4 GeV/c protons. The invariant cross section is plotted as a function of the pion laboratory kinetic energy. The arrows indicate the maximum allowed pion kinetic energy for a free N-N collision. Pions are clearly produced well beyond this value. Figure 1(e) shows the results of a fit to the cross section R of the form $R=R_1A^n$. The exponent n is plotted against T/T_{max}, the pion kinetic energy divided by the free N-N kinematic limit. The fit goes as $A^{2/3}$ for low-energy pions, and changes smoothly to about $A^{1.1}$ for pions with energies greater than the free N-N kinematic limit. This may indicate that low-energy pions are produced from the surface of the nucleus, whereas higher-energy ones are associated with the interior.

Cochran, *et al.*[6], did a survey experiment of pion production by low-energy (730 MeV) protons on various nuclei (from H to Th) at laboratory angles ranging from 15° to 150°. For pion production from hydrogen, they found their data to be in good agreement with a one-pion-exchange model dominated by the Δ resonance[7]. Their carbon data could be fit by a Monte Carlo calculation of an internucleon cascade process[8] in which the initial pion is produced via a "free" N-N interaction, and then is followed along on its way out of the nucleus, allowing for rescattering, energy loss, and absorption. Using a similar model,

Sternheim and Silbar[9] were able to fit the heavier-target data. Their calculations also included charge-exchange effects, which become more important as the number of nucleons increase. It should be noted that the energies of the pions emitted from the heavier nuclei were also well above the corresponding N-N kinematic limit.

Papp, *et al.*[3], investigated forward pion production (ϑ_{lab}=2.5°) using many beams, at differing energies, on a variety of targets. Of particular importance was the observation of scaling when the invariant cross-section ($E\frac{d^3\sigma}{dp^3}$) was plotted against the scaling parameter $z' = \frac{k_\parallel^*}{(k_\parallel^*)_{max}}$, where $k_\parallel^*$ is the longitudinal momentum of the pion as measured in the projectile/target center of mass system. (The longitudinal momentum is that component of the momentum that is parallel to the beam direction.) A model developed by Schmidt and Blankenbecler[2], referred to as SB and to be discussed later, not only predicted the scaling seen by Papp, it even predicted the form of that scaling. Figure 2 shows the data for the reactions $\begin{pmatrix} p \\ d \\ \alpha \end{pmatrix} + C \rightarrow \pi^-(2.5°) + X$ with the prediction of SB superimposed. The agreement is amazingly good. Would the same results, namely, scaling by z and fit by SB's prediction, be seen in the backward direction?

Thus we find many reasons for measuring pion production at 180°. At low energies (Cochran data), pion production in the backward direction from nuclei is consistent with single N-N scattering, whereas at higher energies (Baldin data) there seem to be indications of collective effects. This raises the question, at what energy does the transition from single scattering to clusters take place? We also see some indication, from Baldin's A-dependence, that perhaps different mechanisms are responsible for producing pions of low and high energy, as well. Finally, the amazing success of SB's model in the forward

direction, combined with its similar predictions for the backward direction, practically begs for testing with an experiment in the backward direction.

CHAPTER II

THEORY AND PHENOMENOLOGY

A. Kinematics

Before discussing the data and the various models pertaining to it, it is necessary to explain which variables are most useful in that discussion.

This experiment measured cross sections for reactions of the form $a+b \to c+$anything. Two forms for the cross section that seem most useful in discussing the data are the Lorentz invariant cross section, $\left[\frac{E}{p^2}\right]\frac{d^2\sigma_{ab}^c}{d\Omega dp}(s,\mathbf{p})$, and the laboratory frame cross section, $\frac{d^2\sigma_{ab}^c}{d\Omega dp}(s,\mathbf{p})$. In both cases, the cross section is a function of the beam and target particles a and b, the total center of mass energy $\sqrt{s}$, and the produced fragment c and its momentum $\mathbf{p}$.

The laboratory cross section is useful because it is directly derivable from the raw data. If N_a beam particles are incident on a target containing n_b target nuclei per unit area, and N_c particles of type c are produced into a phase space volume $\Delta\Omega\Delta p$, then the laboratory cross section is

$$\frac{d^2\sigma_{ab}^c}{d\Omega dp} = \frac{N_c}{N_a}\cdot\frac{1}{n_b}\cdot\frac{1}{\Delta\Omega\Delta p}. \tag{1}$$

As the spectrometer directly selects the momentum of the observed fragments, the natural units for the data are $\frac{d^2\sigma_{ab}^c}{d\Omega dp}$ versus p. In this experiment we only measured particles produced at 180°, so that $p=|\mathbf{p}|$.

Another way to present the data is as $\left[\frac{E}{p^2}\right]\frac{d^2\sigma^c_{ab}}{d\Omega dp}$ versus T_π, the kinetic energy of the pion as measured in the laboratory frame. Although it may seem strange to plot an invariant quantity against a non-invariant one, a little reflection will show the usefulness of this approach. Consider the target nucleus to contain a gas of pions, all in thermal equilibrium with each other. They will then be distributed in phase space according to the Boltzmann distribution, that is, proportional to $e^{-\varepsilon/kT}$, where ε is the energy of any particular pion, k is the Boltzmann constant, and T is the temperature of the pion gas. Since the invariant cross section is proportional to the number of pions populating a region of Lorentz invariant phase space, if the cross section falls off exponentially with the pion energy, then the parameter describing the fall-off can be associated with the temperature of the target during the collision. To be technically accurate, this concept of temperature is only meaningful if the pions are being produced isotropically in the frame in which the energy is defined, that is, in the rest frame of their source. As we only look at 180° pions, we cannot guarantee that this condition is met. Instead, we will assume that the backward pions are representative of those pions produced from a source at rest with respect to the target, at least in the context where temperature is being discussed[10].

Finally, we will find various scaling variables, such as $x'_{ab} = \frac{k^*_\parallel}{(k^*_\parallel)_{max}}$, useful as well, where $k^*_\parallel$ is the longitudinal momentum of the pion in the ab center of mass system, and the subscript "max" represents the maximum value allowed for that variable by kinematics. This parameter scales the pion momentum by the maximum value allowed, and thus collapses the momentum scale onto the range $-1 \le x' \le 1$ independent of the energy available in the collision. Scaling

parameters can be useful in obtaining insight into the dynamics of the collision by stressing important concepts over irrelevant ones. For example, if the data were found to scale by x', (that is, if the cross section plots all had the same shape, or all fell on the same curve, when plotted against x'), that would indicate that the relative momentum of the pion is more relevant than its absolute value. Additionally, certain models predict scaling by different parameters, even when they don't predict absolute magnitudes for the cross sections. Thus scaling parameters are helpful in testing these models.

B. Models

Many models and theories have been developed in the attempt to understand nuclear collisions. I will only discuss those models that are relevant to pion production in the backward direction. For a good review of the state of the art in relativistic nuclear collision theory, see Ref. [11] and references therein.

The models I want to discuss generally fall into two categories: hard scattering models, and statistical models.

B.1. Hard Scattering Models

Hard scattering models assume that one nucleon in the projectile nucleus interacts with one nucleon in the target nucleus, producing the pion in a single hard collision. Figure 3(a) is a generalized Feynman diagram for this process. The amplitude ψ_A (ψ_B) refers to finding an off-shell nucleon a (b) within A (B); $T_{ab\pi x}$ is the off-shell scattering matrix for the reaction $a+b\rightarrow\pi+x$; and Ω represents distortions due to final state interactions[12].

Hard scattering models make two assumptions in order to simplify the calculations. First, they neglect final state interactions. These interactions mix

incoherent processes of higher order with the first order coherent ones (see Fig. 3). When models are written to include the distortions to the wave function caused by final state interactions, they generally use the optical model to calculate the distorted waves. This implies that, *after* the collision, the nucleus is still around to distort the wave function, a somewhat questionable assumption. While a rigorous handling of final state interactions is possible, it is messy and therefore usually not done[13]. Although this simplifies the calculations, it also draws into question the validity, or at least the proper interpretation, of any results. For example, Amado and Woloshyn[14] argue that, at low momentum transfer, final state interactions are as important as the primary interaction and exactly cancel the first order effect.

Secondly, in the absence of a detailed field theory, the scattering matrix $T_{ab\pi x}$ is evaluated as if it were on-shell; that is, the particles a and b are treated as if they were on the mass shell $p_0=(\mathbf{p}^2+M^2)^{1/2}$, and the off-shell rates are related to the on-shell rates by taking $s=(p_a+p_b)^2$. The symbols p_a and p_b are four-vectors; three-vectors are denoted as $\mathbf{p}$.

With these assumptions, the diagram in Fig. 3(a) simplifies to that of Fig. 3(b). The hard scattering models then become more phenomenological tools than actual theories, but nonetheless they aid in discerning possible important physical effects in the study of nuclear collisions.

Mathematically, the cross section R is given by hard scattering models as:

$$R(B+A\to\pi+X) \propto \int \frac{d^3a}{\varepsilon(\mathbf{a})}\frac{d^3b}{\varepsilon(\mathbf{b})} G_A(\mathbf{a})G_B(\mathbf{b})R(a+b\to\pi+x;s',t',u')P \qquad (2)$$

where $G_A(\mathbf{a})$ is the pseudo-probability for finding a nucleon with momentum $\mathbf{a}$ and energy $\varepsilon(\mathbf{a})$ in the frame of the A nucleus (corresponding to the amplitude ψ_A), and similarly for $G_B(\mathbf{b})$. P is the phase space factor, and limits the domain

of the a, b integrations so only kinematically-allowed pions are produced in the sub-process.

Hard scattering models thus provide a framework in which to examine the momentum distribution of the nucleons in the nucleus. The differences between various hard scattering models lie in their specific choices for $G_A(a)$ and $G_B(b)$, their parameterization of the $a+b\to\pi+x$ rate, and the kinematic region where P is non-zero.

B.1.a. Schmidt and Blankenbecler

Schmidt and Blankenbecler (SB)[2,12] developed their hard scattering model by assuming that high-energy pions are produced in a nuclear collision *only* when the nucleon involved in the collision (a or b in the diagram) carries a high internal momentum, and the $A-1$ ($B-1$) remaining nucleons recoil coherently and share the recoil momentum equally among themselves. Figure 4(a) represents this process.

With this and other assumptions, SB were able to derive simple counting rules that give the form of the G factors to be $(1-x'_{AB})^{2T(A-a)-1}$ (and similarly for b), where T = 1, 2, or 3 depending upon the model used for the elementary nucleon-nucleon interaction, and x'_{AB} is the scaling variable discussed above. When SB compared their model to the data of Papp, *et al.*[3], they discovered that T=3 gave the best fit. This value corresponds to the nucleon-nucleon interaction being mediated by the exchange of vector mesons, such as ρ's and ω's, and is also the same result one would get by counting quarks. The model thus predicts that the cross section for the reaction

$$B+A\to\pi\begin{pmatrix}180^\circ\\0^\circ\end{pmatrix}+X \tag{3}$$

should go as $(1-x'_{AB})^S$, where

$$S = \begin{cases} 6B-3-2\delta_{A,1} & \text{for } 0^\circ \text{ (projectile fragmentation), and} \\ 6A-3-2\delta_{B,1} & \text{for } 180^\circ \text{ (target fragmentation)} \end{cases} \tag{4}$$

(δ is the Kronecker delta function, and accounts for the fact that a proton beam or target has no internal motion).

Although one of the assumptions of this model implies that it is only good for predicting the shape of the high-energy pion spectrum (that is, near $x' \approx 1$), we saw in Fig. 2 that it fits the low-energy pions as well.

B.1.b. Landau and Gyulassy

As we shall see later, the SB model failed to fit the early results of this experiment, that is, the proton-induced pion spectra[15]. It also failed to fit the data of Baldin, *et al.*[4(a)], and the data of Cochran, *et al.*[6], as analyzed by Landau[16]. This prompted Landau and Gyulassy (LG)[12] to introduce two modifications into the hard scattering model of SB.

First, instead of sharing the recoil momentum (**p** or **k**) equally among the $A-1$ residual nucleons, the LG cluster model has the recoil momentum shared coherently by $c-1$ nucleons, with $1 \le c \le A$, and the remaining $A-c$ nucleons acting as spectators. This situation is described by Fig. 4(b). Here we are just discussing the target fragmentation case, where the incoming projectile hard scatters off a target cluster. For projectile fragmentation one interchanges A and B in this discussion. The cluster c is treated as if it were at rest with respect to the target A; this is called a "frozen" cluster by LG. Then the model of SB is assumed to hold when applied to the Bc subsystem:

$$R[B+A(c) \to \pi(180^\circ)+X] \propto (1-x'_{Bc})^{S_{Bc}}, \tag{5}$$

$$S_{Bc} = 6c-3-2\delta_{B,1} \tag{6}$$

for target fragmentation, and

$$R[B(c)+A\to\pi(0^\circ)+X]\propto(1-x'_{cA})^{S_{Ac}} \tag{7}$$

for projectile fragmentation, where S_{Ac} is given by Eq. (6) with $A\leftrightarrow B$.

Note that c, the number of particles in the cluster, is an important parameter in this model, as it determines both what center of mass system to use when evaluating $k_\parallel^*$, and the value of $(k_\parallel^*)_{max}$, and therefore affects the value of x' that corresponds to each laboratory momentum.

The second modification of LG was to allow the cluster to have some internal motion with respect to the nucleus. They introduce phenomenological pseudo-probability distributions $\rho_c(\mathbf{p})$ to describe the motion of the cluster within the nucleus. These distributions are phenomenological since they are not calculated from any theory, and pseudo-probabilistic because of the neglect of final state interactions. Restricting the folding to just the z-axis, they obtain:

$$\begin{aligned} R[B+A(c)\to\pi(180^\circ)+X]\propto&\int_{-\infty}^{\infty}dp_z\rho_c(p_z)[1-x'_{Bc}(x'_{BA})]^{S_{Bc}}\\ &\times\{\vartheta(1-\mathcal{E}[B,A(c)])\vartheta(\mathcal{E}[B,A(c)]-x'_{BA})\}\\ =&\int_{p_{max}}^{p_{min}}dp_z\rho_c(p_z)[1-x'_{Bc}(x'_{BA})]^{S_{Bc}}. \end{aligned} \tag{8}$$

As the integration is done in the laboratory frame, x'_{Bc} is written as a function of x'_{BA} to indicate that a Lorentz transformation is needed. Since now $0\le x'_{Bc}\le 1$, the maximum value of x'_{BA} is given by $\mathcal{E}[B,A(c)]\equiv x'_{BA}(x'_{Bc}=1)$. The first ϑ function in the integral represents conservation of energy, in that it prevents a pion from being created with a larger momentum than allowed by kinematics in the BA frame, and thus determines the maximum cluster momentum p_{max}. The second ϑ function enforces $x'_{Bc}\le 1$ and determines the minimum cluster momentum p_{min}.

LG choose two forms for $\rho(p_z)$, an exponential and a Gaussian. Comparison of their model with the data will be presented later.

B.1.c. Wong and Blankenbecler

Prompted by the work of Landau and Gyulassy, Wong and Blankenbecler[17] derived a new scaling formula for hard scattering. They re-examined the SB model, and found that the counting rules were really only valid for very energetic collisions, that is, when the rest masses of the nuclei can be neglected[18]. As LG[12] had explained, the success of the counting rules in the forward direction was the result of kinematical effects. They therefore undertook a closer examination of the six-fold integral (Eq. (2)) and found that for both target and projectile fragmentation the integrand is strongly peaked when a and b are near the mass shell. Expanding (for target fragmentation) about the point $x=b/B$, $b_T=a_T=0$, they determined that the cross section Eq. (2) is predominately a function of π_T and x_H, where x_H is the lower limit of the a-integration and is given by:

$$x_H = \frac{\gamma^2+\sqrt{\gamma^4-a^2(u'+C_T^2)}}{u'+C_T^2}\left[\frac{m_b(B_0-B_Z)}{m_B(A_0-A_Z)} - \frac{C_0-C_Z}{A_0-A_Z}\right] \tag{9}$$

where

$$\begin{aligned}\gamma^2&=(d^2-a^2-u')/2,\\ u'&=(m_b B/m_B-C)^2,\end{aligned} \tag{10}$$

and where a, b, A, and B refer to the objects indicated in Fig. 3(a), C refers to the pion, d (corresponding to x in the figure) is the minimum mass of the $(a+b)$ combination (taken to be the mass of the deuteron), and m_i is the mass of particle i. To obtain x_H for forward pion production, one performs the following interchanges: $C_z \leftrightarrow -C_z$, $a \leftrightarrow b$, $A_0 \leftrightarrow B_0$, $A_z \leftrightarrow -B_z$, $m_a \leftrightarrow m_b$, and $m_A \leftrightarrow m_B$.

Although this derivation is more rigorous than the original SB model, it is less transparent. As a result, the scaling variable it derives, x_H, does not yield easily to direct physical interpretation.

B.1.d. Quasi-Two-Body Scaling

Quasi-two-body scaling (QTBS), although a hard scattering model, was derived in a different fashion than the hard scattering models discussed above. Originally developed to explain backward proton production[19], it was extended to pion production by Perdrisat, *et al.*[5].

The reasoning behind QTBS is as follows[19,5] (see Fig. 5). As backward production of nucleons is forbidden in free nucleon-nucleon collisions, backward production in nucleus-nucleus collisions can be attributed to the internal motion of the nucleons. The assumptions made (similar to the assumptions of the hard scattering formalism) are (Fig. 5(a)):

(1) The observed backward particle is a constituent of the target;

(2) The observed particle was freed from the target in a single, low-momentum-transfer interaction;

(3) No large momentum transfer occurred to the rest of the target;

(4) Final state interactions can be ignored.

With these assumptions, the argument is made that the observed momentum $\mathbf{q}$ cannot be too different from the internal momentum $\mathbf{k}$ of the target nucleon. As the probability of finding a nucleon with momentum $\mathbf{k}$ falls off rapidly with increasing k, one expects the process to be dominated by the smallest k possible, k_{min} (Fig. 5(b)). Since $\mathbf{p}+\mathbf{k}=\mathbf{q}+\mathbf{p}'$, or (as $\mathbf{p}$ and $\mathbf{q}$ are fixed) $\mathbf{p}-\mathbf{q}=\mathbf{p}'-\mathbf{k}$, the smallest k comes when $\mathbf{k}\|\mathbf{p}'$. This gives $|k_{min}|=|\mathbf{p}-\mathbf{q}|-|\mathbf{p}'|$. (Note that $-\mathbf{k}$ is also the recoil momentum of the residual $(A-1)$ target nucleus,

and that $\mathbf{p}'$ is the projectile momentum after the collision.) Defining $P = |\mathbf{p}-\mathbf{q}| = |\mathbf{p}'-\mathbf{k}|$, and $\varepsilon = E_p - E_q + m_A = E_{p'} + E_k$, we get that

$$k_{\min} = \frac{1}{2(\varepsilon^2 - P^2)}\{P(\varepsilon^2 - P^2 - m^2 + M^2) - \varepsilon[(\varepsilon^2 - P^2 - m^2 - M^2)^2 + 4m^2M^2]^{1/2}\}. \tag{11}$$

Here m is the nucleon mass and M is the invariant mass of the target residual, $M^2 = E_k^2$. Note that $k_{\min}$ is smallest when M is smallest, that is, when $M = m_{A-1}$.

Frankel had originally argued[19(b)] that the cross section $d^3\sigma/dq^3$ could be factored into a part C proportional to the elementary interaction with a nucleon of momentum $k_{\min}$, and a part depending on the probability of finding a nucleon in the nucleus of momentum $k_{\min}$. He then obtained $d^3\sigma/dq^3 = C(p,k_{\min})G(k_{\min})/|\mathbf{p}-\mathbf{q}|$, where C varies slowly with $k_{\min}$ and $G(k_{\min}) = \int F(k)kdk$ evaluated at $k = k_{\min}$, where $F(k)$ is the internal momentum distribution. Thus one would expect plots of $|\mathbf{p}-\mathbf{q}|d^3\sigma/dq^3$ vs $k_{\min}$ to scale. However, Amado and Woloshyn[14,19(c)] pointed out that two of the assumptions used in the derivation of QTBS, namely that both final state interactions and the excitation of the target can be neglected, are invalid, and that QTBS works just from kinematics as long as 1) the detected fragment is indeed from the target, and 2) the recoil momentum $-\mathbf{k}$ is distributed over many particles in the residual target, not just one. Frankel then responded[19(d)] by rigorously re-deriving QTBS, and producing the *same formalism* as before, but with the following re-interpretation: The vector $\mathbf{k}$ is not now ascribable to an internal nucleon, but is just the recoil of the residual target. $C(p,k_{\min})$ is proportional to the *measured* p-p cross section, and not derivable from first principles as originally done by Woloshyn for Frankel[20]. $G(k_{\min})$ still appears in the formalism, but now it has little, if any, relation to the actual internal momentum distribution.

Be that as it may, the extension of QTBS to pion production is done in two steps. First, the case $p+A\rightarrow\pi+X$ is examined (Fig. 5(c)). It is clear that Eq. (11) still applies, except that in this case p' is the residual momentum of the two-nucleon system, and so corresponds to its invariant mass. Again, the smallest possible k_{min} results when m is as small as possible.

In the second step, the projectile is allowed to be a nucleus of B nucleons (Fig. 5(d)). Now p' is the momentum of the $B+1$ system, and m becomes m_{B+1}. In the calculation of k_{min}, the smallest m_{A-1} and m_{B+1} are used.

LG[12] relate QTBS to their cluster model previously described.

B.2. Statistical Models

Whereas the hard scattering models assume that each nucleon in the projectile or target interacts with at most one other nucleon, producing a pion in a single hard collision, the statistical models assume that the pions are generated as a result of collisions between groups of nucleons. Also, the hard scattering models focus on the internal momentum distribution, while the statistical models are more concerned with the numbers of interacting nucleons. Statistical models factor the pion cross section into two parts: one part determined by geometry, and the other part determined by the dynamics of the interaction. The geometrical part is related to the impact parameter of the collision, which determines how many nucleons from the target and the projectile participate in the interaction. The dynamical part determines the momentum distribution of the produced particles, given the energy and mass of the participants. The way these two parts are specified differentiates the different statistical models.

B.2.a. Firestreak

The firestreak model[21] is a descendant of an earlier model, the fireball model[22]. In the fireball model, the nuclei are treated as sharply defined spheres that sweep out cylindrical cuts in each other (see Fig. 6(a)). The nuclear matter in the overlap region quickly reaches thermal equilibrium and expands until it reaches a critical density ρ_c (also known as the freeze-out density), at which point the nucleons cease interacting with each other and the final particle momentum distributions are fixed.

With two major changes the fireball model becomes the firestreak model. Firstly, instead of thermalization proceeding across the entire overlapping volume, the overlap region is considered to be made up of infinitesimal parallel streaks (see Fig. 6(b)), each of which thermalizes independently from the others. The second major change is that instead of being sharply defined spheres, the nuclei are assumed to have diffuse surfaces.

Mathematically, the firestreak model can be expressed thusly:

$$F_j(\mathbf{p})=\int 2\pi b\,db \int\int dx\,dy\, w_b(x,y) f_j(\mathbf{p};M,\beta). \tag{12}$$

$F_j(\mathbf{p})$ is the Lorentz-invariant momentum space density for particles of type j. The inner integral is for a given impact parameter b; $w_b(x,y)$ is the combined target-projectile density projected onto the x,y plane perpendicular to the beam (the geometrical part of the model) and $f_j(\mathbf{p};M,\beta)$ is the Lorentz-invariant momentum space density for particles of type j emitted by a system (the streak) of mass M and velocity β in the laboratory frame (the dynamical part of the model). The coordinates x,y determine the location of the streak; the values of M and β obviously depend on x and y. The distribution w is a function of the impact parameter b; hence the outer integral over all impact parameters.

Letting N_P and N_T represent the amount of material contributed to the streak by the projectile and target, respectively, one can define the parameter $\eta = N_P/(N_P+N_T)$ as the fraction of the streak that comes from the projectile. This η is also a function of x and y, and uniquely determines M and β, given the projectile and target types and the projectile energy. This parameterization allows one to separate the integrals in Eq. (12) as follows:

$$F_j(\mathbf{p}) = \sum_{i=1}^{M} Y(\eta_i) f_j[\mathbf{p}; M(\eta_i), \beta(\eta_i)]$$
$$Y(\eta_i) = \int_{\eta_i - \Delta\eta/2}^{\eta_i + \Delta\eta/2} d\eta' \int 2\pi b\, db \int\int dx\, dy\, w_b(x,y)\, \delta[\eta' - \eta_b(x,y)] \tag{13}$$

where the yield function $Y(\eta_i)$ contains all the geometry. Thus the η range can be conveniently divided into equally-sized intervals, and the yield functions can be tabulated separately. Once the yield functions have been tabulated for a given target-beam combination, different values of the dynamical function f_j can be easily tested.

The diffuse density distributions, which go into the computation of w, have the form

$$\rho(r) = \rho_0 \begin{cases} \left[1 - \left(1 + \frac{R}{a}\right) e^{-R/a} \frac{\sinh(r/a)}{r/a}\right], & r \le R \\ \left[\frac{R}{a}\cosh(R/a) - \sinh(R/a)\right] \frac{e^{-r/a}}{r/a}, & r \ge R \end{cases} \tag{14}$$

where $R = 1.18A^{1/3}$ and $a = \sqrt{1/2}$.

The dynamical functions f_j determine the phase space distributions of the produced particles by assuming thermodynamic equilibrium between all the particles at the freeze-out density ρ_c. It contains two parts, one pertaining to the equilibrium of the final state particles, and one due to the two-body decay of resonances which are themselves in thermal equilibrium at the time of

freeze-out:

$$f_j = f_{1,j} + f_{2,j}. \tag{15}$$

Since f_j is a Lorentz-invariant quantity, it can be evaluated in any frame. This evaluation is easiest in the center of mass frame of the streak, where

$$f_j[\mathbf{p}; M(\eta_i), \beta(\eta_i)] = f_j[\mathbf{p}'; M(\eta_i), 0] = E' \frac{d^3 N_j}{d\mathbf{p}'^3} \tag{16}$$

and primed quantities are measured in the streak center of mass.

The thermal part is

$$f_{1,j}(\mathbf{p}') = E' \frac{(2S_j+1)}{(2\pi)^3} V \left[\exp\left(\frac{E' - \mu_j}{T} \right) \pm 1 \right]^{-1} \tag{17}$$

where $E' = (p'^2 + m_j^2)^{1/2}$ is the total energy of the particle, m_j is its mass, S_j its spin, and μ_j its chemical potential. V and T are the volume and temperature, respectively, of the system at the freeze-out density, and the + or − sign indicates a fermion or boson, respectively.

The two-body decay part is

$$f_{2,j}(\mathbf{p}') = \sum_R \frac{W_D (2S_R+1) V m_R T^2}{16\pi^3 p' p_D} \left[\frac{\mu_R}{T} \ln(1+e^{-x}) + \sum_{n=1}^{\infty} \frac{(\mp)^{n+1}}{n^2} e^{-nx} (nx+1) \right]_{x_-}^{x_+} \tag{18}$$

where

$$x_\pm = \left[\frac{m_R}{m_j^2} (E' E_D \pm p' p_D) - \mu_R \right] / T \tag{19}$$

and m_R, S_R, and μ_R are the mass, spin, and chemical potential of the resonance, E' and p' refer to the energy and momentum of the resonance as measured in the streak center of mass, and E_D and p_D refer to the decay total energy and momentum of the particle of type j in the resonance rest frame.

All the chemical potentials can be expressed in terms of the chemical potentials of the neutron and proton (for example, $p+n \leftrightarrow n+n+\pi^+$ implies $\mu_{\pi^+}=\mu_p-\mu_n$, and $n+n+p \leftrightarrow n+d$ implies $\mu_d=\mu_n+\mu_p$); thus the problem that remains involves solving a system of thermodynamic equations for μ_n, μ_p, and T. The only variable parameter in the model is the freeze-out density ρ_c, which indirectly determines the freeze-out volume V. From a calculational standpoint, another parameter is the number of resonances used in the summation in Eq. (18).

In their calculations, Gosset, *et al.*[21b] used resonances (meaning both N^* and Δ, and excited nuclei) up to mass 5. They also found that varying ρ_c over a reasonable range of values did not change the shapes of the spectra, only their normalizations. In no case could they simultaneously normalize the curves of the different particles to match the data of Gosset, *et al.*[22b]. They chose a value of $\rho_c=0.12\pm0.02$ hadrons/fm^3 which resulted in the curves for p, d, t, and ^{3}He all being too low by a factor of 2. The spectra for ^{4}He were then low by a factor of 4, which they attributed to the $A=5$ cutoff in the resonance calculations.

While the baryonic spectra are all too low, the pionic predictions are too high. Figures 7(a)-7(d) compare the data of Nagamiya, *et al.*[23] and Nakai, *et al.*[24] for high- and low-energy pions, respectively, with the firestreak model. The firestreak predictions in Figs. 7(c) and 7(d) have been multiplied by 1/2.

Comparison of the the firestreak model with the data of this experiment will be presented later.

B.2.b. Bohrmann and Knoll

Although Bohrmann and Knoll (BK) originally developed their model[25] to describe only nucleon spectra, they later extended that model to include pion

production[26]. The basic premises of this later model are that each nucleon interacts with a limited number of other nucleons, and that, subject to conservation laws, the final momentum distributions of the nucleons and created pions fill all available phase space uniformly. Thus the single particle inclusive cross section is an incoherent sum of contributions from different groups of interacting nucleons:

$$\varepsilon \frac{d^3\sigma}{dp^3} = \sum_{M,N} \sigma_{AB}(M,N) F_{MN}(\mathbf{p}) \tag{20}$$

where ε and $\mathbf{p}$ refer to the total energy and momentum of the observed particle: $\varepsilon=\sqrt{m^2+\mathbf{p}^2}$. The contribution from each group of nucleons (M from projectile A, N from target B) can be factored into its formation cross section $\sigma_{AB}(M,N)$ (the geometrical part), and the normalized momentum distribution $F_{MN}(\mathbf{p})$ for producing a pion with momentum $\mathbf{p}$ from $M+N$ nucleons (the dynamical part).

Equation (20) is of course general; the model becomes specific in its choice of σ and F. BK define $\sigma_{AB}(M,N)$ as the cross section for finding exactly M nucleons from A and N nucleons from B inside a tube aligned parallel to the beam direction and with cross-sectional area equal to the total nucleon-nucleon cross section. $F_{MN}(\mathbf{p})$ is defined in reference to the following equations:

$$
\begin{aligned}
F_{MN}(\mathbf{p}) &= \sum_m m P_{MNm}(s)\varphi^1_{MNm}(\mathbf{p}) \\
P_{MNm}(s) &= \frac{\Lambda_{MNm}}{\sum_m \Lambda_{MNm}} \\
\varphi^1_K &= \int \frac{d^3p_2}{\varepsilon_2} \cdots \frac{d^3p_K}{\varepsilon_K}\, \varphi_K(\mathbf{p}_1 \cdots \mathbf{p}_K) \\
\varphi_K(\mathbf{p}_1 \cdots \mathbf{p}_K) &= \delta\left[\sum_{i=1}^{K} \varepsilon_i - E\right]\delta^3\left[\sum_{i=1}^{K} \mathbf{p}_i - \mathbf{P}\right] / I_K(s) \\
I_K(s) &= \int \frac{d^3p_2}{\varepsilon_2} \cdots \frac{d^3p_K}{\varepsilon_K}\, \delta\left[\sum_{i=1}^{K} \varepsilon_i - \sqrt{s}\right]\delta^3\left[\sum_{i=1}^{K} \mathbf{p}_i\right] \\
\Lambda_{MNm} &= \left[\frac{V}{(2\pi\hbar)^3}\right]^{M+N+m-1} \varepsilon_n^{M+N}\varepsilon_n^{m} I_{MNm}(s)\, dE\, 2^{2(M+N)} 3^m .
\end{aligned}
\tag{21}
$$

P_{MNm} is the probability for producing exactly m pions from a system of $M+N$ nucleons at center of mass energy $\sqrt{s}$. It is proportional to Λ_{MNm}, which is the number of states available to the $M+N+m$ particles at energy $\sqrt{s}$, subject to conservation laws. This is the same approach used by Fermi in his statistical model of pion production in nucleon-nucleon collisions[27].

$\varphi^1_{MNm}(\mathbf{p})$ is the one-particle Lorentz-invariant momentum distribution, obtained by integrating $\varphi_{MNm}(\mathbf{p}_1 \cdots \mathbf{p}_K)$, the multi-particle momentum distribution ($K=M+N+m$), over all but one pion momentum. $I_K(s)$ is the normalization factor, E and $\mathbf{P}$ are the total energy and momentum available to the system, and $s = E^2 - \mathbf{P}^2$ is the square of the invariant mass.

The only free parameter in the model is the coordinate space volume V that appears in the expression for Λ_{MNm}, the number of states available to the $M+N+m$ system. This volume can be expressed as a density ρ_c when related to the number of nucleons ($M+N$) occupying the volume. The statistical nature of the model comes from the definition of φ_k and of Λ_{MNm}, both of which are basically phase space parameters.

This model differs from the firestreak model[21] described above in that the firestreak model treats each independently interacting group of nucleons as bulk matter—temperature, volume, and chemical potential are the important quantities, while momentum and energy are conserved only on the average. In the finite particle number model, each tube of nucleons retains the character of a collection of nucleons and pions—the energy and momentum are shared by all the particles in an equilibrated fashion, but conservation laws are obeyed at each possible point in phase space, and not just on the average. One would thus expect the models to differ in their results in kinematic regions near the edge of available phase space.

The purpose of the BK model is to study the effect of finite particle numbers on the pion spectra; hence they compare their results not with the full firestreak model, but with a "firestreak simulation", obtained by replacing the expression for F with

$$F_{\ell N}^{bulk}(\mathbf{p})=\lim_{\alpha\to\infty}\frac{m_\ell}{\alpha}\,P_{\alpha\ell\alpha Nm}\,\varphi_{\ell Nm}^{1}(\mathbf{p}). \tag{22}$$

This bulk limit differs from the actual firestreak model in that it ignores isospin (charge conservation) and delta resonances.

To compare their model with data, BK choose a value of $\rho_c=2\rho_0$ (where ρ_0 is the normal nuclear density, 0.16 fm^{-3}) in order to fit the pion multiplicity data of Sandoval, *et al.*[28], for beam energies around 1 GeV. Figure 8(a) is a comparison of their model with the data of Lemaire, *et al.*[29]. It shows that their model tends to reproduce the slopes of the data but not the actual normalizations. Figure 8(b) shows the proton-induced data of Papp, *et al.*[3], which technically cannot be handled by a firestreak model, as the assumptions of the firestreak model make no sense for a single-nucleon participant. Note that the firestreak simulation runs into trouble near the kinematic limit, as

expected (Fig. 8(b)).

B.2.c. Meng Ta-Chung

The model of Meng Ta-chung[30] differs from the previous statistical models in that it does not predict the shapes of the cross sections; instead, it uses the statistical line of reasoning (factorization of the cross section) to predict certain patterns the data should follow. Also, whereas the previous statistical models assume that the backward pions are produced when the overlapping regions merge into a single object (what Meng calls a violent collision), Meng's model assumes that they are produced only in gentle collisions, where the overlapping regions just pass through each other while retaining their individual identities.

Meng presents a single physical picture[31] for discussing both nucleon-nucleus and nucleus-nucleus collisions, and is able to derive some interesting (and testable) predictions from this picture[30].

The basic assumptions of Meng's model are[30(a)]:

(1) The time needed for the formation of multi-body final states in nucleon-nucleon collisions is long compared to the traversal time of a relativistic nucleon through a nucleus. Thus, in a nucleon-nucleus collision, the nucleons in the path of the projectile can be viewed as acting collectively, and to f. . order can be considered as a single object, called an effective target ($E^{\prime\prime}$).

(2) The nucleon-ET interaction can be described by the same picture[32] used to describe a nucleon-nucleon interaction. This picture divides collisions into two types: gentle, where the two (spatially extended) objects pass through and excite each other, then fragment separately; and violent,

where the two objects stop each other and form a conglomerate which expands, reaches a critical volume, and decays. Gentle processes are associated with large impact parameters (peripheral collisions), while violent processes tend to be associated with more central collisions.

(3) The mass of the *ET* is proportional to its average "thickness", that is, to the average number of nucleons in the path of the incident nucleon. Meng defines $M_{ET}=\nu_{ET}M$, where M_{ET} and M are the mass of the *ET* and the nucleon, respectively, and ν_{ET} is the number of nucleons in the *ET*.

(4) Defining the effective projectile (*EP*) in an analogous manner, a high-energy nucleus-nucleus collision can be considered as the simultaneous collision of all possible *EP*-*ET* pairs. As the binding energy per nucleon in each nucleus is small compared to the collision energy, the transverse dimension of the *EP*'s and *ET*'s is that of a single nucleon. This is similar to the rows-on-rows model of Bohrmann and Knoll[26]. Each collision between an *EP* and an *ET* can be either gentle or violent, as described in (2).

(5) In general, a high-energy nucleus-nucleus collision will contain both gentle and violent *EP*-*ET* interactions. To the extent that one or the other type dominates, the collision can be called gentle or violent, respectively.

(6) Since gentle processes are associated with larger impact parameters, nucleus-nucleus fragmentation will most likely take place in a peripheral collision of two nuclei.

Meng notes that the fragmentation products of gentle collisions tend to be confined to the forward and backward regions, whereas the violent collisions will also populate the central angles (as measured in the center of mass)[32]. In particular, pions at 0° and 180° are more likely to be produced in the gentle,

peripheral collisions[30(a), 30(b)]. The violent collisions can be described by a statistical model of Meng's[30(b),32,33] which will not be discussed here. Instead, we will examine in more detail the gentle collision, from the point of view of the target.

Let ε be the beam kinetic energy per nucleon. Then the ET has $E_{proj}^{kin}=\nu_{ET}\varepsilon$ kinetic energy in the projectile frame. After the collision, this energy can either remain as the kinetic energy of the ET, or go into the production and emission of low-mass particles, or go into some combination of the two. The two extremes are (1) the ET retains its original velocity, until it breaks up (isotropically in its rest frame) into single and multi-nucleon fragments, and (2) the ET uses the maximum amount of its kinetic energy in emitting energetic low-mass particles in its direction of motion (the backward direction in the laboratory frame), while it slows down to some minimum velocity. This second process is analogous to bremsstrahlung.

Meng then makes the following points:

1. Since the maximum amount of energy available for producing backward pions is $\nu_{ET}\varepsilon$, the relevant variable to use when comparing energy distributions of pions near $\vartheta_{lab}=180°$ (which is the same as $\vartheta_{proj}=0°$) from collisions involving different targets and/or different beam energies is not e_{lab}^{kin}, the kinetic energy of the pion in the laboratory, but this quantity measured in the projectile frame and scaled by the total amount of kinetic energy available; that is, one should use $u_{proj}=e_{proj}^{kin}/\nu_{ET}\varepsilon$. For forward pions, the relevant variable is $u_{lab}=e_{lab}^{kin}/\nu_{EP}\varepsilon$.

2. As the backward pions are produced from the ET, and not the EP, the inclusive cross section can be factored as follows:

$$\left[\frac{d^3\sigma}{dp^3}\right]_{proj}(A_1,A_2,\varepsilon;\vartheta_{proj}\approx 0,e^{kin}_{proj}) = F_{1\,proj}(A_1)F_{2\,proj}(A_2,\varepsilon;\vartheta_{proj}\approx 0,e^{kin}_{proj}) \tag{23}$$

where F_1 describes the EP and F_2 describes the ET.

Since this is a peripheral process, $F_{2\,proj}$ is proportional to the area a_2 of the ring on the periphery of the nucleus (see Fig. 9(c)). Taking the nucleus to be a sphere in its rest frame, with radius R_2, we get:

$$F_{2\,proj} \propto a_2 = 2\pi(R_2-\Delta R_2/2)\Delta R_2 \tag{24}$$

where ΔR_2 is the depth of the ring.

3. The number ν_{ET} of nucleons in the ET is proportional to the thickness of the ring-shaped object (Fig. 9(d)):

$$\nu_{ET} \propto t_2 = \frac{4}{3}[(2R_2-\Delta R_2)\Delta R_2]^{1/2} = \frac{4}{3}\sqrt{a_2/\pi}\,. \tag{25}$$

4. From 1, 2, and 3 above, we find that we can write

$$F_{2\,proj}(A_2,\varepsilon;\vartheta_{proj}\approx 0,e^{kin}_{proj}) = a_2(A_2)G_2(\varepsilon,e^{kin}_{proj}) \tag{26}$$

where G_2 depends only on the variable $u_{proj}=e^{kin}_{proj}/\nu_{ET}\varepsilon \propto e^{kin}_{proj}/\sqrt{a_2}\varepsilon$. Thus one would expect plots of $(d^3\sigma/dp^3)_{proj}$ vs $e^{kin}_{proj}/\varepsilon$ to scale, for constant beam and target.

By similar arguments, one would expect plots of $(d^3\sigma/dp^3)_{lab}$ vs $e^{kin}_{lab}/\varepsilon$ for forward pions to scale, again for constant beam and target. Figure 10(a), the proton-induced data of Papp, *et al.*[3], is just such a plot.

To check the A_2 dependence given by 4 above, one needs a more specific model. Assuming that the projectile is a sphere of radius

$$R_2 = A_2^{1/3}r_0 \quad (r_0=1.2\text{ fm}) \tag{27}$$

and writing

$$\Delta R_2 = \xi(A_2) r_0, \tag{28}$$

we can write

$$a_2 = \pi r_0^2 s_2 \text{ and } t_2 = \frac{4}{3} r_0 \sqrt{s_2}, \tag{29}$$

where

$$s_2 = (2A_2^{1/3} - \xi)\xi. \tag{30}$$

Thus, according to this model, one would expect plots of $s_2^{-1}(d^3\sigma/dp^3)_{proj}$ vs $e_{proj}^{kin}/\sqrt{s_2}\varepsilon$ to scale, independent of energy and target. Similarly, one would also expect plots of $s_1^{-1}(d^3\sigma/dp^3)_{lab}$ vs $e_{lab}^{kin}/\sqrt{s_1}\varepsilon$ for forward pions to scale, independent of energy and projectile.

The only parameter not yet specified is ξ; Meng uses the *ansatz* $\xi(A)=A^{-1/6}$. A plot of $s_1^{-1}(d^3\sigma/dp^3)_{lab}$ vs $e_{lab}^{kin}/\sqrt{s_1}\varepsilon$ for the data of Papp, *et al.*[3] using this *ansatz* is given in Fig. 10(b).

Similarly, a plot of $s_2^{-1}(d^3\sigma/dp^3)_{proj}$ vs $e_{proj}^{kin}/\sqrt{s_2}\varepsilon$ is given in Figs. 10(c) and 10(d) for the data of Baldin, *et al.*[4(a), 4(b)].

These graphs indicate that Meng's model works very well in both the forward and backward directions, at least for the range of targets, projectiles, and energies considered. It should be noted that, until the present experiment, a broad range of projectile energies had only been used in the forward direction.

Based upon the preliminary results of this experiment[15], Meng observed[30(c)] that the invariant cross section for 180° pions can be expressed as $Ed^3\sigma/dp^3 = C\exp[-e_{lab}^{kin}/T_0(\varepsilon)]$, where T_0 is the slope parameter and depends strongly on ε, while C depends only weakly on ε. From the arguments above, Meng would expect the cross section to go as

$C'\exp[-e^{kin}_{proj}/(\alpha\nu_{ET}\varepsilon)]$, where α is independent of ε and A_T. Equating the two expressions, performing the required Lorentz transformation, and neglecting the pion mass, Meng obtains

$$T_0(\varepsilon)=\alpha\nu_{ET}\,\frac{\varepsilon}{M}[\varepsilon+M-\sqrt{\varepsilon(\varepsilon+2M)}]\underset{\varepsilon\gg 2M}{\overset{\lim}{=}}\frac{\alpha\nu_{ET}M}{2} \tag{31}$$

where M is the nucleon mass. If one does not neglect the pion mass, then Eq. (31) becomes

$$\begin{aligned} T_0(\varepsilon)&=\alpha\nu_{ET}\,\frac{\varepsilon}{M}\left[\varepsilon\left(1+\frac{m_\pi}{e^{kin}_{proj}}\right)+M-\sqrt{\varepsilon(\varepsilon+2M)}\left(1+2\frac{m_\pi}{e^{kin}_{proj}}\right)^{*}\right] \\ &=\alpha\nu_{ET}\,\frac{\varepsilon}{M}\,\frac{\left[\varepsilon\left(1+\frac{m_\pi}{e^{kin}_{lab}}\right)+M-\sqrt{\varepsilon(\varepsilon+2M)}\left(1+2\frac{m_\pi}{e^{kin}_{lab}}\right)^{*}\right]}{1-\frac{m_\pi}{e^{kin}_{lab}}\left[3\frac{\varepsilon}{M}+2\left(\frac{\varepsilon}{M}\right)^2\right]+\left(\frac{m_\pi}{e^{kin}_{lab}}\right)^2\left(\frac{\varepsilon}{M}\right)^2} \end{aligned} \tag{32}$$

which shows that, for less-energetic pions, the exponential parameterization may not be appropriate for this model.

It should be noted that this model does not distinguish between positive and negative pions, whereas the preliminary results[15] of this experiment showed that there were indeed differences. At our urging, Meng examined the origin of π^-/π^+ ratios, and predicted that, for low-energy ($\varepsilon \le 1$GeV) protons on nuclei, $0.09 \le \pi^-/\pi^+ \le 0.19$. As the incident energy increases, the ratio should approach one.

Comparisons of Meng's predictions (concerning scaling, T_0, and π^-/π^+ ratios) with the data will be done in a later section.

CHAPTER III

METHOD

The experiment was performed with a single-arm spectrometer that provided momentum selection, as well as transporting the backward-produced particles through the detection system. The detection system identified particles by their momentum, time-of-flight, and dE/dx. The data were recorded on-line by a PDP-9[34] computer, and the magnetic tapes thus produced were later analyzed off-line.

The experiment was located in beam line 30 in the EPB[35] hall of the Bevatron/Bevalac facility at the Lawrence Berkeley Laboratory. Figure 11(a) is a plan view, and Fig. 11(b) an elevation view, of the experimental setup.

A. Primary Beam

Carbon and argon beams were accelerated to an energy of 3.5 MeV/A by the SuperHILAC, and delivered through a transfer line to the Bevatron for acceleration to final energies. When running in this configuration, the SuperHILAC/Bevatron combination is called the Bevalac. Proton and alpha beams were produced in the Bevatron's own injector, a 20 MeV proton linac which has been modified to also accelerate deuteron, alpha, and carbon beams.

No matter which injector was used, the beams were accelerated to the desired energy in the Bevatron main ring, and delivered by a series of bending and focusing magnets to the experimental cave. A quadrupole doublet (Q1 and Q2 in Fig. 11(a)) was used to produce the final focus of the beam spot on the targets. A small bending magnet (M1S), mounted so that it could be rotated

about the beam axis, provided the ability to make small steering corrections in both the horizontal and vertical directions.

Three multi-wire proportional chambers (30-1WC, 30-2WC, and 30-3WC) were used to monitor the beam position. Each chamber consisted of two planes of 32 wires each; the wires were spaced six millimeters apart in 30-1WC and 30-3WC, and two millimeters apart in 30-2WC[36]. The upstream steering magnets were used to center the beam in 30-1WC, and M1S then used as necessary to center the beam into 30-2WC. Chamber 30-2WC also monitored the focusing of the beam by Q1 and Q2. (As 30-2WC was only about 60 centimeters downstream from the target position, compared to about 9 meters from the quadrupoles, focusing on 30-2WC was sufficient to focus on the target.) During data taking, 30-2WC was connected to the on-line computer to monitor and record the beam spot position and size. The use of 30-3WC is described later.

B. Targets

The standard targets used were two-inch squares of carbon, aluminum, copper, tin, and lead. For certain runs targets of polyethylene (CH_2), deuterated polyethylene (CD_2), and silver were also used. All targets were mounted in a target holder that had space for up to six targets. Normally one target position was left empty so that background runs, referred to as "target-empty" (MT) runs, could be done.

The nominal thickness of the standard and silver targets was one-eighth inch; for the polyethylene targets the nominal thickness was one-quarter inch. Multiple squares of each target were available. The targets mounted in the holder were equipped with pegs in the upper two corners. The extra targets were drilled with matching holes so that they could be slipped onto the pegs and increase the thickness of the target, in steps of the nominal thickness, as

desired.

For studies of the effect of target thickness on the measured cross sections (a method of checking the credibility of the experiment), squares of 1/32" copper and 1/64" aluminum were used. These squares were mounted in the MT position using Scotch tape[37].

The target holder was mounted in a target positioner that allowed for remote selection and positioning of the desired target. An odometer-type dial mounted on the positioner frame, and monitored with a TV camera, indicated the target position. This arrangement permitted the proper target to be moved into the correct location by remote control, so that an experimenter did not have to enter the cave.

C. Beam Flux Monitor

The beam flux was monitored with an ion chamber (IC) placed in the beam; this monitor was checked with two telescopes placed above and below the beam line (MU and MD, respectively, in Fig. 11(b)) aimed to pick up the spray from the ion chamber. Aluminum plates were placed in front of these telescopes to allow only the harder spray to get through. This kept the photo-multiplier tubes from saturating at high beam intensities so that the linear relationship between the integrated current from the ion chamber and the counts from MU and MD could be maintained. The ion chamber was calibrated for each beam/energy combination by doing carbon-11 activation runs[38]: A disk of polystyrene was placed in the target position and exposed to the beam for a measured length of time, and the integrated ion chamber current for this period of time was recorded. Carbon-11 produced in the disk by the passage of the beam through it was then measured in an off-line gamma-ray spectrometer. By applying various corrections for the rate of irradiation, time elapsed between irradiation and

measurement, etc., the total amount of carbon-11 produced could be calculated. Using the known value of the $^{12}C \rightarrow ^{11}C$ cross section for the particular beam and energy, the total number of beam particles passing through the disk could be determined, and compared to the integrated current produced by the ion chamber.

A third telescope (ML) was positioned to one side and slightly downstream of the target, and aimed in the general direction of the targets. By observing the counts in ML while the target was slowly moved across the beam spot, the calibration of the target positioner could be checked. Figure 12 shows the results of such a scan. ML was also used to monitor the beam flux, although the measurements obtained this way were obviously target dependent.

D. Spectrometer

The spectrometer consisted of a dipole magnet, M2, and a quadrupole doublet, Q2/Q3. A second dipole, M3, was used to reduce the background, as will be explained later. M2 momentum-analyzed the backward-going particles, and the quadrupole doublet increased the accepted solid angle of the spectrometer by producing an image of the target at the rear counter. The acceptance of the spectrometer varied somewhat with the momentum selected, but was generally 1 msr in solid angle and ±6% in momentum.

Particles were detected by two scintillation counter telescopes, F1/F2 in the front (between M2 and Q3), and R1/R2 in the back. A coincidence was required between both telescopes. The size of F1 determined the angular acceptance of the spectrometer.

Collimators were placed on either side of the front telescope, just inside the exit of M2 and the entrance to Q3, to reduce the number of particles that might reach the back telescope while missing the front one. The collimators

were disks of lead, one inch thick, with square holes cut in them. The holes were sufficiently large so as not to affect the angular acceptance of the spectrometer. Four disks were used in front of F1 and six were placed behind F2.

The front member of the rear telescope consisted of three segments, labeled R1A, R1B, and R1C. This arrangement permitted three measurements to be made at each setting of the spectrometer. The central momentum detected by R1B was the nominal setting of the spectrometer; R1A and R1C accepted a central momentum that was 12 percent higher or lower, respectively. This also provided a redundancy check for the spectrometer, as cross section measurements would have to be consistent between counters at a single setting, as well as within counters at different settings. The width of each segment determined the momentum acceptance of the spectrometer (about ±6%). The dimensions of the front and rear scintillators are listed in Table II.

On its way to the target the primary beam had to pass through M2, and was thus bent away from the nominal beam line. As the amount of bending depended on the ratio of the beam to detected particle rigidities, a computer program was written to determine the required magnetic field strength and target location as a function of the desired momentum setting.

After passing through the target the non-interacting primary beam, as well as any forward-produced particles, entered M3. With the field in M3 set in the opposite sense of that in M2, M3 steered the beam back towards the beam dump. In addition, any backward-going charged particles produced when the beam later hit the beam dump would be swept out of the acceptance of the spectrometer by M3. This procedure was required to reduce the background of the experiment. Measurements in the target-empty configuration showed a ten-fold reduction in counting rate with M3 on as compared to identical runs

with M3 off. The location at which the beam exited M3 was monitored with 30-3WC.

M2 was calibrated[39] using a computerized mapping system[40]. Q3 and Q4 were calibrated[41] using the technique described in Ref. 41(b). The program OPTIK[42] was used to determine the focusing conditions for the quadrupoles. It was observed that the necessary focal strengths were smoothly varying functions of the spectrometer bend angle, which in turn depended on the ratio of beam to fragment rigidity. These functions were determined and incorporated into the magnet field strength and target location program described above, along with the magnet calibration data, so that a table of magnet currents, their corresponding meter readings, and target positions could be produced prior to each run.

The calibration data and computer program results were verified by wire orbiting[43].

E. Particle ID

Particles were identified by their momentum, their time-of-flight between the front and rear counters, and by the pulse height (dE/dx) measured in the counters. The dE/dx measurement served two purposes. First, it allowed distinction between alphas and deuterons. As alphas have the same charge-to-mass ratio as deuterons, and therefore have the same velocity for the same rigidity, time-of-flight alone is insufficient to separate deuterons from alphas. Since dE/dx, however, depends only on the charge-to-velocity ratio of the fragment ($dE/dx \propto Z^2/\beta^2$), alphas would distinguish themselves by a much greater energy loss than the deuterons. Second, since dE/dx varies inversely to the velocity, and hence directly with the time-of-flight, it provided another data cut that, when used in conjunction with the time-of-flight measurements,

reduced the background considerably. These cuts were of the form

$$C_1<(A\cdot\mathrm{TOF}-B\cdot\mathrm{ADC})<C_2 \tag{33}$$

where A and B are empirically determined from the time-of-flight (TOF) versus pulse height (ADC) scatter plots, and C_1 and C_2 are similarly determined to eliminate the background without eliminating good events. Figure 13 is an example of such a scatter plot that illustrates the value of this cut. The lower cluster of points are pions, and the upper cluster of points are protons. The time-of-flight and pulse height histograms are projected onto the axes. This particular scatter plot is from a 300 MeV/c, long gate run with a 2.1 GeV/A carbon beam and a $\frac{1}{8}$ inch copper target.

F. Electronics and Computer

The electronics were set to trigger on a coincidence between the front and rear counters. (See Fig. 14.) Three different gate configurations were used in the trigger coincidence. In the normal "long gate" configuration, the width of this coincidence was set long enough to allow acceptance of the heavier, slower fragments (protons, deuterons, tritons), as well as lighter fragments with $\beta=1$. A narrower "short gate" trigger was used when measuring low-energy positive pions (100-400 MeV/c) to exclude protons from the data. This shorter gate was also modified to exclude the pions in order to measure the K^+ cross section.

A Digital Equipment Corporation PDP-9 was used to record the data from the experiment. Interfaced to the computer through a CAMAC crate were the time-of-flight time digitizers (TDCs), the dE/dx analog-to-digital converters (ADCs), and various scalars connected to the monitor telescopes, the ion chamber, and the front and back detectors themselves and the various coincidences between them. The scalars were recorded so that they could be used

in determining the dead time of the data acquisition computer, which was done by comparing the counts from the scalars gated on during a spill with those that also had a veto signal from the computer when it was busy. In other words,

$$\text{Dead time} = 1 - \frac{\text{Spill gated scaler}}{(\text{Spill}\cdot\text{Not busy})\ \text{gated scalar}} \tag{34}$$

provided an estimate of the dead time.

Chamber 30-2WC was also connected to the computer to produce a spill-by-spill record of the beam position for use in the analysis, as the actual position of the beam spot, relative to the nominal value, affected the central momentum value for the spectrometer. In addition, many of the scalars were displayed visually for monitoring during the run, and typed out at the end of each data run via an automatic typewriter, for doing real-time diagnostics of the beam conditions and equipment.

G. Running Plan

The procedure for taking data at each beam and energy combination was divided into four phases.

The first phase was beam tune up and ion chamber calibration. The beam spot was focused onto the target plane, and, if not previously done for this beam, a carbon-11 activation run was performed to calibrate the ion chamber. Various checks of the electronics and computer were made, and the equipment readied for data acquisition.

In the second phase, also known as "long gate" running, the magnet polarities were set for positive fragments, and the electronics set for the long trigger coincidence gate previously described. In a typical run, data would be collected at momentum settings from 300 MeV/c to 1 GeV/c in steps of 100 MeV/c, and then in steps of 200 MeV/c until the rate became too low. High-energy pions, as

well as protons, deuterons, and tritons, were detected in the long gate mode.

At each momentum setting, each target, in turn, was positioned in the beam (as determined by the computer program), and data collected for a period of time that depended on the counting rate, generally averaging a few minutes. The "MT" target was also positioned in the beam for background measurements. Additional thicknesses of targets were added as required, to keep the counting rate at a reasonable level.

In the third phase, or "short gate" mode, the electronics were set to exclude triggers from slow particles, and the targets were again cycled through at each momentum setting. A typical momentum sequence in the short gate mode would be 50 to 200 MeV/c in steps of 50 MeV/c, then to 500 MeV/c in steps of 100 MeV/c. Pions generally did not appear until 150 MeV/c or so; at 400 or 500 MeV/c, protons would start to creep into the gate.

For the fourth phase, "negative" running, the magnet polarities were all reversed so that the spectrometer would accept only negative particles. With the electronics set to "long gate", the same momenta as in the "short gate" running were used.

CHAPTER IV

DATA ANALYSIS

The data was analyzed using a two-step procedure. First, a central momentum and a momentum acceptance were calculated for each of the three rear counters at each setting of the spectrometer, taking into consideration the beam spot size and position (that is, deviation from nominal beam center) during that particular run. Time-of-flight cuts were then calculated, based on the momentum acceptance, and applied to the time-of-flight spectra to obtain the yields for pions, protons, deuterons, and tritons in positive-field running, and just pions in negative-field running. Cuts based on dE/dx were applied at the same time to eliminate accidentals.

Yields for a few runs were also obtained by making hand cuts on the time-of-flight versus dE/dx scatter plots. These yields were compared with the computer-generated yields for the same runs. Since good agreement was found between these two methods, and given the volume of data that had to be processed, it was decided to use the computer-generated cuts to extract all the yields.

The computer-generated cuts were also applied to the target-empty runs, to obtain "yields" to be used in the background subtraction.

The second step involved matching each target-in run with its corresponding target-out run, normalizing the target-out yield to the target-in yield by using the ratios of the corresponding ion chamber measurements, and subtracting the normalized target-out yield from the target-in yield. Points with target-in yields of only one or two events were deemed to be "noise" and not

processed. The subtracted yields were then converted into cross sections by using the well known formula:

$$\frac{d\sigma}{d\Omega dp} = \frac{N_y}{N_0 \rho t} \frac{1}{\Delta\Omega\, \Delta p} C \tag{35}$$

where

N_y = subtracted yield,

N_0 = incident beam,

ρ = target density,

t = target thickness,

$\Delta\Omega$ = spectrometer solid angle acceptance,

Δp = spectrometer momentum acceptance,

C = product of various correction factors.

The correction factors included pion decay (based upon the average time-of-flight for that counter), dead time in the electronics, multiple scattering, and absorption. Contamination by electrons turned out not to be a problem, as the electron yields fell off rapidly with momentum, and were essentially zero at momenta where the pion peak and the electron peak would have overlapped ($p_\pi \geq 200$ MeV/c). Energy loss in the target and detectors was calculated and used to adjust the momentum "seen" by the rear detector to that of the pion originally emitted in the target.

The shift in central momentum seen by the counters due to the exponential nature of the cross section was accounted for by doing the acceptance calculation twice. A uniform spectrum was assumed to get the initial value of the cross section. A curve of the form $\exp[-(ap^2+bp+c)]$ was then fit through each set of three points, and the resulting values of the parameters a, b, and c were used to adjust the central momentum. The cross section was then recalculated

using the new values. This technique was found to converge so rapidly that a second iteration was not necessary.

Statistical errors were calculated by assuming that the events detected came from a Poisson distribution; thus the best estimate of the standard deviation of N counts is $\sqrt{N}$. The error on the yield was combined in quadrature with the error on the background, using standard error propagation techniques. These same techniques were used to generate the final statistical uncertainties in the cross sections.

Systematic errors could have resulted from errors in determining the magnet and counter positions, drifts in the magnet currents, drifts in the ion chamber integrator, and inefficiencies in the photo-multiplier tubes. A study was made of the probable magnitude of these effects, and to account for them a factor of seven percent has been folded in, in quadrature, with the statistical errors. These errors are reported with the data.

The above errors account for the point-to-point uncertainty in the data. In addition, there is an overall uncertainty in the normalization of the cross sections estimated to be no more than fifteen percent. This estimate is based on the ion chamber calibration, and should be taken into account when the data from this experiment is compared with that of other experiments.

Multiple scattering and muon contamination effects were simulated using a Monte Carlo method. It was noted that the corrections due to these effects become large, with correspondingly large uncertainties, below 200 MeV/c. Because of this, none of the data below 200 MeV/c will be included in this report.

CHAPTER V

RESULTS

Tables III-XXVI contain the measured pion production cross sections for all of the beams and for the five standard targets (C, Al, Cu, Sn, Pb) used in this experiment. The other targets are discussed in an appendix. All the corrections described in Chapter IV have been applied, and the errors listed correspond to statistical ones.

I will first discuss the systematic characteristics of the data, comparing where appropriate with data of other experiments. Comparisons with the models previously discussed will then be made, followed by the results of the kaon search.

A. Systematics

Figure 15 is a plot of invariant cross section versus kinetic energy for the reaction 2.1 GeV/A C + Cu $\rightarrow \pi^-$ (180°) + X; it is representative of the shape of all the data. The most notable feature of the data is the lack of structure. The invariant cross section falls off exponentially with pion kinetic energy, with no intriguing bumps or peaks.

This is typical of all the spectra observed. Each spectrum can be parametrized by a slope and an amplitude, corresponding to the fit $(E/p^2)d^2\sigma/d\Omega dp = A\exp[-T/T_0]$. For us to glean any information from the data, we must therefore examine how these parameters change as the experimental conditions (incident energy and projectile and target type) change. These parameters are listed in Table XXVII, and are discussed below.

Figure 16 is a plot of T_0 versus T_{beam}/A_{beam}, for protons, alphas, carbon, and argon on copper. For beam energies below 2.1 GeV/A, T_0 rises steadily with beam energy. With the higher energies used with the proton beam, one can begin to see a leveling-off of T_0. This behavior is seen with all targets, and confirms the earlier trend seen by Baldin, *et al.*,[4(a)] which indicates that T_0 appears to reach a limiting value of 60-70 MeV. The data for the heavier beams does not go to high enough beam energy to indicate whether a limiting value is reached in those cases as well; the data that is available, however, is not inconsistent with such a leveling off.

Figure 17 shows the T_0 dependence on beam and target, for a fixed beam energy of 1.05 GeV/A. Although there is some variation from beam to beam and target to target, no strong dependence is seen. At best we can say that the slope parameter, on average, increases slightly with increasing beam or target mass.

The other parameter describing these cross sections is the amplitude. Physically more meaningful, however, is the integrated cross section $d\sigma/d\Omega$ which in this case is defined as

$$\left.\frac{d\sigma}{d\Omega}\right|_{(180°)} = \int_{100\ \mathrm{MeV}}^{600\ \mathrm{MeV}} \frac{d^2\sigma}{d\Omega dT}\, dT. \tag{36}$$

These are also tabulated in Table XXVII. The lower limit of integration represents the lowest energy for pions which are included in this report; the upper limit generally corresponds to the highest observed. Due to the exponential nature of the cross sections, the error introduced by truncating the integration at 600 MeV is in all cases much less than the propagated error from the fit parameters.

Figure 18 shows how the integrated cross sections change with beam energy, for carbon beams on all targets. Although it is obvious that the integrated cross section increases with increasing energy, there are not enough data points to determine the functional form of this dependence.

Before discussing the variation of $d\sigma/d\Omega$ with beam and target mass, it will be helpful to first examine the π^-/π^+ ratios. Tabulated in Table *XXVIII*, and plotted in Fig. 19 as a function of beam energy, are these ratios for all beam and target combinations. For all beams heavier than protons, the π^-/π^+ ratio is consistent with one, although there seems to be a slight increase with increasing energy. The ratios from the argon beam are all slightly (but not significantly) greater than one, as would be expected from the 1.22 neutron-proton ratio in argon.

For the proton-induced pions we see a definite trend—the pion ratios are much less than one at the lower energies, increasing towards one with increasing energy. This energy dependence is consistent with the fact that a proton beam is more likely to produce π^+'s than π^-'s. For example, if we assume that at low energies the pions are produced by the formation and decay of a single Δ resonance, then simple analysis of the Clebsch-Gordan coefficients would predict a π^-/π^+ ratio of 0.1 for an $N=Z$ target. At higher energies, multi-pion production channels would begin to enter, and the π^-/π^+ ratio would be expected to approach one. The increasing fraction of neutrons in heavier targets also plays a part, again pushing the ratio towards one.

An examination of the dependence of the 180° integrated cross sections on beam and target shows an increase with both increasing beam and target mass. Determination of the A,B dependence is important because it helps separate that part of the cross section that is due to the basic nucleon-nucleon interac-

tion from that part which is due to the nucleons acting in concert. For example, a simple $(A^{1/3}+B^{1/3})^n$ dependence would imply that each nucleus acted as a single object, with the cross section dominated by the geometrical probability of a collision. A simple $(AB)^n$ dependence, on the other hand, would indicate a factorization of the cross section in a manner consistent with each nucleon acting independently of all the others. In this second case, the important contribution of a nucleus-nucleus collision is that it increases the probability, based on sheer numbers, that two nucleons will collide.

These represent the two extremes, the former characterizing each nucleus as a "bowl of jelly", and the latter characterizing each nucleus as a "bag of marbles". The integrated cross sections were fit to each of these formulations. Figure 20 shows the results of fitting the 1.05 GeV/A $\rightarrow \pi^+$ data to the "bags of marbles" model. The "bowls of jelly" fit did not produce a single straight line. We see that the integrated cross section exhibits a power-law dependence on the product of the beam and target masses, with a power of 0.80±0.02. This same behavior is seen with the 2.1 GeV/A $\rightarrow \pi^-$ data, except that the power in this case is 0.95±0.02. The cross sections for the 1.05 GeV/A $\rightarrow \pi^-$ and 2.1 GeV/A $\rightarrow \pi^+$ data also increase with the beam mass-target mass product; however, the fit to a power law is not as good as in the first two cases. This is understandable if we remember that the π^-/π^+ ratio is unity except for the proton beam data. Hence one would expect that a good fit to π^- data would not fit the corresponding π^+ data, and vice versa, when protons are included. When we exclude the proton data, the fit to a power law is excellent in all cases, with an exponent of 0.80±0.02 for the 1.05 GeV/A data and 0.95±0.02 for the 2.1 GeV/A data.

When we examine how the *differential* cross sections vary with this product, we see the same power-law dependence at the lower momenta, but not at the higher ones. This is consistent with the integrated cross section data, as the integrated cross sections are dominated by the lower-momentum pions. For example, the power is the same at 200 MeV/c as it is in the integrated case, but increases as the pion momentum increases, reaching a value of about 1.0 for the 1.05 and 2.1 GeV/A π^+ data, and about 1.1 for the π^- data. Also, there appears to be more variation with beam, as the argon beam data falls slightly below the line defined by the alpha and carbon beam data, in the 1.05 GeV/A π^- and π^+ cases at 200 MeV/c. This may indicate a dependence on the isospin of the beam, as both the alpha and carbon beams are of isospin zero, while argon has an isospin of at least two. The data at 500 MeV/c is too sparse for any definite conclusions to be drawn.

There are two more ways of looking at the data that I would like to discuss. The first is (almost) model independent; the second assumes an isobar model for pion production.

In this first approach we try to "build" the cross section for the heavier projectiles out of those produced by the proton beam. For example, one could say that, since projectile B consists of Z_B protons and N_B neutrons, one should be able to write

$$\left[\frac{d^2\sigma}{d\Omega dp}\right]_{B+A\to\pi^+} = Z_B\left[\frac{d^2\sigma}{d\Omega dp}\right]_{p+A\to\pi^+} + N_B\left[\frac{d^2\sigma}{d\Omega dp}\right]_{n+A\to\pi^+} \tag{37}$$

and similarly for the π^- cross sections. This assumes, of course, that single nucleon-nucleon collisions dominate, and that multi-particle effects, such as clustering, Fermi motion in the projectile, etc., are not important.

Since we do not measure the neutron-induced cross sections, we need some way of "faking" them. For an isospin zero target, such as ^{12}C, this is simple:

$$n + {}^{12}C \to \pi^+ \leftrightarrow p + {}^{12}C \to \pi^- . \tag{38}$$

For a non-isospin zero target, such as copper, we must make additional assumptions. Let us assume that the pions are produced singly, in a single nucleon-nucleon interaction, and that once produced, they do not change their identity. This implies that we neglect charge exchange, although effects such as absorption and rescattering in the target (but not in the projectile) are implicitly accounted for in the model. Then the possible reactions are:

$$\begin{aligned} p + p &\to \begin{cases} pp\,\pi^0 \\ pn\,\pi^+ \end{cases} \\ \left.\begin{matrix} p + n \\ n + p \end{matrix}\right\} &\to \begin{cases} pp\,\pi^- \\ pn\,\pi^0 \\ nn\,\pi^+ \end{cases} \\ n + n &\to \begin{cases} nn\,\pi^0 \\ np\,\pi^- . \end{cases} \end{aligned} \tag{39}$$

From this we see that it is only the protons in the target that would contribute to the neutron-induced pi-plus production. Since $n + p \to \pi^+ \leftrightarrow p + n \to \pi^-$, we mock up the neutron-induced cross section by equating

$$\left[\frac{d^2\sigma}{d\Omega dp}\right]_{n+A\to\pi^+} = \frac{Z_A}{N_A}\left[\frac{d^2\sigma}{d\Omega dp}\right]_{p+A\to\pi^-} . \tag{40}$$

Substituting into Eq. (37), we obtain

$$\left[\frac{d^2\sigma}{d\Omega dp}\right]_{B+A\to\pi^+} = Z_B\left[\frac{d^2\sigma}{d\Omega dp}\right]_{p+A\to\pi^+} + N_B\,\frac{Z_A}{N_A}\left[\frac{d^2\sigma}{d\Omega dp}\right]_{p+A\to\pi^-} . \tag{41}$$

Since, of the targets used, only aluminum is naturally a single isotope, a

weighted average of the naturally occurring isotopes was used[44].

Note that this procedure will not work to mock up π^- cross sections, as both neutrons *and* protons contribute to the neutron-induced π^- production. Without resorting to some dynamical model, there is no way to differentiate between the two contributions.

Figure 21 shows a comparison of this mock-up with the data for the 1.05 GeV/A alpha and argon beams, and for the 2.1 GeV/A alpha beam. Four trends are clear: The mock-up fits the lower-energy beams better than it does the higher-energy ones; the mock-up tends to overpredict the lower-momentum pions; this overprediction is greater with heavier projectiles; and the mock-up fits heavier targets better than lighter ones. Although the carbon data is not shown, it bears out these trends.

The first two trends may follow from a breakdown in the assumption that pions are produced singly. It is quite possible that low-momentum pions are produced multiply, especially in higher-energy collisions:

$$N+N \rightarrow NN\pi\pi \text{ or } NN\pi\pi\pi. \tag{42}$$

It is well known[45] that the $N+N \rightarrow NN+m\pi$ cross section rises rapidly to a peak after the threshold for m-pion production is reached, and then slowly falls as the energy increases further. The energy threshold for single-pion production from two nucleons is 0.29 GeV; for two pions it is 0.60 GeV, and for three it is 0.93 GeV. Thus we are well into the peak of two-pion production, and somewhat into the region of three-pion production, at the 2.1 GeV/A beam energy.

The third and fourth trends are also probably related: with lighter targets, and with heavier projectiles, collective effects in the projectile that the mock-up ignores are more likely to be important. Also, just from geometric considerations, pion absorption in the projectile is more likely to occur in a large

projectile-small target situation. Effects due to charge exchange, and pion rescattering in the projectile, which are ignored by the mock-up, may be larger in this situation as well.

Next we examine an isobar model for pion production, to see how well it accounts for the data. In the spirit of Sternheim and Silbar[9,46], but without accounting for all the effects that they do, we assign weights for the processes listed in Eq. (39) by assuming single production of pions through Δ production and decay:

$$N+N \rightarrow N\Delta \rightarrow NN\pi. \tag{43}$$

Using Clebsch-Gordon coefficients, we get:

$$\begin{aligned}
p+p &\rightarrow \begin{cases} pp\,\pi^0 & \left(\frac{1}{8}\right) \\ pn\,\pi^+ & \left(\frac{5}{8}\right) \end{cases} \\
\left.\begin{matrix} p+n \\ n+p \end{matrix}\right\} &\rightarrow \begin{cases} pp\,\pi^- & \left(\frac{1}{12}\right) \\ pn\,\pi^0 & \left(\frac{1}{3}\right) \\ nn\,\pi^+ & \left(\frac{1}{12}\right) \end{cases} \\
n+n &\rightarrow \begin{cases} nn\,\pi^0 & \left(\frac{1}{8}\right) \\ np\,\pi^- & \left(\frac{5}{8}\right). \end{cases}
\end{aligned} \tag{44}$$

Next we need to fold in the probabilities for an N-N interaction. We assume a geometric cross section πR^2 for a nuclear interaction, where R is the nuclear radius. Then the probability for an interaction between a nucleon in the pro-

jectile with a neutron in the target is proportional to

$$\frac{N_A}{A_A}\pi R_A^2 = N_A \pi r_o^2 (A_A)^{-1/3} \tag{45}$$

and with a proton is

$$\frac{Z_A}{A_A}\pi R_A^2 = Z_A \pi r_o^2 (A_A)^{-1/3} \tag{46}$$

where r_o is the nucleon radius.

Combining these factors with the corresponding terms for the interaction of a target nucleon with the projectile, we obtain

$$\begin{aligned} &pp: && Z_A Z_B (A_A^{-1/3}+A_B^{-1/3})\pi r_o^2 \\ &pp = np: && (Z_A N_B + N_A Z_B)(A_A^{-1/3}+A_B^{-1/3})\pi r_o^2 \\ &nn: && N_A N_B (A_A^{-1/3}+A_B^{-1/3})\pi r_o^2. \end{aligned} \tag{47}$$

Thus, combining the two sets of equations, and neglecting the common factor of πr_o^2, we obtain that the pion yields should be proportional to the following formulae:

$$\begin{aligned} &\pi^+: && [\tfrac{5}{6}(Z_A Z_B) + \tfrac{1}{12}(Z_A N_B + N_A Z_B)](A_A^{-1/3}+A_B^{-1/3}) \\ &\pi^0: && [\tfrac{1}{6}(Z_A Z_B + N_A N_B) + \tfrac{1}{3}(Z_A N_B + N_A Z_B)](A_A^{-1/3}+A_B^{-1/3}) \\ &\pi^-: && [\tfrac{5}{6}(N_A N_B) + \tfrac{1}{12}(Z_A N_B + N_A Z_B)](A_A^{-1/3}+A_B^{-1/3}). \end{aligned} \tag{48}$$

Table XXIX contains the values generated by these formulae for the beams and targets used.

If this model were to hold, we would expect the data, when plotted against these isobar yield factors, to fall on a line with a slope (on log-log paper) of one. In other words, we would expect $\sigma = C(\varepsilon,\mathrm{p})Y_\pi(A,B)$, where C just depends on beam and pion energy, and Y_π are the yield factors calculated above. Figure 22

is the integrated cross section plotted against these yield factors for the 1.05 GeV/A data. The 2.1 GeV/A data is similar. The straight lines are not fits to the data, but rather lines of slope equal to one. We see that, although the model appears to account for the variation with target when beam and pion charge are held constant, it does not completely account for the variation between beams and between positive and negative pions. In the 1.05 GeV/A case, the proton data straddles the line formed by the heavier beams. In the 2.1 GeV/A case, the π^+ proton data coincides with the heavier beam data, while the π^- proton data is larger by more than a factor of three.

When broken down by pion momentum (Fig. 23), the same trends are evident, although the 500 MeV/c data shows deviations from the slope-one line that do not show at 200 MeV/c. This would indicate that other processes besides $NN \rightarrow N\Delta \rightarrow NN\pi$ are important in higher-momentum pion production. This is consistent with the fact that, for example, at 2.1 GeV the kinematic limit for a backwards pion produced directly (that is, via $pp \rightarrow \pi d$) is 269 MeV/c, whereas it is only 157 MeV/c for a pion produced via Δ production and decay. This does not necessarily mean that direct production *is* the mechanism responsible for high-energy pions, just that the formation of Δ's is insufficient to explain it.

B. Comparison With Other Data

We have already discussed how our proton data compares with that of Baldin, *et al.*[4(a)] We see the same exponential trend, and the slopes of our proton-induced data fit nicely with those of Baldin.

Perdrisat, *et al.*[5], looked at π^+ production at 155° and 180° from low-energy (175 MeV/A) deuterons and alphas, as well as at 155° from 600 MeV protons. Relevant to the current work is their data from the reaction 175 MeV/A $\alpha + C \rightarrow \pi^+(180°)$, with a slope of 17.4 MeV, and from the reaction 600 MeV

$p + C \rightarrow \pi^+(155°)$, with a limiting slope of 25 MeV. ("Limiting" because there is a turnover in the data below 50 MeV; including these points in the fit gives a "slope" of 30 MeV.) These slopes are consistent with the trends we have already seen.

Data from Anderson, *et al.*[47], for 1.05 and 2.1 GeV/A $C + C \rightarrow \pi^-(0°)$ can be transformed into the projectile frame and compared with our corresponding data at 180°. This has been done in Fig. 24. The two data sets are seen to be in good agreement, both in overall magnitude and shape. This is to be expected, as the target and projectile frames must be equivalent when the projectile and target are identical. The excellence of the agreement between the two data sets, from two different experiments, shows that our normalizations are correct.

C. Comparison With Models

The comparison with models is done in the same order as the models were presented in Chapter II. First we discuss the hard scattering models, then the statistical ones.

C.1. Schmidt and Blankenbecler

The model of Schmidt and Blankenbecler previously discussed predicted scaling of invariant cross section versus x'; that is, plots of invariant cross section versus x' for different beam energies should all fall on one line. We have previously observed[15] (see Fig. 25) that such scaling does not hold in the backward direction, indicating that their assumption of coherent recoil is most likely incorrect.

C.2. Landau and Gyulassy

The comparison of our data with the Landau and Gyulassy cluster-scattering model is shown in Fig. 26. Their proton curves have been previously

normalized to the data of Baldin, *et al.*[4(a)]; the normalization of the alpha curves is arbitrary. We only show their calculations using a single nucleon as the "cluster"; the calculations using a deuteron or alpha cluster do not fit as well as this case. Their Fermi momentum distributions are of the form $\exp[-p^2/2\sigma^2]$ with σ=130 MeV/c in the Gaussian case, and $\exp[-|p|/k_0]$ with k_0=100 MeV/c in the exponential case. As can be seen, the best fit occurs when scattering off a single nucleon with an exponential Fermi momentum distribution is assumed.

The success of this model, compared with the failure of the SB model on which it is based, indicates that while the pions we observed were most likely produced in single nucleon-nucleon collisions, the spectator portion of the nucleus does not share the recoil momentum equally among its constituents. It also indicates that the internal Fermi momentum distribution is more closely characterized by an exponential than by a Gaussian. This latter aspect is puzzling, as one would normally associate a Gaussian distribution with simple single-particle effects. One explanation is that the exponential distribution may be hiding the effects of higher-order correlations that don't show up in the "cluster" version of the LG model. Or it could indicate the importance of the higher-momentum components, or be simulating the effects of final state interactions.

It should be noted that the LG calculations were done only for the lighter beams (protons and alphas). It would be interesting to see if this model is as successful for the heavier beams.

C.3. Wong and Blankenbecler

Turning next to the model of Wong and Blankenbecler, we see in Fig. 27(a) and 27(b) graphs of invariant cross section versus their x_R for the p+Cu→π^-

and Cu+C→π^- data. At first glance, it appears that the data do indeed scale as predicted. However, on closer examination, it can be seen that the points for each beam energy fall on their own lines, with the slope of each line becoming shallower with increasing beam energy. This indicates that the model fails to account fully for the variation with energy of the cross sections, and has lead Wong and his colleagues to abandon the approximation approach and do a complete numerical integration of the six-fold integral discussed in Chapter II[48].

It should be noted that this model is closer in spirit to the LG model than the original SB model, in that it makes fewer simplifying assumptions concerning the distribution of the "recoil" momentum over the residual target nucleons.

C.4. Quasi-Two-Body Scaling

The last hard scattering model we look at is quasi-two-body scaling. Figure 28 shows our data plotted according to Frankel's prescription. We see that the data does not all conform to the same slope, indicating that this is not a good model. It should also be noted that the k_{min} values of the low-energy pions are negative. These values have no physical meaning in the context of the QTBS model. Although QTBS is different from the SB model, its failure implies a related cause: the assumption that the recoil momentum is distributed over many nucleons in the residual target is wrong. The failure of these models and the relative success of the LG model suggests that the recoil momentum is concentrated in just a few, or even only one, of the "residual target" nucleons, implying that the target itself fragments in the course of the collision.

C.5. Firestreak and Rows-on-Rows

Figure 29 is a comparison of our data with the predictions of the firestreak model and the rows-on-rows model of Bohrmann and Knoll. The firestreak model, which is known to over-predict pion production in other cases, continues to do so in the backward direction. In addition, this model falls off much more slowly than the actual data. Thus we see that the firestreak model is not a good model for pion production in the backward direction.

The rows-on-rows model is closer in magnitude to the actual data than the firestreak model, but is still slightly on the high side. In addition, whereas the data tends to follow a straight exponential, the rows-on-rows model predicts a curve in the cross section, and thus a different shape. This curvature is more noticeable for the lighter beams than for the heavier one. Thus, while the rows-on-rows model works fairly well for the heavier beam data, it does not do as well as the LG model for the lighter beam data. Of course, one would expect a statistical model to work better with large numbers of nucleons (heavy beams) than with small numbers (light beams). It should also be noted that the rows-on-rows model makes no distinction between π^- and π^+ production.

Overall, we can thus say that the statistical models do not do as well as the Landau and Gyulassy hard scattering model in explaining the data. Again, this suggests that it is the individual nucleons, rather than the bulk matter of the nucleus, that is responsible for the backward pion production.

C.6. Meng Ta-Chung

Figure 30 shows our proton and argon data plotted according to the scheme of Meng Ta-Chung. We see that the scaling predicted by Meng Ta-Chung holds for the π^- data. It also holds for the π^+ data, except in the case of the proton beam (Fig. 30(c)). Here we see a definite energy dependence, although

the target independence predicted by Meng still holds.

The original model of Meng neglected the π^-/π^+ difference. As discussed in Chapter II, our results concerning the proton-induced pions led Meng to investigate these differences and come up with the prediction that at low beam energies the π^-/π^+ ratio should be between 0.09 and 0.19, and increase towards unity with increasing beam energy. While our trend agrees with his prediction, the actual numbers differ. For a beam of 0.8 GeV protons, we observe a π^-/π^+ ratio of 0.30, 0.25, and 0.29 for targets of C, Cu, and PB, respectively—not as low as Meng predicts. Of course, effects such as charge exchange, which are ignored by Meng, could account for our higher π^-/π^+ ratios.

Turning to T_0, we compare Meng's prediction for its energy dependence with our proton-induced data in Fig. 31. As can be seen, Meng's model accounts very well for the energy dependence of T_0, but predicts a much wider variation of T_0 with target mass than is in fact present.

To extract meaning from Meng's generally successful scaling of the data, we must turn back to his assumptions, namely that the pions are produced in gentle, peripheral collisions, with the energy available in the collision proportional to the number of nucleons involved. It is difficult to reconcile these assumptions with those of the equally successful LG model, which imply that pions are produced in single nucleon-nucleon hard scattering collisions. This apparent contradiction will be expanded upon in the next chapter.

D. Kaon Search

Kaon production, like pion production, can be used to study the nature of nucleus-nucleus collisions. Kaon production brings another degree of freedom into the picture, that of strangeness. If kaons are more readily produced in A-A collisions than they are in N-N collisions, they could give us another

handle on the dynamics involved.

For example, consider the simplest reaction for producing kaons in a p-p collision:

$$p + p \rightarrow K^{+} \Lambda p. \tag{49}$$

For a 4.89 GeV incident proton, the highest backward momentum a kaon could have is 151 MeV/c. For an incident proton of infinite energy, the corresponding kaon momentum would be 339 MeV/c. Another way of looking at this is to say that a 4.89 GeV incident proton would have to strike a nucleon with a backward-going Fermi momentum of 400 MeV/c to produce a backward-going kaon of 465 MeV/c. As these kinematic limits are much lower than the corresponding ones for pion production, kaon production has the possibility of revealing more information on collective effects and/or the high end of the Fermi momentum distribution.

We looked for K^{+} production in the following cases, all above the p-π threshold described above:

Beam and Energy (GeV)	Target	Momentum (MeV/c)
4.89 p	Cu	250
		300
2.1 α	C	200
		400
	Cu	200
		400
2.1 C	Cu	300

Figure 32 is a plot of the subtracted data (counts) for a typical run to observe K^{+} production. Superimposed are the counts for the corresponding "long gate" (proton and positive pion) run. What appears to be a peak near where kaons are expected turns out to be the tail of the proton peak getting into the gate. This is true for all the cases listed above. Since we did not detect

a measurable K^+ signal above background, the best we can do is assign an upper bound to the cross section, based upon the length of the run. Table XXX lists the upper bound cross sections at the ninety percent confidence level for these kaon runs. These upper bounds are consistent with the kaon cross section measurements of Schnetzer, *et al.*[49]

Our failure to see kaons is not due to any lack of sensitivity of the spectrometer. For example, we would have seen about 10^3 pions in each counter in the equivalent "short gate" runs. Another way of stating this is that we saw no kaons in 10^3 pions, which is consistent with the difference between the total pion and kaon cross sections at these energies.

This lack of kaons is consistent with a simple nucleon-nucleon collision picture, without any exotic features such as high Fermi momentum components or collective effects. However, the lack of evidence for these features does not mean that they are definitely not there.

CHAPTER VI

SUMMARY AND CONCLUSIONS

This experiment has clearly met its objectives. It has systematically explored the variation of backward pion production with energy, beam, and target. It has also been successful in providing a testing ground for a variety of theories, and has stimulated thought in theoretical circles. It also points the way for future experiments.

A. Systematics

There are three points to be made concerning the systematics of the data itself. These concern the energy dependence of T_0, the AB dependence of $d\sigma/d\Omega$, and the implications of the mock-up fit.

A.1. T_0 Energy Dependence

One possible interpretation of the exponential slope parameter T_0 is as a temperature. With this interpretation, the saturation of T_0 with increasing proton beam energy may indicate a phase transition. As an analogy, consider the momentum distribution of water molecules above the surface of a pan of water sitting on a stove. As one increases the heat flow into the water, the temperature as determined by the momentum distribution is seen to increase, until the water starts to boil. At that point, the addition of more heat (corresponding to higher energies) causes the water to boil more rapidly, increasing the rate at which water molecules are produced (corresponding to the increase in cross section), but leaving the relative momentum distribution unchanged.

However, the model of Meng Ta-Chung interprets the "saturation" of T_0 as a kinematical effect, due to the Lorentz transformation between the laboratory and projectile frames, and thus has nothing to do with a phase transition. Unfortunately, we do not have enough evidence as yet to determine which of these interpretations, if either, is correct.

Saturation of T_0 was not seen with the heavier beams with the beam energies used in this experiment. It should be noted that the saturation with proton beams did not set in until energies were used that were greater than the ones used with heavy beams. Measurements with higher-energy heavy beams would be useful to see if and when this saturation occurs. Saturation of T_0 with heavy beams at the same energy and value as with proton beams would be further evidence for the domination of pion production by single nucleon-nucleon collisions, for it would mean that a B-A collision was the same as "B" p-A collisions.

A.2. AB Dependence of $d\sigma/d\Omega$

The AB dependence of $d\sigma/d\Omega$ is striking. The change in power from 0.80 at 1.05 GeV/A to 0.95 at 2.1 GeV/A could indicate a transition from a surface-surface interaction to a volume-volume one. Again, measurements with higher-energy heavy beams, as well as (or especially with) lower-energy ones, would be helpful in exploring this point.

A.3. Mock-up Implications

The mock-up showed that much of the cross section of B-A collisions could be accounted for by "B" p-A collisions. This means that no strong collective effects in the projectile are needed to explain backward pion production, at least for the lower-energy pions. In association with the results of the model comparisons, this may indicate that no collective effects occur *anywhere* in the

production of backward pions.

B. Model Comparisons

The underlying theme coming out of the model comparisons is that single N-N collisions produce the backward pions, *without* any "coherent recoil" of the spectator nucleons. Those hard scattering models that assume coherent recoil—SB and QTBS—perform poorly. Those models that do not—LG and, to a lesser extent, Wong and Blankenbecler—do much better. The statistical models, which in effect deal *only* with collective behavior, do worst of all, although it must be said that the rows-on-rows model is adequate for the heaviest beams.

We are still left with the model of Meng Ta-Chung. It successfully applies scaling to the target dependence of the cross sections, while failing in the specific prediction for the target dependence of T_0. The energy dependence of T_0 *is* explained successfully, however, and the predicted energy scaling holds in all but the $p \to \pi^+$ case. Given this mixed bag of results, we must somehow reconcile the assumptions of this model with the conflicting assumptions of the more successful model of LG.

The energy dependence of Meng's model comes from treating the kinetic energy *per nucleon* as the important independent variable, not the total kinetic energy "per beam". This is what one would expect if just a single nucleon in the beam nucleus was responsible for the pion production.

The source of the target dependence of Meng's model is less obvious. In the T_0 prediction, it appears to be related to Meng's ν_{BT}, the number of target nucleons that interact with the effective projectile. This number is larger than two in all the cases studied, and directly conflicts with the implication of the success of the LG model that it is a single nucleon in the target that is involved in the collision. The scaling of the cross sections is more complicated, as

target-dependent factors show up in both ν_{BT}, which scales the pion energy, and in the area available for the interaction region (Meng's a_2), which scales the pion cross section. While it is not transparent, perhaps these interact in a way which imitates the mechanism that actually determines the target dependence of the cross section. Further study of the target dependence is definitely needed. More study into the relationship of Meng's model with hard scattering models and the more traditional of the statistical models would also be helpful.

We earlier noted that the LG model was only applied to the data for the proton and alpha beams, and that it is with the heavier beams that the Meng model, along with the rows-on-rows model, works best. It could be that different mechanisms are at work in these two differing regions of parameter space, and that each model is in fact describing the mechanism dominant in its own region. An important test of these two models would be to look for two-particle (and higher) correlations, with a backward-going pion as one of the particles. Meng's model implies that the residual projectile, with perhaps some of its own emitted pions, would be detected in the forward direction, with no target fragments in any direction. The LG model, on the other hand, suggests that target (and projectile) fragments would be detected in many directions, as the "recoil" momentum would be concentrated in only a few nucleons and would thus cause both target and projectile breakup.

C. Future Work

The results of this experiment indicate two directions for further work. One avenue would be to continue the measurements of single-pion inclusive cross sections at lower and higher energies, and with heavier beams. This would allow for the study of the saturation of T_0 and of the AB dependence. The other avenue would be to look for correlations with backward pions in the forward

and perpendicular directions. This could provide a finer test for distinguishing between models since, as explained in the previous section, different models that work equally well in single-pion production can differ in their predictions of expected two-particle correlations. It is hoped that these future experiments will help us achieve a deeper understanding of high-energy nucleus-nucleus collisions.

APPENDIX A

OTHER TARGETS

In addition to the five standard targets (C, Al, Cu, Sn, and Pb), some data was also taken using the 0.80 GeV and 4.89 GeV proton beam on polyethylene (CH_2), deuterated polyethylene (CD_2), and silver (Ag) targets (see Table I). While none of this data was used in the preparation of this dissertation, the results are presented here for completeness. Tables XXXI-XXXIII contain the measured pion production cross sections for these targets. Cross sections from the CH_2 and CD_2 targets were calculated as if the scattering centers were single objects of CH_2 and CD_2, respectively.

The original intent of the CH_2 and CD_2 measurements was to calculate pion production cross sections from p and d, respectively, by subtracting the corresponding cross section measurement of C:

$$\begin{aligned} \sigma_p &= (\sigma_{CH_2} - \sigma_C)/2 \\ \sigma_d &= (\sigma_{CD_2} - \sigma_C)/2 \end{aligned} \tag{50}$$

with the corresponding errors combined in quadrature.

The results of this subtraction are presented in Tables XXXIV and XXXV. The subtracted cross sections from the 0.80 GeV proton beam, and most of the CH_2 subtracted cross sections are consistent with zero. The subtracted cross sections for the 4.89 GeV $p+CD_2$ data, where not consistent with zero, have large error bars, ranging from 26 percent to 77 percent.

The Ag target was included so that a direct comparison could be made of the cross sections for backward production of protons, deuterons, and tritons

in this experiment[50] with a similar experiment by Frankel, *et al.*[51]

REFERENCES

[1] (a) V.V. Burov, V.K. Lukyanov, and A.I. Titov, Phys. Lett. **67B**, 46 (1977);

(b) M.I. Gorenstein and G.M. Zinovjev, Phys. Lett. **67B**, 100 (1977);

(c) M.B. Mathis and Meng Ta-chung, Phys. Rev. C **18**, 952 (1978);

(d) L.L. Frankfurt and M.I. Strickman, Phys. Lett. **83B**, 407 (1979).

[2] I.A. Schmidt and R. Blankenbecler, Phys. Rev. D **15**, 3321 (1975).

[3] James Papp, Lawrence Berkeley Laboratory Report No. LBL-3633, May 1975 (Ph.D. thesis, unpublished); J. Papp, J. Jaros, L. Schroeder, J. Staples, H. Steiner, A. Wagner, and J. Wiss, Phys. Rev. Lett. **34**, 601 (1975).

[4] (a) A.M. Baldin, N. Giordenescu, V.N. Zubarev, L.K. Ivanova, N.S. Moroz, A.A. Povtoreiko, V.B. Radomanov, and V.S. Stavanskii, Yad. Fiz. **20**, 1201 (1974) [Sov. J. Nucl. Phys. **20**, 629 (1975)];

(b) A.M. Baldin, N. Giordenescu, V.N. Zubarev, L.K. Ivanova, N.S. Moroz, A.A. Povtoreiko, V.B. Radomanov, V.S. Stavanskii, V.K. Bondarev, and Yu.N. Yakovlev, Yad. Fiz. **21**, 1008 (1975) [Sov. J. Nucl. Phys. **21**, 517 (1978)];

(c) A.M. Baldin, AIP Conference Proceedings No. 26, pg. 621-41 (invited talk at High Energy Physics and Nuclear Structure Conference held at Santa Fe and Los Alamos, New Mexico, 9-13 June 1975).

[5] C.F. Perdrisat, S. Frankel, and W. Frati, Phys. Rev. C **18**, 1764 (1978).

[6] D.R.F. Cochran, P.N. Dean, P.A.M. Gram, E.A. Knapp, E.R. Martin, D.E. Nagle, R.B. Perkins, W.J. Shlaer, H.A. Thiessen, and E.D. Theriot, Phys. Rev. D **6**, 3085 (1972).

[7] (a) D. Drechsel and H.J. Weber, Nucl Phys. **B25**, 159 (1970);

(b) E. Ferrari and F. Selleri, Nuovo Cimento **21**, 1028 (1961);

(c) V.C. Suslenko and V.I. Kochkin, JINR report, Dubna 1970 (unpublished).

[8] (a) H.W. Bertini and M.P. Guthrie, Nucl. Phys. **A169**, 670 (1971);

(b) N. Metropolis, R. Bivins, M. Storm, Anthony Turkevich, J.M. Miller, and G. Friedlander, Phys. Rev. **110**, 185 and 204 (1958).

[9] M. Sternheim and R. Silbar, Phys. Rev. D **6**, 3317 (1972).

[10] I would like to thank Miklos Gyulassy for clarifying this point for me.

[11] Miklos Gyulassy, Lawrence Berkeley Laboratory Report LBL-11040, July 1980 (unpublished).

[12] R.H. Landau and M. Gyulassy, Phys. Rev. C **19**, 149 (1979). This reference provides a very good summary of hard scattering models, and explains the model of Schmidt and Blankenbecler[2] even better than the original authors.

[13] I would like to thank Rubin Landau for clarifying this point for me.

[14] R.D. Amado and R.M. Woloshyn, Phys. Lett. **69B**, 400 (1977).

[15] (a) S. Chessin, J. Geaga, J. Grossiord, D. Hendrie, L. Schroeder, B. Treuhaft, K. Van Bibber, and C. Wuest, Bull. Am. Phys. Soc. **23**, 48 (1978).

(b) L.S. Schroeder, S.A. Chessin, J.V. Geaga, J.Y. Grossiord, J.W. Harris, D.L. Hendrie, R. Treuhaft, and K. Van Bibber, Phys. Rev. Lett. **43**, 1787 (1979).

[16] Rubin H. Landau, Phys. Rev. C **17**, 2144 (1978).

[17] C.Y. Wong and R. Blankenbecler, SLAC-PUB-2488, Mar. 1980 (Submitted to Phys. Rev. Lett.)

[18] Cheuk-Yin Wong and R. Blankenbecler, Phys. Rev. C **22**, 2433 (1980).

[19] (a) R.D. Amado and R.M. Woloshyn, Phys. Rev. Lett. **36**, 1435 (1976);

(b) Sherman Frankel, Phys. Rev. Lett. **38**, 1338 (1977);

(c) R.D. Amado and R.M. Woloshyn, Phys. Rev. C **16**, 1255 (1977);

(d) Sherman Frankel, Phys. Rev. C **17**, 694 (1978);

(e) Sherman Frankel, University of Pennsylvania Report No. UPR 0087T, 1978 (unpublished).

[20] See footnote 5 of Ref. 19(b).

[21] (a) William D. Myers, Nucl. Phys. **A296**, 177 (1978);

(b) J. Gosset, J.I. Kapusta, and G.D. Westfall, Phys. Rev. C **18**, 844 (1978).

[22] (a) G.D. Westfall, J. Gosset, P.J. Johansen, A.M. Poskanzer, W.G. Meyer, H.H. Gutbrod, A. Sandoval, and R. Stock, Phys. Rev. Lett. **37**, 1202 (1976);

(b) J. Gosset, H.H. Gutbrod, W.G. Meyer, A.M. Poskanzer, A. Sandoval, R. Stock, and G.D. Westfall, Phys. Rev. C **16**, 629 (1977).

[23] S. Nagamiya, I. Tanihata, S. Schnetzer, L. Anderson, W. Brückner, O. Chamberlain, G. Shapiro, and H. Steiner, in *Proceedings of the International Conference on Nuclear Structure, Tokyo, 1977*, edited by T. Marumori (Physical Society of Japan, Tokyo, 1978) [J. Phys. Soc. Jpn. **44**, Suppl. 378 (1978)].

[24] K. Nakai, J. Chiba, I. Tanihata, S. Nagamiya, H. Bowman, J. Ioannou, and J.O. Rasmussen, contribution to the VIIth International Conference on High-Energy Physics and Nuclear Structure, Zürich, August, 1977 (unpublished); J. Chiba, K. Nakai, I. Tanihata, S. Nagamiya, H. Bowman, J. Ingersoll, and J.O. Rasmussen, Phys. Rev. C **20**, 1332 (1979). Note that the citation to this work in Ref. 21(b) (their Ref. 4) is incorrect.

[25] (a) Jörn Knoll, Phys. Rev. C **20**, 773 (1979);

(b) Jörn Knoll, Nucl. Phys. **A343**, 511 (1980).

[26] Steffen Bohrmann and Jörn Knoll, Nucl. Phys. **A356**, 498 (1981).

[27] Enrico Fermi, Prog. of Theor. Phys. **5**, 570 (1950); E. Fermi, Phys. Rev. **92**, 452 (1953).

[28] A. Sandoval, R. Stock, H.E. Stelzer, R.E. Renfordt, J.W. Harris, J.P. Brannigan, J.V. Geaga, L.J. Rosenberg, L.S. Schroeder, and K.L. Wolf, Phys. Rev. Lett. **45**, 874 (1980).

[29] M.-C. Lemaire, S. Nagamiya, O. Chamberlain, G. Shapiro, S. Schnetzer, H. Steiner, and I. Tanihata, Lawrence Berkeley Laboratory Report LBL-8463, November 1978 (unpublished).

[30] (a) H.B. Mathis and Meng Ta-chung, Phys. Rev. C **18**, 952 (1978);
(b) Meng Ta-chung, Phys. Rev. Lett. **42**, 1331 (1979);
(c) U. Brosa, Meng Ta-chung, and E. Moeller, FUB-HEP-17-11/80.

[31] Meng Ta-chung, Phys. Rev. D **15**, 197 (1977); Meng Ta-chung and E. Moeller, FUB-HEP-76/11; Meng Ta-chung, in *Proceedings of the Topical Meeting on Multiparticle Production on Nuclei at Very High Energies, Trieste, 1976*, edited by G. Pellini, L. Bertocchi, and P.G. Rancoita (International Centre for Theoretical Physics, Trieste, Italy, 1977), pp. 435-462.

[32] Meng Ta-chung, Phys. Rev. D **9**, 3062 (1974); Meng Ta-chung and E. Moeller, Phys. Rev. D **14**, 1449 (1976).

[33] Kwan-Wu Lai and Meng Ta-chung, Phys. Rev. Lett. **37**, 241 (1976).

[34] PDP is a registered trademark of the Digital Equipment Corporation.

[35] EPB stands for External Proton Beam, a historical reference to the days when the Bevatron accelerated only protons.

[36] J. Cuperus and R. Morgado, IEEE Trans. Nucl. Sci. **NS-22**, 1561(1975).

[37] Scotch Magic Transparent Tape, 3/4 . Scotch is a registered trade mark of the 3M Company.

[38] Alan R. Smith (LBL), personal communication.

[39] Don Nelson, Lawrence Berkeley Laboratory Engineering Note MT-259, 2 March 1977 (unpublished).

[40] Charles G. Dols, Lawrence Berkeley Laboratory Report LBL-1311, Sept. 1972 (unpublished).

[41] (a) Q3 calibration: Don Nelson, personal communication.
(b) Q4 calibration: Donald H. Nelson, Lawrence Berkeley Laboratory Engineering Note MT-283, 27 July 1977 (unpublished).

[42] T.J. Devlin, OPTIK: An IBM 709 computer program for the optics of high energy particle beams, Lawrence Berkeley Laboratory Report UCRL-9727, 15 Sept 1961 (unpublished); J.S. Colonias, *Particle Accelerator Design: Computer Programs* (Academic Press, New York, 1974), pp. 164-182.

[43] Uriel Vogel, Rev. Sci. Instrum. **36**, 188 (1965).

[44] V.S. Shirley and C.M. Lederer, editors, *Nuclear Wallet Cards* (Isotopes Project, Lawrence Berkeley Laboratory, Berkeley, California, 1979).

[45] Particle Data Group (Odette Benary, LeRoy R. Price, and Gideon Alexander), "NN and ND interactions (above 0.5 GeV/c) — a compilation", Lawrence Berkeley Laboratory, UCRL-20000 NN (August 1970).

[46] John Peter Sullivan, Ph.D. thesis, Lawrence Berkeley Laboratory Report No. LBL-12546, 1981.

[47] L.M. Anderson, Jr., O. Chamberlain, S. Nagamiya, S. Nissen-Meyer, D. Nygren, L. Schroeder, G. Shapiro, and H. Steiner, Lawrence Berkeley Laboratory Report No. LBL-9493, July 1979 (unpublished).

[48] C.Y. Wong, personal communication.

[49] S. Schnetzer, M.-C. Lemaire, R. Lombard, E. Moeller, S. Nagamiya, G. Shapiro, H. Steiner, and I. Tanihata, Lawrence Berkeley Laboratory Report No. LBL-14523, 1982;
Stephen R. Schnetzer, Ph.D. thesis, Lawrence Berkeley Laboratory Report No. LBL-13727, 1981.

[50] J.V. Geaga, S.A. Chessin, J.Y. Grossiord, J.W. Harris, D.L. Hendrie, L.S. Schroeder, R.N. Treuhaft, and K. Van Bibber, Phys. Rev. Lett. **45**, 1993 (1980).

[51] S. Frankel, W. Frati, Q. Van Dyck, R. Werbeck, and V. Highland, Phys. Rev. Lett. **36**, 642 (1976).

LIST OF TABLES

TABLE I. Beam, energy, and target combinations used in this experiment.

TABLE II. Dimensions of the front and rear scintillator telescopes. Length is in the direction of momentum dispersion, thickness is parallel to the dispersed beam, and height is perpendicular to both length and thickness.

TABLE III. π^+ production cross sections from 0.80 GeV protons.

TABLE IV. π^+ production cross sections from 1.05 GeV protons.

TABLE V. π^+ production cross sections from 2.1 GeV protons.

TABLE VI. π^+ production cross sections from 3.5 GeV protons.

TABLE VII. π^+ production cross sections from 4.89 GeV protons.

TABLE VIII. π^- production cross sections from 0.80 GeV protons.

TABLE IX. π^- production cross sections from 1.05 GeV protons.

TABLE X. π^- production cross sections from 2.1 GeV protons.

TABLE XI. π^- production cross sections from 4.89 GeV protons.

TABLE XII. π^+ production cross sections from 1.05 GeV/A alphas.

TABLE XIII. π^+ production cross sections from 2.1 GeV/A alphas.

TABLE XIV. π^- production cross sections from 1.05 GeV/A alphas.

TABLE XV. π^- production cross sections from 2.1 GeV/A alphas.

TABLE XVI. π^+ production cross sections from 0.40 GeV/A carbon.

TABLE XVII. π^+ production cross sections from 1.05 GeV/A carbon.

TABLE XVIII. π^+ production cross sections from 2.1 GeV/A carbon.

TABLE XIX. π^- production cross sections from 0.40 GeV/A carbon.

TABLE XX. π^- production cross sections from 1.05 GeV/A carbon.

TABLE XXI. π^- production cross sections from 2.1 GeV/A carbon.

TABLE XXII. π^+ production cross sections from 1.05 GeV/A argon.

TABLE XXIII. π^+ production cross sections from 1.83 GeV/A argon.

TABLE XXIV. π^- production cross sections from 1.05 GeV/A argon.

TABLE XXV. π^- production cross sections from 1.83 GeV/A argon.

TABLE XXVI. π^+ production cross sections from 0.40 GeV/A neon.

TABLE XXVII. Tabulation of the slopes and integrated cross sections for all the experimental conditions.

TABLE XXVIII. π^-/π^+ ratios.

TABLE XXIX. Isobar model yield factors.

TABLE XXX. Upper bounds at the ninety percent confidence level of the K^+ cross section.

TABLE XXXI. π^+ production cross sections from 0.80 GeV protons, for Ag target.

TABLE XXXII. π^- production cross sections from 0.80 GeV protons, for CD_2 and Ag targets.

TABLE XXXIII. π^- production cross sections from 4.89 GeV protons, for CH_2 and CD_2 targets.

TABLE XXXIV. Subtracted π^- production cross sections from 0.80 GeV protons for CD_2 target.

TABLE XXXV. Subtracted π^- production cross sections from 4.89 GeV protons for CH_2 and CD_2 targets.

TABLE I. Beam, energy, and target combinations used in this experiment.

Kinetic energy per nucleon (GeV)	Beam	Targets
0.4	C Ne	C,Cu,Ph Cu,Sn,Pb
0.8	p	C,Cu,Ag,Pb CD_2 (π^- only)
1.05	p α C Ar	C,Al,Cu,Sn,Pb
1.83	Ar	C,Al,Cu,Sn,Pb
2.1	p α C	C,Al,Cu,Sn,Pb
3.5	p	Cu (π^+ only)
4.89	p	C,Cu,Pb CH_2,CD_2 (π^- only)

TABLE II. Dimensions of the front and rear scintillator telescopes. Length is in the direction of momentum dispersion, thickness is parallel to the dispersed beam, and height is perpendicular to both length and thickness.

Detector	Length (inches)	Height (inches)	Thickness (inches)
F1	2.0	2.5	0.075
F2	2.0	2.5	0.075
R1A	1.47	0.99	0.25
R1B	1.47	0.99	0.25
R1C	1.47	0.98	0.25
R2	8.0	1.0	0.25

TABLE III. π^+ production cross sections from 0.80 GeV protons.

Mom (MeV/c)	C	Al	Cu	Sn	Pb
		$\frac{d^2\sigma}{d\Omega dp}\left[\frac{\text{mb}}{\text{sr-GeV/c}}\right]$ in form $(\sigma\pm\text{err})\times10^{\text{exp}}$			
185	3.40±.40 E0				2.69±.27 E1
186			1.28±.12 E1		
198	3.22±.39 E0				2.53±.27 E1
199			1.15±.11 E1		
215	3.29±.42 E0				2.43±.27 E1
218			1.08±.10 E1		
268	5.37±.98 −1		1.96±.32 E0		3.64±.62 E0
278	4.22±.80 −1		1.54±.18 E0		
282					3.52±.40 E0
286	4.00±.72 −1		2.03±.31 E0		
287					2.90±.50 E0
299			1.15±.15 E0		
300	3.05±.65 −1				
304					2.45±.32 E0
310	1.97±.61 −1		8.3 ±2.1 −1		
311					3.13±.57 E0
326	1.56±.50 −1		8.2 ±1.3 −1		
332					1.57±.26 E0
359	9.3 ±2.8 −2				
360					6.7 ±1.1 −1
367			2.36±.45 −1		
385	4.1 ±1.5 −2				
386					3.54±.69 −1
396			1.65±.36 −1		
420	2.0 ±1.6 −2				
421					2.13±.64 −1
433			9.6 ±3.2 −2		
434			6.2 ±3.4 −2		
440	9.0 ±7.1 −3				
441					1.20±.78 −1
474					9.7 ±7.2 −2

TABLE IV. π^+ production cross sections from 1.05 GeV protons.

Mom (MeV/c)	C	Al	Cu	Sn	Pb
		$\frac{d^2\sigma}{d\Omega dp}\left[\frac{mb}{sr-GeV/c}\right]$ in form $(\sigma\pm err)\times 10^{exp}$			
181		6.61±.75 E0			
182	3.54±.41 E0		1.20±.11 E1	1.66±.17 E1	2.57±.25 E1
192		4.88±.60 E0			
193	2.83±.36 E0		1.14±.11 E1		
194				1.31±.15 E1	2.45±.24 E1
207		6.02±.70 E0			
209	3.33±.40 E0		1.09±.11 E1	1.41±.16 E1	
210					2.12±.22 E1
266			2.08±.37 E0		
267	5.3 ±2.0 −1	1.20±.33 E0		3.92±.76 E0	6.5 ±1.1 E0
268					4.79±.57 E0
269	5.65±.95 −1	1.07±.15 E0	2.26±.25 E0		
270				3.43±.41 E0	
283			1.87±.31 E0		
284		7.3 ±2.3 −1		1.98±.49 E0	4.23±.77 E0
286					3.51±.45 E0
287	3.28±.72 −1	6.2 ±1.1 −1	1.53±.19 E0		
288				2.07±.20 E0	
305			1.03±.23 E0		
306				1.69±.45 E0	2.86±.64 E0
307	4.4 ±1.4 −1	9.8 ±2.4 −1			
309	1.51±.56 −1				2.31±.36 E0
310		4.9 ±1.0 −1	9.6 ±1.4 −1		
311				1.48±.26 E0	
352			3.5 ±1.3 −1		
353	2.49±.78 −1	2.07±.86 −1		5.2 ±2.2 −1	
354					1.01±.18 E0
354					1.17±.38 E0
355	8.3 ±3.4 −2	2.16±.81 −1	3.91±.66 −1	5.9 ±1.3 −1	
376			1.32±.83 −1		
377		1.52±.84 −1		3.3 ±1.9 −1	8.9 ±3.3 −1
378					5.2 ±1.1 −1
379	7.6 ±2.5 −2		2.13±.42 −1		
380		9.1 ±3.4 −2		3.87±.91 −1	
407				2.6 ±2.3 −1	
409					3.40±.89 −1
410			7.5 ±2.5 −2		
411	3.8 ±1.7 −2	8.9 ±2.8 −2		1.83±.63 −1	
443			1.59±.58 −1		
446					2.5 ±1.1 −1
475			4.7 ±4.5 −2		
478					1.6 ±1.2 −1
530			3.0 ±2.8 −2		

TABLE V. π^+ production cross sections from 2.10 GeV protons.

Mom (MeV/c)	C	Al	Cu	Sn	Pb
		$\frac{d^2\sigma}{d\Omega dp}\left[\frac{mb}{sr-GeV/c}\right]$ in form $(\sigma\pm err)\times10^{exp}$			
182		1.42±.15 E1			6.16±.62 E1
183			2.79±.27 E1	3.67±.38 E1	
184	6.60±.80 E0				
194	6.06±.76 E0	1.15±.13 E1	2.31±.23 E1	3.74±.39 E1	5.73±.58 E1
208		1.13±.14 E1			6.22±.65 E1
209			2.41±.25 E1	3.35±.38 E1	
211	6.31±.83 E0				
269			7.81±.84 E0		
275	1.60±.17 E0	2.67±.32 E0	7.57±.76 E0	1.06±.12 E1	1.34±.19 E1
288			4.48±.56 E0		
295	1.00±.13 E0	2.62±.31 E0	5.73±.62 E0	7.40±.93 E0	1.24±.16 E1
310			3.92±.54 E0		
318	9.6 ±1.3 −1	2.02±.28 E0	4.01±.52 E0	4.45±.74 E0	8.2 ±1.3 E0
362		9.1 ±1.1 −1			
363					5.02±.50 E0
364			1.89±.21 E0		
364			1.51±.27 E0	3.04±.33 E0	
364				3.42±.58 E0	
366	4.51±.69 −1	9.9 ±1.5 −1			4.24±.71 E0
367	4.53±.65 −1				
387		5.58±.79 −1			
388			1.37±.17 E0	2.29±.28 E0	3.48±.37 E0
391			1.34±.25 E0	2.25±.44 E0	
392					1.93±.47 E0
393	3.30±.49 −1				
393	3.09±.54 −1	5.5 ±1.1 −1			
418		3.52±.69 −1			
419			1.10±.16 E0	1.29±.19 E0	2.12±.28 E0
420	1.84±.40 −1				
423			1.07±.26 E0	1.57±.43 E0	
424					2.14±.57 E0
425	1.78±.52 −1	3.5 ±1.1 −1			
447		2.34±.40 −1			
451			8.4 ±2.1 −1		
453					1.75±.22 E0
454			5.76±.74 −1		
454			6.5 ±1.3 −1	9.9 ±1.4 −1	
456	8.9 ±1.9 −2			8.0 ±2.0 −1	1.26±.32 E0
457		2.13±.55 −1			
460	1.00±.25 −1				
478		1.02±.28 −1			
483			3.3 ±1.3 −1		8.7 ±1.4 −1
486			3.40±.54 −1	5.6 ±1.0 −1	
488			7.6 ±5.2 −2		

TABLE V (continued).

Mom (MeV/c)	C	Al	Cu	Sn	Pb
		$\frac{d^2\sigma}{d\Omega dp}\left[\frac{mb}{sr-GeV/c}\right]$ in form $(\sigma\pm err)\times10^{exp}$			
491	6.0 ±2.1 −2				
491	3.2 ±1.5 −2			4.5 ±1.8 −1	6.5 ±2.4 −1
492		8.9 ±4.1 −2			
503			1.58±.39 −1		
516		3.4 ±1.4 −2			
523					5.1 ±1.1 −1
526			2.04±.43 −1	1.74±.57 −1	
529	4.9 ±1.9 −2				
530			1.26±.71 −1		
532				2.3 ±1.4 −1	
535			8.9 ±5.0 −2		5.0 ±1.4 −1
536	1.7 ±1.4 −2				
537		6.7 ±2.7 −2	1.88±.40 −1		
537			1.16±.31 −1		
538				2.9 ±1.2 −1	
543			1.19±.34 −1		
572					2.65±.96 −1
576	1.43±.83 −2				
577		4.2 ±1.7 −2	4.5 ±1.9 −2		
577			6.1 ±2.1 −2		2.5 ±1.4 −1
578				1.29±.75 −1	
592			9.6 ±3.5 −2		
620					1.22±.71 −1
623			2.3 ±1.4 −2		
626		2.9 ±1.7 −2	4.1 ±2.1 −2		
627				4.5 ±2.9 −2	
688			1.45±.97 −2		
712			1.62±.59 −2		
713					2.6 ±1.2 −2
838					2.0 ±1.1 −2

TABLE VI. π^+ production cross sections from 3.50 GeV protons.

Mom (MeV/c)	C	Al	Cu	Sn	Pb
		$\frac{d^2\sigma}{d\Omega dp}\left[\frac{\text{mb}}{\text{sr-GeV/c}}\right]$ in form $(\sigma\pm\text{err})\times10^{\text{exp}}$			
180			3.65±.34 E1		
192			3.44±.32 E1		
206			4.19±.39 E1		
271			1.14±.12 E1		
290			9.9 ±1.0 E0		
312			7.37±.90 E0		
360			3.32±.45 E0		
386			2.45±.37 E0		
416			2.21±.39 E0		
446			1.62±.29 E0		
449			1.43±.25 E0		
478			1.00±.21 E0		
482			7.8 ±1.8 −1		
514			4.7 ±1.6 −1		
520			5.5 ±1.8 −1		
537			4.00±.88 −1		
577			2.07±.58 −1		
617			6.8 ±2.5 −2		
624			1.44+.84 −1		
662			2.3 ±1.3 −2		
667			3.8 ±1.7 −2		
702			4.2 ±1.5 −2		
716			3.0 ±1.7 −2		

TABLE VII. π^+ production cross sections from 4.89 GeV protons.

Mom (MeV/c)	C	Al	Cu	Sn	Pb
		$\frac{d^2\sigma}{d\Omega dp}\left[\frac{\text{mb}}{\text{sr-GeV/c}}\right]$ in form $(\sigma\pm\text{err})\times10^{\text{exp}}$			
184	7.42±.82 E0		3.45±.30 E[illegible]		
185					8.85±.78 E1
197	7.26±.84 E0		3.39±.30 E1		9.15±.81 E1
211	8.70±.98 E0		3.77±.34 E1		
212					9.52±.86 E1
277	2.39±.30 E0		1.06±.10 E1		3.11±.26 E1
280	1.90±.30 E0		1.05±.10 E1		2.87±.30 E1
295	2.16±.29 E0				2.34±.22 E1
298			9.32±.89 E0		
299	2.36±.33 E0		8.50±.86 E0		2.50±.28 E1
317	1.67±.28 E0		7.82±.81 E0		1.90±.19 E1
321			7.78±.83 E0		
322	1.69±.29 E0				2.07±.25 E1
369	7.6 ±1.3 −1		3.67±.37 E0		9.80±.98 E0
372			4.30±.59 E0		1.12±.15 E1
373	9.7 ±1.5 −1				
395	4.4 ±1.2 −1		2.80±.31 E0		8.54±.91 E0
398			3.13±.52 E0		7.1 ±1.2 E0
399	6.8 ±1.4 −1				
424					6.24±.75 E0
425	2.4 ±1.0 −1		2.38±.29 E0		
429	6.1 ±1.3 −1		2.63±.51 E0		7.7 ±1.4 E0
466	2.77±.30 −1		1.83±.25 E0		4.56±.71 E0
466					4.41±.65 E0
499	1.53±.47 −1		1.08±.19 E0		3.49±.60 E0
500					2.95±.58 E0
538	3.8 ±2.2 −2		4.8 ±1.3 −1		1.30±.38 E0
539					1.32±.41 E0
556	8.1 ±2.2 −2				
558			3.67±.75 −1		7.3 ±2.1 −1
599			2.59±.66 −1		8.2 ±2.4 −1
647			6.2 ±3.6 −2		
651					2.32±.71 −1
652			5.3 ±2.5 −2		
700					1.18±.55 −1
743			1.92±.74 −2		4.2 ±2.5 −2
800			9.7 ±5.6 −3		

TABLE VIII. π^- production cross sections from 0.80 GeV protons.

Mom (MeV/c)	C	Al	Cu	Sn	Pb
		$\frac{d^2\sigma}{d\Omega dp}\left(\frac{\text{mb}}{\text{sr-GeV/c}}\right)$ in form $(\sigma\pm\text{err})\times10^{\text{exp}}$			
189			3.68±.38 E0		
191	8.5 ±1.2 −1				7.78±.85 E0
200			3.39±.36 E0		
201					7.34±.86 E0
202	9.1 ±1.3 −1				
211			2.57±.30 E0		
213					6.94±.85 E0
214	9.8 ±1.5 −1				
283					7.8 ±1.2 −1
284	8.1 ±1.5 −2				
285			3.04±.44 −1		
296					5.9 ±1.0 −1
298	8.0 ±1.3 −2				
299			2.19±.34 −1		
312					4.54±.98 −1
314	4.3 ±1.3 −2				
315			1.75±.36 −1		

TABLE IX. π^- production cross sections from 1.05 GeV protons.

Mom (MeV/c)	C	Al	Cu	Sn	Pb
		$\frac{d^2\sigma}{d\Omega dp}\left[\frac{mb}{sr-GeV/c}\right]$ in form $(\sigma \pm err)\times 10^{exp}$			
184		2.31±.49 E0		6.9 ±1.0 E0	
187	1.68±.23 E0		5.71±.55 E0		1.36±.13 E1
193		1.57±.42 E0			
194				4.90±.87 E0	
197			5.77±.57 E0		1.22±.13 E1
198	1.55±.22 E0				
205		1.72±.40 E0		4.72±.82 E0	
209			5.41±.54 E0		1.23±.13 E1
210	1.66±.25 E0				
230		8.9 ±2.8 −1		3.22±.58 E0	
242		4.0 ±2.5 −1		1.82±.48 E0	
255		6.5 ±2.3 −1		2.08±.45 E0	
281	1.37±.23				
283	1.53±.33 −1				
283	1.92±.27 −1		7.20±.72 −1		2.17±.27 E0
284			7.9 ±1.1 −1		1.76±.18 E0
295	1.34±.23 −1				
297			5.29±.53 −1		
298	1.61±.36 −1				
298	1.46±.24 −1		7.6 ±1.1 −1		1.60±.23 E0
298					1.42±.15 E0
311	6.0 ±2.1 −2				
314	7.0 ±3.8 −2				
314	9.4 ±2.4 −2		4.50±.94 −1		
314			4.48±.56 −1		1.25±.23 E0
315					1.24±.15 E0
380	1.47±.85 −2				
381			1.05±.15 −1		2.52±.39 −1
398	1.49±.35 −2				
399			8.2 ±1.1 −2		1.78±.25 −1
418	6.7 ±6.1 −3				
419			5.4 ±1.1 −2		1.39±.28 −1

TABLE X. π^- production cross sections from 2.10 GeV protons.

Mom (MeV/c)	C	Al	Cu	Sn	Pb
		$\frac{d^2\sigma}{d\Omega dp}\left\{\frac{\text{mb}}{\text{sr-GeV/c}}\right\}$ in form $(\sigma\pm\text{err})\times10^{\text{exp}}$			
181			1.80±.19 E1		
184				2.48±.25 E1	
186	3.73±.47 E0	7.25±.83 E0			4.04±.38 E1
191			1.53±.16 E1		
194				1.95±.21 E1	
196					3.55±.34 E1
197	2.85±.42 E0	6.62±.79 E0			
203			1.81±.18 E1		
207				2.26±.25 E1	
209					3.52±.35 E1
210	2.77±.46 E0	7.13±.90 E0			
279					9.4 ±1.0 E0
280	7.9 ±1.4 −1	1.65±.27 E0	3.95±.42 E0		
280			3.78±.35 E0	5.37±.64 E0	
295	6.3 ±1.2 −1		3.42±.38 E0		
295			2.98±.29 E0		7.77±.90 E0
296		1.58±.23 E0		4.04±.52 E0	
312					7.46±.93 E0
313	6.5 ±1.5 −1		2.31±.31 E0		
313			2.07±.22 E0		
314		1.04±.24 E0		2.67±.49 E0	
374				1.82±.21 E0	2.93±.29 E0
375	1.84±.33 −1	5.84±.67 −1	1.17±.12 E0		
394				1.62±.20 E0	2.30±.24 E0
395	1.12±.25 −1	4.08±.70 −1	8.06±.89 −1		
416				6.3 ±1.4 −1	1.79±.21 E0
416	1.32±.32 −1	2.72±.66 −1	4.93±.70 −1		
466	4.0 ±1.4 −2		2.70±.45 −1	4.71±.84 −1	
469		1.72±.37 −1			9.4 ±1.4 −1
491	3.6 ±1.3 −2			3.45±.72 −1	
492		6.5 ±2.2 −2	1.57±.33 −1		4.17±.87 −1
516			8.5 ±2.5 −2	1.51±.49 −1	
519		2.5 ±1.5 −2			2.71±.73 −1
567				5.8 ±2.7 −2	8.1 ±3.6 −2
568			5.7 ±1.6 −2		
595			1.85±.84 −2	4.9 ±2.2 −2	4.0 ±2.3 −2
626					8.2 ±3.7 −2

TABLE XI. π^- production cross sections from 4.89 GeV protons.

Mom (MeV/c)	C	Al	Cu	Sn	Pb
		$\frac{d^2\sigma}{d\Omega dp}\left[\frac{\text{mb}}{\text{sr-GeV/c}}\right]$ in form $(\sigma \pm \text{err}) \times 10^{\text{exp}}$			
188	8.87±.71 E0		3.12±.28 E1		8.50±.74 E1
200	7.17±.74 E0		3.36±.30 E1		8.74±.76 E1
213	7.48±.80 E0				8.49±.76 E1
214			3.38±.31 E1		
235	3.64±.38 E0		1.89±.17 E1		4.62±.42 E1
250	3.42±.38 E0		1.64±.15 E1		4.17±.38 E1
266	2.52±.35 E0				
267			1.39±.13 E1		3.39±.33 E1
282	1.80±.16 E0				
283	1.98±.22 E0		9.30±.85 E0		2.39±.22 E1
300	1.40±.20 E0				
300	1.28±.14 E0		7.38±.71 E0		1.88±.19 E1
319	1.15±.13 E0		6.74±.67 E0		
320	1.35±.19 E0				1.84±.19 E1
377			3.06±.28 E0		
378	6.16±.62 −1				9.05±.91 E0
400			2.46±.23 E0		8.22±.86 E0
401	4.65±.50 −1				
425			2.23±.23 E0		
426					7.14±.81 E0
427	3.62±.46 −1				
473	1.12±.26 −1		1.02±.12 E0		3.76±.41 E0
474	1.61±.21 −1				
501	9.5 ±2.2 −2		7.54±.97 −1		2.33±.30 E0
502	9.5 ±1.5 −2				
533	5.5 ±2.1 −2		4.22±.77 −1		1.29±.23 E0
534	6.0 ±1.4 −2				
569	2.77±.68 −2				9.6 ±1.2 −1
570			2.38±.46 −1		
570			2.52±.31 −1		
571					8.5 ±1.4 −1
602	2.01±.66 −2				4.94±.82 −1
603			1.78±.43 −1		
603			1.34±.23 −1		
604					4.1 ±1.1 −1
639					2.85±.68 −1
640	9.0 ±5.3 −3		1.35±.41 −1		
640			7.7 ±1.8 −2		
641					2.62±.96 −1
667			3.90±.79 −2		
668	6.7 ±2.4 −3				1.59±.26 −1
705	5.5 ±2.1 −3		2.59±.84 −2		
706					7.5 ±1.7 −2

TABLE XI (continued).

Mom (MeV/c)	C	Al	Cu	Sn	Pb
		$\frac{d^2\sigma}{d\Omega dp}\left[\frac{\text{mb}}{\text{sr-GeV/c}}\right]$ in form $(\sigma\pm\text{err})\times10^{\text{exp}}$			
747			7.3 ±3.7 −3		
749					4.8 ±1.5 −2
764					2.09±.87 −2
807					1.1 ±1.4 −2

TABLE XII. π^+ production cross sections from 1.05 GeV/A alphas.

Mom (MeV/c)	C	Al	Cu	Sn	Pb
		$\frac{d^2\sigma}{d\Omega dp}\left[\frac{\text{mb}}{\text{sr-GeV/c}}\right]$ in form $(\sigma\pm\text{err})\times10^{\text{exp}}$			
180	9.9 ±1.2 E0	1.94±.21 E1	3.99±.36 E1	5.47±.53 E1	8.43±.79 E1
192	6.3 ±1.0 E0	1.64±.18 E1	2.96±.28 E1	4.40±.44 E1	7.02±.68 E1
206	6.41±.97 E0	1.44±.18 E1	2.83±.28 E1	4.66±.48 E1	6.91±.69 E1
268	1.50±.26 E0	3.01±.47 E0			
269			6.79±.71 E0	9.6 ±1.2 E0	2.02±.21 E1
287	7.3 ±1.9 −1	1.98±.37 E0		5.56±.81 E0	1.09±.14 E1
288			4.24±.50 E0		
295	9.2 ±2.8 −1	2.14±.54 E0			1.26±.19 E1
296			4.13±.65 E0	7.0 ±1.2 E0	
308	6.2 ±1.6 −1	1.52±.31 E0		5.36±.80 E0	7.5 ±1.1 E0
309			3.05±.41 E0		
315	6.4 ±2.1 −1	1.89±.47 E0			
316			2.30±.46 E0	2.29±.69 E0	7.9 ±1.4 E0
339	6.9 ±2.5 −1				3.8 ±1.1 E0
340			1.56±.42 E0	1.82±.70 E0	
355			1.34±.17 E0		
356		7.1 ±1.2 −1		1.84±.26 E0	
357	1.97±.56 −1				3.29±.42 E0
379			4.91±.86 −1		
381				9.4 ±1.8 −1	
382	7.7 ±3.5 −2	2.93±.73 −1			1.32±.23 E0
384	1.41±.59 −1		7.7 ±2.1 −1	9.7 ±3.5 −1	1.47±.48 E0
385		5.1 ±.7 −1			
408			4.21±.81 −1		
410		2.56±.69 −1		6.4 ±1.5 −1	
411	7.4 ±3.1 −2				1.05±.21 E0
412			1.6 ±1.1 −1		7.7 ±3.8 −1
413		1.7 ±1.3 −1			
443			3.26±.84 −1	4.3 ±1.1 −1	
444	9.6 ±5.6 −2		3.5 ±1.8 −1		8.9 ±1.7 −1
444					1.40±.54 E0
475			1.60±.42 −1		
476				9.5 ±5.4 −2	
477					1.49±.80 −1
512			7.6 ±3.1 −2	1.20±.61 −1	
513					2.2 ±1.0 −1
568			4.4 ±2.6 −2		

TABLE XIII. π^+ production cross sections from 2.10 GeV/A alphas.

Mom (MeV/c)	C	Al	Cu	Sn	Pb
		$\frac{d^2\sigma}{d\Omega dp}\left[\frac{mb}{sr-GeV/c}\right]$ in form $(\sigma\pm err)\times 10^{exp}$			
182	1.41±.16 E1	3.27±.34 E1	8.98±.66 E1	9.57±.96 E1	1.73±.16 E2
194	1.47±.17 E1	2.87±.31 E1	6.93±.66 E1	6.68±.90 E1	1.62±.16 E2
208	1.34±.18 E1	2.75±.33 E1	6.79±.67 E1	8.81±.97 E1	1.66±.17 E2
271		7.5 ±1.0 E0			
272	3.48±.53 E0				4.06±.54 E1
273			1.79±.21 E1	2.43±.35 E1	4.85±.48 E1
274	4.02±.50 E0	7.02±.84 E0	1.66±.17 E1	2.73±.27 E1	
290	2.44±.49 E0	6.07±.95 E0			
291			1.14±.18 E1	1.81±.31 E1	2.84±.45 E1
292	3.00±.41 E0	5.57±.72 E0	1.16±.13 E1	1.30±.20 E1	3.56±.38 E1
311		3.98±.78 E0			
312	2.70±.48 E0		1.14±.17 E1	1.57±.30 E1	2.64±.45 E1
313	1.78±.34 E0	3.75±.62 E0	1.00±.12 E1	1.37±.17 E1	2.32±.29 E1
361	7.6 ±2.2 −1		3.70±.73 E0	8.2 ±1.5 E0	8.8 ±2.2 E0
362		2.34±.47 E0			
363			5.15±.54 E0		
364	9.7 ±1.3 −1	2.20±.26 E0		8.17±.95 E0	1.35±.14 E1
386	7.8 ±2.4 −1		3.36±.72 E0	2.66±.91 E0	1.02±.24 E1
387		1.19±.38 E0			
388	7.5 ±1.2 −1	1.43±.20 E0	3.40±.40 E0	5.45±.72 E0	9.7 ±1.1 E0
414				4.5 ±1.3 E0	5.9 ±2.0 E0
415	3.1 ±2.0 −1		2.94±.75 E0		
416		6.3 ±3.3 −1			
417	2.7 ±1.1 −1	9.0 ±1.9 −1	2.56±.36 E0	3.50±.63 E0	7.6 ±1.0 E0
450			2.14±.40 E0		
451	2.41±.85 −1	5.3 ±1.5 −1		3.19±.69 E0	6.5 ±1.4 E0
454	2.34±.59 −1	6.2 ±1.3 −1	1.48±.19 E0	2.48±.38 E0	3.24±.47 E0
458	2.13±.50 −1				
481			8.7 ±2.4 −1		
482	2.00±.72 −1				3.10±.96 E0
483		3.4 ±1.2 −1		1.48±.46 E0	
485	1.15±.52 −1	2.27±.91 −1	8.1 ±1.4 −1	1.18±.27 E0	2.74±.44 E0
490	5.3 ±3.5 −2				
518			4.5 ±1.9 −1		
519	6.9 ±4.0 −2				
520		2.21±.92 −1		8.0 ±3.6 −1	
522		2.52±.97 −1	6.5 ±1.3 −1	1.12±.28 E0	1.69±.36 E0
528	7.8 ±1.9 −2				
550			1.98±.77 −1		
551			2.91±.79 −1		
552			2.68±.69 −1		
553			2.78±.78 −1		
561	3.9 ±1.8 −2	7.8 ±3.9 −2			
562					8.7 ±3.0 −1
564				3.0 ±1.3 −1	

TABLE XIII (continued).

Mom (MeV/c)	C	Al	Cu	Sn	Pb
		$\frac{d^2\sigma}{d\Omega dp}\left[\frac{\text{mb}}{\text{sr-GeV/c}}\right]$ in form $(\sigma \pm \text{err}) \times 10^{\text{exp}}$			
591			8.9 ±5.8 −2		
592			8.4 ±4.7 −2		
593			1.43±.54 −1		
594			8.9 ±4.8 −2		
607				2.0 ±1.4 −1	
639			6.1 ±4.5 −2		
639			7.4 ±5.5 −2		
652			5.7 ±3.3 −2		3.2 ±1.2 −1
702			5.9 ±3.5 −2		
786			1.47±.88 −2		

TABLE XIV. π^- production cross sections from 1.05 GeV/A alphas.

Mom (MeV/c)	C	Al	Cu	Sn	Pb
		$\frac{d^2\sigma}{d\Omega dp}\left[\frac{\text{mb}}{\text{sr-GeV/c}}\right]$ in form $(\sigma\pm\text{err})\times10^{exp}$			
183		1.71±.18 E1		4.92±.47 E1	8.10±.76 E1
184	7.92±.97 E0		3.28±.30 E1		
195	7.32±.92 E0	1.65±.17 E1	3.35±.30 E1	4.55±.44 E1	7.98±.75 E1
207	7.8 ±1.1 E0	1.68±.19 E1	3.27±.30 E1	5.15±.51 E1	6.98±.70 E1
274		2.59±.30 E0			
275	1.06±.14 E0				
276			4.59±.46 E0	7.09±.77 E0	1.02±.10 E1
290		1.37±.20 E0			
291	8.1 ±1.1 −1				
292			3.07±.34 E0	4.43±.58 E0	7.87±.83 E0
307		1.20±.19 E0			
308	6.5 ±1.0 −1				
309					6.21±.72 E0
310			2.25±.29 E0	3.94±.54 E0	
366			8.6 ±1.0 −1	1.20±.18 E0	
367	1.43±.42 −1	2.41±.65 −1			1.72±.24 E0
386			4.60±.69 −1	7.7 ±1.4 −1	
387	4.3 ±2.9 −2	2.75±.65 −1			1.34±.20 E0
408			2.88±.55 −1		
409	5.8 ±2.7 −2			5.8 ±1.2 −1	
410		2.79±.65 −1			9.3 ±1.7 −1
460		4.3 ±1.5 −2			3.96±.63 −1
461			1.25±.31 −1		
461			1.06±.16 −1	1.77±.33 −1	
484		2.0 ±1.0 −2			2.24±.44 −1
485			6.2 ±2.1 −2		
485			6.0 ±1.3 −2	1.08±.24 −1	
511	9.5 ±4.8 −3	1.61±.82 −2			8.0 ±2.6 −2
512			5.3 ±1.9 −2		
512			3.60±.98 −2	5.0 ±1.6 −2	
553			1.64±.51 −2		4.6 ±1.4 −2
581			7.7 ±3.5 −3		1.98±.90 −2

TABLE XV. π^- production cross sections from 2.10 GeV/A alphas.

Mom (MeV/c)	C	Al	Cu	Sn	Pb
		$\frac{d^2\sigma}{d\Omega dp}\left[\frac{\text{mb}}{\text{sr-GeV/c}}\right]$ in form $(\sigma\pm\text{err})\times10^{\text{exp}}$			
184	1.17±.16 E1	2.83±.33 E1	6.09±.58 E1	1.08±.11 E2	1.43±.14 E2
198	1.25±.16 E1	2.75±.32 E1	5.10±.50 E1	8.51±.91 E1	1.24±.12 E2
209	1.13±.17 E1	1.89±.28 E1	4.85±.51 E1	7.90±.92 E1	1.24±.13 E2
280	2.98±.50 E0	7.04±.98 E0	1.43±.14 E1	2.44±.26 E1	4.21±.43 E1
297	3.20±.50 E0	5.67±.63 E0	1.17±.12 E1	1.64±.21 E1	3.09±.34 E1
316					2.57±.31 E1
317	1.98±.49 E0	5.11±.92 E0	1.06±.12 E1	1.86±.23 E1	
370			4.32±.49 E0		
371	1.06±.19 E0	2.44±.38 E0		8.00±.95 E0	1.17±.13 E1
392		1.12±.27 E0	3.06±.39 E0		
393	3.5 ±1.3 −1			4.20±.65 E0	9.1 ±1.1 E0
416			2.16±.38 E0		
417	2.9 ±1.7 −1	8.1 ±3.0 −1		3.09±.66 E0	6.5 ±1.0 E0
469			9.1 ±1.5 −1	1.40±.33 E0	
496			5.7 ±1.2 −1	1.29±.34 E0	
527			3.9 ±1.1 −1	6.5 ±3.1 −1	
573			1.26±.43 −1		
573			1.33±.29 −1	2.56±.60 −1	4.76±.84 −1
606			9.2 ±2.3 −2	1.21±.38 −1	2.30±.55 −1
644			2.4 ±1.7 −2	6.2 ±4.3 −2	9.9 ±4.9 −2

TABLE XVI. π^+ production cross sections from 0.40 GeV/A carbon.

Mom (MeV/c)	C	Al	Cu	Sn	Pb
		$\frac{d^2\sigma}{d\Omega dp}\left[\frac{\text{mb}}{\text{sr-GeV/c}}\right]$ in form $(\sigma\pm\text{err})\times10^{\text{exp}}$			
184					1.81±.23 E1
185	2.00±.24 E0		8.8 ±1.0 E0		
198			7.03±.91 E0		1.80±.23 E1
199	1.27±.18 E0				
214			6.49±.97 E0		1.38±.22 E1
215	1.44±.22 E0				
230			3.15±.37 E0		7.82±.93 E0
231	6.15±.77 −1				
246			2.00±.29 E0		
247					5.62±.79 E0
248	3.92±.63 −1				
268			1.34±.23 E0		
267					3.20±.57 E0
269	2.38±.47 −1				
275			1.11±.43 E0		
275			1.23±.45 E0		
280			5.41±1.0 −1		
286	1.11±.23 −1				
287					1.51±.32 E0
296			9.1 ±4.1 −1		
296			5.3 ±3.1 −1		
302			3.9 ±1.1 −1		
309	6.9 ±2.9 −2				
311					9.6 ±3.6 −1
321			6.9 ±4.0 −1		
328			3.22±.90 −1		
336	5.3 ±1.9 −2				

TABLE XVII. π^+ production cross sections from 1.05 GeV/A carbon.

Mom (MeV/c)	C	Al	Cu	Sn	Pb
		$\frac{d^2\sigma}{d\Omega dp}\left[\frac{mb}{sr-GeV/c}\right]$ in form $(\sigma\pm err)\times 10^{exp}$			
188	1.73±.13 E1	3.42±.31 E1	7.20±.66 E1		
189				1.15±.11 E2	1.86±.17 E2
201		3.43±.31 E1	7.65±.70 E1		
202	1.63±.16 E1			1.11±.11 E2	1.83±.17 E2
216		3.20±.30 E1			
217	1.57±.16 E1		7.77±.73 E1		
218				1.07±.11 E2	1.82±.17 E2
276	2.96±.46 E0				
277		6.44±.97 E0	1.54±.18 E1	2.64±.32 E1	4.30±.54 E1
278		6.57±.61 E0			
281		5.1 ±1.3 E0			
295	1.88±.45 E0				
296			1.13±.15 E1	1.69±.26 E1	2.79±.42 E1
297		3.89±.86 E0			
298		5.01±.79 E0			
301		2.7 ±1.2 E0			
318	1.52±.46 E0				
319			8.3 ±1.4 E0		2.00±.39 E1
320		3.58±.93 E0		1.42±.26 E1	
321		3.71±.77 E0			
325		4.1 ±1.6 E0			
366			3.2 ±1.1 E0		
367		1.57±.37 E0		5.5 ±1.1 E0	
368	3.4 ±1.4 −1				7.9 ±1.4 E0
369			2.12±.50 E0		
392			2.6 ±1.0 E0		
393				3.40±.87 E0	
394		5.1 ±1.8 −1			6.9 ±1.3 E0
395	3.19±.96 −1				
396			2.15±.50 E0		
424				1.57±.78 E0	
426					2.72±1.0 E0
428			1.60±.53 E0		
465			4.3 ±2.2 −1		

TABLE XVIII. π^+ production cross sections from 2.10 GeV/A carbon.

Mom (MeV/c)	C	Al	Cu	Sn	Pb
		$\frac{d^2\sigma}{d\Omega dp}\left[\frac{mb}{sr-GeV/c}\right]$ in form $(\sigma\pm err)\times10^{exp}$			
184		6.93±.68 E1	1.76±.15 E2	2.55±.24 E2	4.27±.38 E2
196			1.82±.16 E2		
197		8.09±.79 E1		2.65±.25 E2	4.66±.42 E2
211		6.25±.84 E1	1.81±.16 E2	3.01±.29 E2	4.96±.46 E2
276		1.99±.20 E1	4.68±.40 E1	6.86±.67 E1	1.38±.14 E2
277	8.18±.84 E0				
278	7.65±.97 E0	1.65±.20 E1	4.51±.48 E1	6.62±.81 E1	1.44±.16 E2
294			3.84±.33 E1		
295	6.65±.74 E0	1.53±.16 E1		6.23±.64 E1	1.05±.11 E2
297	8.11±.98 E0		3.71±.42 E1	6.44±.82 E1	9.6 ±1.2 E1
298		1.62±.19 E1			
316			3.31±.29 E1		
317	5.70±.69 E0	1.41±.16 E1		5.68±.61 E1	9.8 ±1.1 E1
319			2.93±.38 E1	4.89±.74 E1	9.5 ±1.3 E1
320	6.16±.91 E0	1.38±.19 E1			
367	1.96±.36 E0	5.34±.89 E0			3.14±.67 E1
368				2.40±.34 E1	
369			1.39±.21 E1		
371	2.40±.26 E0	5.33±.56 E0			4.03±.36 E1
373			1.24±.12 E1	2.00±.20 E1	
393	1.17±.31 E0	2.94±.70 E0		1.45±.26 E1	3.14±.69 E1
394			1.29±.21 E1		
397	1.30±.18 E0	3.99±.46 E0			2.97±.30 E1
398			1.05±.10 E1	1.79±.19 E1	
422	5.5 ±3.1 −1	2.47±.75 E0			
423				1.39±.28 E1	1.78±.59 E1
424			6.0 ±1.5 E0		
427	8.5 ±1.6 −1				2.23±.25 E1
428		2.72±.40 E0	7.50±.83 E0	1.03±.13 E1	
461			3.15±.71 E0		
462			4.17±.50 E0		
475	5.8 ±1.4 −1				
479		1.27±.32 E0	5.0 ±1.0 E0	5.3 ±1.4 E0	9.9 ±2.1 E0
494			2.36±.64 E0		
495			2.36±.34 E0		
511	8.1 ±1.7 −1				
515		9.8 ±2.9 −1	1.94±.69 E0	3.5 ±1.3 E0	
516					6.6 ±1.9 E0
532			1.72±.33 E0		
533			2.15±.70 E0		
541		4.1 ±1.3 −1			
542	1.06±.48 −1				

TABLE XVIII (continued).

Mom (MeV/c)	C	Al	Cu	Sn	Pb
		$\frac{d^2\sigma}{d\Omega dp}\left[\frac{mb}{sr-GeV/c}\right]$ in form $(\sigma\pm err)\times 10^{exp}$			
549				1.73±.54 E0	
550			9.6 ±2.4 −1		
552	2.0 ±1.2 −1				
553					3.71±.94 E0
557		8.3 ±3.2 −1	1.93±.79 E0	2.5 ±1.2 E0	3.5 ±1.6 E0
579		1.83±.74 −1			
581	5.0 ±2.5 −2				
589			2.4 ±1.2 −1	6.8 ±3.5 −1	
594					9.6 ±4.9 −1
624		2.1 ±1.2 −1			
625			2.46±.96 −1	3.4 ±1.9 −1	
627	2.8 ±2.4 −2	7.3 ±4.3 −2			
628					7.3 ±3.2 −1
635				1.25±.56 E0	
636			5.8 ±2.3 −1		
670		4.1 ±2.4 −2			
671	5.2 ±2.2 −2		9.8 ±5.7 −2	2.8 ±1.6 −1	
735			6.6 ±3.6 −2		
737					3.6 ±1.4 −1
739				1.35±.70 −1	

TABLE XIX. π^- production cross sections from 0.40 GeV/A carbon.

Mom (MeV/c)	C	Al	Cu	Sn	Pb
		$\frac{d^2\sigma}{d\Omega dp}\left[\frac{mb}{sr-GeV/c}\right]$ in form $(\sigma\pm err)\times 10^{exp}$			
188	1.85±.26 E0		5.96±.86 E0		1.65±.25 E1
199	1.17±.23 E0				1.40±.25 E1
200			5.76±.91 E0		
211	1.32±.24 E0				1.27±.23 E1
212			5.40±.88 E0		
236	3.8 ±1.1 −1		2.28±.45 E0		
236			2.07±.36 E0		3.3 ±1.1 E0
236					4.42±.87 E0
249			1.91±.39 E0		
249			2.10±.36 E0		3.10±.95 E0
249					4.51±.87 E0
250	2.80±.88 −1				
263					2.99±.71 E0
264	1.87±.72 −1		6.6 ±2.3 −1		
264			1.33±.29 E0		2.82±.92 E0
264			4.13±.93 −1		
285	1.37±.57 −1				9.5 ±2.4 −1
299			1.82±.79 −1		
300					7.9 ±2.7 −1
301	9.5 ±5.7 −2				
317	1.59±.72 −1		2.11±.77 −1		8.3 ±2.3 −1

TABLE XX. π^- production cross sections from 1.05 GeV/A carbon.

Mom (MeV/c)	C	Al	Cu	Sn	Pb
		$\frac{d^2\sigma}{d\Omega dp}\left[\frac{\text{mb}}{\text{sr-GeV/c}}\right]$ in form $(\sigma\pm\text{err})\times10^{\text{exp}}$			
183			7.83±.71 E1		
185		3.73±.32 E1			1.94±.18 E2
186	1.69±.17 E1			1.32±.12 E2	
193			8.75±.80 E1		
196		3.73±.32 E1			2.10±.19 E2
197	1.82±.17 E1			1.29±.12 E2	
205			8.78±.82 E1		
208		4.07±.35 E1			2.06±.19 E2
209	1.96±.18 E1			1.29±.12 E2	
277					3.48±.31 E1
278	2.77±.25 E0	6.31±.57 E0	1.46±.13 E1	2.37±.22 E1	
292					2.62±.24 E1
293	1.97±.19 E0	4.79±.45 E0		1.70±.16 E1	
294			1.12±.10 E1		
310	1.65±.17 E0				2.32±.23 E1
311		3.61±.37 E0	9.23±.90 E0	1.37±.14 E1	
365	4.61±.48 −1				
366				4.76±.48 E0	
368		1.08±.11 E0			7.81±.77 E0
369			2.70±.26 E0		
384	2.93±.34 −1				
386				3.75±.39 E0	
387					5.57±.56 E0
388		6.00±.65 −1			
389			1.74±.16 E0		
405	2.35±.31 −1				
407				2.33±.29 E0	
409					4.52±.51 E0
410		5.53±.69 −1			
411			1.38±.17 E0		
461		1.96±.33 −1	5.79±.73 −1		
462	6.1 ±1.4 −2				2.20±.26 E0
463				1.17±.16 E0	
484		1.30±.28 −1	3.58±.56 −1		
486	4.3 ±1.1 −2				1.03±.16 E0
487				3.98±.92 −1	
510			1.01±.28 −1		
512		4.2 ±1.6 −2			
513					5.0 ±1.1 −1
514	2.25±.83 −2			5.4 ±1.1 −1	
553			1.28±.29 −1		
554				9.3 ±5.4 −2	4.2 ±1.9 −1
558	1.69±.55 −2				

TABLE XX (continued).

Mom (MeV/c)	C	Al	Cu	Sn	Pb
		$\frac{d^2\sigma}{d\Omega dp}\left[\frac{\text{mb}}{\text{sr-GeV/c}}\right]$ in form $(\sigma\pm\text{err})\times10^{\text{exp}}$			
581			7.5 ±2.2 −2		
582				9.7 ±5.6 −2	
583	9.0 ±4.1 −3				
611			5.7 ±2.1 −2		
654			1.27±.74 −2		

TABLE XXI. π^- production cross sections from 2.10 GeV/A carbon.

Mom (MeV/c)	C	Al	Cu	Sn	Pb
		$\frac{d^2\sigma}{d\Omega dp}\left[\frac{mb}{sr-GeV/c}\right]$ in form $(\sigma\pm err)\times10^{exp}$			
185	2.87±.28 E1	6.54±.60 E1		2.52±.24 E2	4.21±.37 E2
188			1.53±.13 E2		
189	3.25±.34 E1		1.58±.14 E2		4.33±.39 E2
196	2.60±.28 E1				
197		5.94±.57 E1		2.44±.24 E2	3.83±.35 E2
198			1.47±.13 E2		
201			1.58±.14 E2		
202	2.68±.35 E1				4.24±.39 E2
209	2.68±.28 E1				
210		6.02±.58 E1		2.25±.23 E2	3.69±.34 E2
211			1.44±.13 E2		
215	3.09±.38 E1		1.49±.14 E2		3.96±.37 E2
280	8.35±.80 E0	1.82±.17 E1	4.31±.40 E1	7.22±.66 E1	1.16±.11 E2
284	7.85±.97 E0		3.90±.37 E1		1.14±.10 E2
297	7.21±.74 E0	1.56±.15 E1	3.56±.34 E1	6.16±.59 E1	9.61±.91 E1
302	5.19±.88 E0		3.19±.33 E1		9.32± 89 E1
316	5.68±.63 E0			4.89±.51 E1	9.07±.89 E1
317		1.33±.14 E1	3.02±.31 E1		
321			2.83±.31 E1		
322	5.68±.93 E0				7.58±.78 E1
371			1.36±.12 E1		
372	2.16±.21 E0				3.98±.37 E1
373	1.94±.21 E0				
374		4.86±.47 E0		2.37±.23 E1	
378	1.00±.30 E0				
379	1.62±.20 E0		1.24±.13 E1		3.37±.35 E1
393			9.94±.92 E0		
394	1.66±.17 E0				3.05±.30 E1
395	1.59±.19 E0				
396				1.47±.16 E1	
397		3.44±.36 E0			
402	6.7 ±3.2 −1				
402	1.54±.21 E0		6.49±.99 E0		2.54±.29 E1
418			7.92±.78 E0		
419	1.21±.14 E0				2.33±.25 E1
420	1.00±.15 E0				
422		2.78±.32 E0		1.29±.15 E1	
428	1.23±.19 E0		6.64±.88 E0		1.82±.25 [illegible]
464		1.23±.13 E0			
465	3.75±.54 −1			6.54±.67 E0	1.20±.11 E1
467			3.42±.35 E0		
474	1.79±.84 −1				9.6 ±1.1 E0
475			2.76±.39 E0		

TABLE XXI (continued).

Mom (MeV/c)	C	Al	Cu	Sn	Pb
		$\frac{d^2\sigma}{d\Omega dp}\left[\frac{mb}{sr-GeV/c}\right]$ in form $(\sigma\pm err)\times 10^{exp}$			
492	2.54±.44 −1	7.21±.94 −1		4.26±.49 E0	7.60±.79 E0
494			2.05±.24 E0		
503	6.1 ±7.2 −2		2.19±.36 E0		6.68±.93 E0
522		5.29±.61 −1		2.69±.37 E0	
523	2.36±.44 −1				5.05±.61 E0
525			1.28±.19 E0		
534	9.6 ±7.0 −2				4.70±.80 E0
535			8.2 ±2.3 −1		
570			5.34±.88 −1		2.19±.30 E0
571	3.7 ±2.0 −2				
571	5.4 ±1.8 −2				
604			2.76±.67 −1		1.15±.22 E0
605	4.3 ±1.9 −2				
642	5.6 ±4.4 −2		1.71±.64 −1		9.0 ±2.2 −1
665					2.39±.75 −1
704			5.8 ±2.2 −2		1.34±.61 −1

TABLE XXII. π^+ production cross sections from 1.05 GeV/A argon.

Mom (MeV/c)	C	Al	Cu	Sn	Pb
		$\frac{d^2\sigma}{d\Omega dp}\left[\frac{mb}{sr-GeV/c}\right]$ in form $(\sigma\pm err)\times10^{exp}$			
197	2.82±.42 E1	6.58±.80 E1	1.61±.16 E2	2.46±.25 E2	4.09±.40 E2
203	3.25±.49 E1	6.44±.65 E1	1.57±.16 E2		4.50±.45 E2
204				2.42±.26 E2	
219	2.91±.50 E1	5.05±.60 E1	1.35±.15 E2	2.22±.26 E2	3.94±.41 E2
238	1.11±.17 E1	3.20±.45 E1	7.34±.77 E1	1.30±.14 E2	2.16±.21 E2
255	1.09±.17 E1	3.09±.46 E1	6.32±.72 E1	9.6 ±1.2 E1	2.17±.21 E2
272			3.24±.56 E1		
273	6.5 ±1.6 E0	6.4 ±2.5 E0		4.16±.99 E1	7.8 ±1.1 E1
275	9.7 ±1.8 E0	1.89±.40 E1	4.90±.64 E1	8.6 ±1.2 E1	1.40±.16 E2
284				5.24±.66 E1	7.97±.92 E1
285	6.4 ±1.1 E0	9.6 ±2.1 E0	2.93±.35 E1		
291			3.11±.57 E1		
292	3.2 ±1.3 E0	1.29±.31 E1		4.9 ±1.1 E1	5.73±.97 E1
305			2.37±.33 E1	3.26±.52 E1	6.74±.85 E1
306	2.10±.83 E0	1.05±.24 E1			
313			1.71±.47 E1		
314	3.8 ±2.0 E0			1.85±.88 E1	6.1 ±1.2 E1
315		4.2 ±3.0 E0			
329				1.99±.43 E1	4.79±.73 E1
330	3.88±.88 E0	6.7 ±2.1 E0	1.73±.29 E1		
364		1.59±.78 E0			
366	1.97±.69 E0		6.7 ±1.4 E0	8.5 ±2.4 E0	2.27±.53 E1
380			8.4 ±1.5 E0		
381					1.90±.31 E1
391		9.1 ±4.6 −1			
392	9.2 ±4.2 −1			3.5 ±1.5 E0	1.76±.48 E1
393			6.4 ±1.3 E0		
409	7.0 ±3.6 −1		1.85±.74 E0		1.24±.25 E1
421		9.3 ±5.4 −1			
423				6.8 ±2.3 E0	1.20±.44 E1
424			1.85±.77 E0		
442	1.10±.38 E0				
443			2.98±.94 E0		9.8 ±2.3 E0
459			9.5 ±3.7 −1	1.33±.78 E0	5.8 ±1.6 E0
460	2.8 ±1.6 −1	4.6 ±2.7 −1			
493			4.7 ±2.7 −1	1.54±.90 E0	2.4 ±1.1 E0
555				4.9 ±2.9 −1	
558					7.1 ±4.1 −1
600					8.4 ±4.9 −1

TABLE XXIII. π^+ production cross sections from 1.83 GeV/A argon.

Mom (MeV/c)	C	Al	Cu	Sn	Pb
		$\frac{d^2\sigma}{d\Omega dp}\left[\frac{mb}{sr-GeV/c}\right]$ in form $(\sigma\pm err)\times10^{exp}$			
188			3.22±.32 E2		
189	5.36±.90 E1	1.34±.19 E2		4.82±.52 E2	8.82±.82 E2
202			3.92±.39 E2		9.58±.90 E2
203	7.2 ±1.1 E1	1.52±.22 E2		5.34±.60 E2	
217			3.97±.41 E2		1.04±.10 E3
218	8.2 ±1.3 E1	1.58±.24 E2		5.85±.67 E2	
235	3.53±.52 E1	8.2 ±1.1 E1	1.70±.18 E2	2.59±.29 E2	4.95±.50 E2
251	2.90±.53 E1				
252		5.9 ±1.0 E1	1.67±.19 E2	2.17±.28 E2	4.91±.52 E2
270	2.24±.52 E1	8.1 ±1.1 E1			3.95±.47 E2
271			1.57±.19 E2	2.09±.29 E2	
277	1.40±.22 E1		8.58±.86 E1	1.32±.13 E2	2.59±.26 E2
278		2.69±.37 E1			
282	1.17±.30 E1	3.84±.58 E1	7.76±.89 E1		
282			7.98±.85 E1	1.21±.16 E2	2.48±.28 E2
283	1.65±.20 E1				
296	1.69±.23 E1				1.95±.21 E2
297		3.21±.40 E1	7.09±.74 E1	1.02±.11 E2	
302	1.38±.34 E1	2.41±.49 E1	6.15±.79 E1	1.16±.16 E2	2.20±.26 E2
303	1.21±.17 E1		7.19±.81 E1		
318					1.92±.22 E2
319	1.11±.22 E1	2.03±.36 E1	5.96±.70 E1	9.3 ±1.1 E1	
325	8.9 ±2.9 E0				
325	1.26±.19 E1	1.52±.41 E1	5.22±.75 E1	7.7 ±1.3 E1	1.80±.24 E2
326			6.13±.76 E1		
369					6.67±.96 E1
370	3.60±.90 E0	9.6 ±1.7 E0	2.20±.27 E1	4.83±.68 E1	
373			2.18±.24 E1	3.72±.43 E1	
375	3.98±.52 E0	8.4 ±1.1 E0			8.54±.91 E1
395					7.8 ±1.1 E1
398	2.69±.77 E0	7.2 ±1.5 E0	2.04±.27 E1	3.40±.56 E1	
400			1.80±.21 E1		
401				3.18±.41 E1	
403	2.95±.48 E0	5.98±.91 E0			6.26±.76 E1
426		3.7 ±1.6 E0	1.28±.23 E1	2.16±.53 E1	4.13±.87 E1
431			1.48±.20 E1	1.66±.30 E1	
434	1.90±.42 E0	4.22±.85 E0			3.17±.54 E1
458	5.2 ±3.6 −1	1.60±.61 E0			
459			7.0 ±1.1 E0	1.43±.28 E1	
460					2.03±.44 E1
466					1.96±.27 E1
467	8.9 ±2.2 −1	2.24±.49 E0		8.1 ±1.5 E0	
468			5.64±.83 E0		

TABLE XXIII (continued).

Mom (MeV/c)	C	Al	Cu	Sn	Pb
		$\frac{d^2\sigma}{d\Omega dp}\left[\frac{mb}{sr-GeV/c}\right]$ in form $(\sigma\pm err)\times 10^{exp}$			
490		2.04±.82 E0			
491	2.8 ±2.1 −1		3.45±.72 E0		
492				6.8 ±2.0 E0	
493					2.00±.45 E1
501	6.0 ±1.5 −1				1.38±.22 E1
502		1.11±.31 E0	4.32±.70 E0	6.8 ±1.3 E0	
529	4.9 ±4.0 −1		1.84±.87 E0		
530				3.0 ±1.7 E0	
531					5.8 ±2.9 E0
540	2.1 ±1.6 −1				9.7 ±2.1 E0
541		9.3 ±4.0 −1			
542			1.58±.52 E0	6.0 ±1.5 E0	
550		4.5 ±1.6 −1	2.37±.50 E0	2.96±.83 E0	4.4 ±1.2 E0
590	2.6 ±1.5 −1	2.6 ±1.3 −1	7.4 ±2.9 −1	2.70±.84 E0	4.4 ±1.3 E0
636		2.5 ±1.5 −1	5.4 ±2.7 −1	1.56±.71 E0	2.6 ±1.2 E0
662			3.6 ±1.8 −1		
712					6.7 ±3.9 −1
714				4.6 ±2.7 −1	
753					1.9 ±1.1 −1
760				3.7 ±1.4 −1	
761			1.26±.64 −1		
813					4.7 ±2.0 −1

TABLE XXIV. π^- production cross sections from 1.05 GeV/A argon.

Mom (MeV/c)	C	Al	Cu	Sn	Pb
		$\frac{d^2\sigma}{d\Omega dp}\left[\frac{\text{mb}}{\text{sr-GeV/c}}\right]$ in form $(\sigma\pm\text{err})\times10^{\text{exp}}$			
187	3.88±.57 E1	6.8 ±1.0 E1	1.81±.20 E2	2.67±.32 E2	4.36±.46 E2
198			1.69±.20 E2		
199	3.52±.61 E1	6.6 ±1.1 E1		2.68±.34 E2	5.11±.55 E2
211			1.90±.22 E2	2.85±.37 E2	
212	2.90±.55 E1	7.8 ±1.2 E1			4.71±.53 E2
234	1.75±.29 E1	3.53±.49 E1	9.1 ±1.7 E1		
234			7.92±.94 E1	1.31±.16 E2	
236					2.32±.26 E2
247			6.34±.82 E1		
248			6.1 ±1.4 E1	1.19±.16 E2	
249	1.28±.24 E1	3.00±.44 E1			
250					1.71±.22 E2
263			4.97±.78 E1		
264	7.5 ±2.4 E0	2.15±.44 E1	4.0 ±1.3 E1	1.00±.15 E2	
267					1.75±.24 E2
284					7.50±.95 E1
285	5.83±.88 E0	1.26±.23 E1	3.07±.37 E1	4.72±.63 E1	
301	1.29±.46 E1				7.28±.97 E1
302	5.62±.89 E0	1.00±.21 E1	2.86±.36 E1	4.46±.62 E1	
320	3.8 ±3.2 E0				
321	2.99±.71 E0	6.7 ±2.0 E0		3.84±.60 E1	5.37±.87 E1
322			1.96±.31 E1		
381			4.29±.68 E0		
382		1.81±.43 E0		9.3 ±1.6 E0	
383	7.8 ±2.3 −1				
384					1.70±.24 E1
404			4.02±.67 E0	7.1 ±1.4 E0	
405		1.63±.40 E0			
406	6.9 ±2.1 −1				1.28±.21 E1
429			2.64±.57 E0	5.5 ±1.3 E0	
431	5.5 ±2.0 −1	3.3 ±1.9 −1			1.09±.21 E1
480					3.51±.65 E0
507					1.70±.47 E0
537					1.02±.39 E0

TABLE XXV. π^- production cross sections from 1.83 GeV/A argon.

Mom (MeV/c)	C	Al	Cu	Sn	Pb
		$\frac{d^2\sigma}{d\Omega dp}\left[\frac{mb}{sr-GeV/c}\right]$ in form $(\sigma\pm err)\times10^{exp}$			
188	5.58±.68 E1	1.25±.14 E2	3.24±.29 E2	5.39±.50 E2	8.78±.77 E2
200	6.97±.83 E1	1.34±.15 E2	3.21±.29 E2	5.04±.48 E2	9.14±.81 E2
213	7.31±.91 E1	1.31±.16 E2			8.69±.79 E2
214			3.13±.29 E2	5.03±.49 E2	
235	3.55±.45 E1	7.42±.83 E1	1.77±.16 E2		
236				2.91±.28 E2	
237					4.85±.44 E2
250	2.78±.44 E1	7.29±.89 E1	1.48±.14 E2		
251				2.93±.29 E2	4.59±.43 E2
267	2.69±.44 E1	6.30±.83 E1	1.38±.14 E2		
268				2.60±.27 E2	3.88±.38 E2
283	1.78±.25 E1	3.78±.45 E1	9.16±.86 E1	1.49±.15 E2	2.81±.26 E2
300		2.91±.43 E1	7.88±.79 E1	1.23±.13 E2	
301	1.29±.25 E1				2.08±.21 E2
320		2.48±.41 E1	6.75±.72 E1	9.8 ±1.2 E1	
321	1.43±.27 E1				1.96±.20 E2
375					6.92±.82 E1
376	3.10±.58 E0	7.8 ±1.0 E0	2.49±.28 E1	4.46±.54 E1	
398					5.94±.76 E1
399	3.29±.65 E0	6.37±.96 E0	1.69±.23 E1	2.77±.43 E1	
423					5.59±.80 E1
424				2.63±.45 E1	
425	1.13±.49 E0	4.25±.85 E0	1.11±.19 E1		
472	7.1 ±1.3 −1	3.59±.47 E0		8.8 ±1.2 E0	2.08±.24 E1
473			5.81±.73 E0		
500					1.52±.20 E1
501	3.83±.94 −1	2.17±.38 E0	5.10±.72 E0	6.4 ±1.0 E0	
532	1.52±.59 −1	9.8 ±2.4 −1		3.81±.77 E0	7.2 ±1.3 E0
533			2.87±.52 E0		
558		6.7 ±2.0 −1			5.5 ±1.0 E0
567			1.12±.21 E0		
568				1.22±.34 E0	
590		5.0 ±1.8 −1			3.40±.79 E0
601			6.2 ±1.5 −1	9.5 ±2.6 −1	
626		3.8 ±1.5 −1			1.93±.63 E0
637			5.0 ±1.4 −1		
638				6.0 ±2.3 −1	

TABLE XXVI. π^+ production cross sections from 0.40 GeV/A neon.

Mom (MeV/c)	C	Al	Cu	Sn	Pb
		$\frac{d^2\sigma}{d\Omega dp}\left[\frac{\text{mb}}{\text{sr-GeV/c}}\right]$ in form $(\sigma\pm\text{err})\times10^{\text{exp}}$			
179			1.20±.24 E1	1.21±.40 E1	
181					3.85±.70 E1
190			8.3 ±1.8 E0	1.55±.39 E1	
193					1.29±.39 E1
204			7.5 ±1.9 E0	9.0 ±3.4 E0	
208					1.22±.44 E1
278			7.1 ±4.1 −1	1.27±.74 E0	
279					4.0 ±1.6 E0
299				1.6 ±1.1 E0	
300					2.2 ±1.5 E0

TABLE XXVII. Tabulation of the slopes and integrated cross sections for all the experimental conditions. $\left[\frac{d\sigma}{d\Omega} = \int_{100}^{600} \frac{d^2\sigma}{d\Omega dp} dT\right]$

Target	Fragment	Slope Parameter (MeV)	Intercept Parameter $\left[\frac{\text{mb-GeV}}{\text{sr-(GeV/c)}^3}\right]$	Integrated Cross Section (mb/sr)
		0.80 GeV p		
CD_2	π^-	24.2 ± 1.1	560 ± 160	.049 ± .018
Ag	π^+	39.5 ± 2.1	1330 ± 340	1.01 ± .33
Ag	π^-	26.4 ± 0.9	2240 ± 450	.303 ± .079
C	π^+	31.3 ± 1.0	511. ± 81.	.152 ± .032
C	π^-	25.7 ± 1.2	400 ± 120	.047 ± .018
Cu	π^+	33.5 ± 0.8	1470 ± 160	.582 ± .086
Cu	π^-	27.1 ± 1.0	940 ± 200	.145 ± .040
Pb	π^+	33.7 ± 0.8	3060 ± 360	1.24 ± .19
Pb	π^-	26.9 ± 1.1	2410 ± 570	.36 ± .11
		1.05 GeV p		
C	π^+	37.8 ± 1.2	255. ± 34.	.163 ± .029
C	π^-	31.1 ± 0.9	221. ± 33.	.064 ± .012
Al	π^+	34.5 ± 1.1	618. ± 89.	.276 ± .053
Al	π^-	33.8 ± 2.9	224. ± 63.	.090 ± .041
Cu	π^+	37.5 ± 0.8	884. ± 85.	.549 ± .069
Cu	π^-	36.0 ± 0.6	452. ± 36.	.240 ± .025
Sn	π^+	35.9 ± 1.0	1440 ± 180	.76 ± .13
Sn	π^-	35.4 ± 2.2	590 ± 110	.290 ± .092
Pb	π^+	40.7 ± 0.9	1480 ± 140	1.25 ± .16
Pb	π^-	36.3 ± 0.7	1070. ± 94	.586 ± .068
		2.10 GeV p		
C	π^+	46.6 ± 1.0	298. ± 30.	.404 ± .050
C	π^-	46.9 ± 1.5	150. ± 23.	.208 ± .039
Al	π^+	46.6 ± 0.9	585. ± 54.	.793 ± .089
Al	π^-	48.6 ± 1.3	330. ± 41.	.514 ± .078
Cu	π^+	50.6 ± 0.7	926. ± 60.	1.64 ± .13
Cu	π^-	49.9 ± 1.0	538. ± 52.	.91 ± .11
Sn	π^+	49.9 ± 0.9	1500 ± 130	2.55 ± .26
Sn	π^-	51.3 ± 1.2	796. ± 96.	1.48 ± .21
Pb	π^+	51.4 ± 0.8	2170 ± 160	4.05 ± .37
Pb	π^-	50.6 ± 0.9	1490 ± 130	2.65 ± .27
		3.50 GeV p		
Cu	π^+	54.8 ± 0.8	1240. ± 83.	2.82 ± .23

TABLE XXVII (continued).

Target	Fragment	Slope Parameter (MeV)	Intercept Parameter $\left[\frac{\text{mb-GeV}}{\text{sr-(GeV/c)}^3}\right]$	Integrated Cross Section (mb/sr)
		4.89 GeV p		
CH_2	π^-	51.2 ± 1.2	298. ± 27.	.549 ± .064
CD_2	π^-	49.7 ± 1.1	396. ± 34.	.664 ± .074
C	π^+	55.2 ± 1.4	268. ± 28.	.624 ± .080
C	π^-	53.8 ± 0.7	226. ± 15.	.486 ± .037
Cu	π^+	58.7 ± 0.9	1010. ± 63.	2.83 ± .22
Cu	π^-	57.2 ± 0.6	1010. ± 52.	2.62 ± .16
Pb	π^+	60.5 ± 0.9	2430 ± 160	7.43 ± .58
Pb	π^-	60.0 ± 0.6	2350 ± 120	7.02 ± .41
		1.05 GeV/A α		
C	π^+	34.0 ± 1.1	890 ± 130	.374 ± .074
C	π^-	32.9 ± 1.2	910 ± 190	.334 ± .088
Al	π^+	36.3 ± 1.0	1500 ± 180	.82 ± .13
Al	π^-	34.7 ± 0.9	1590 ± 250	.73 ± .14
Cu	π^+	37.9 ± 0.7	2430 ± 210	1.57 ± .17
Cu	π^-	37.0 ± 0.6	2300 ± 240	1.36 ± .16
Sn	π^+	36.7 ± 0.8	4140 ± 410	2.37 ± .31
Sn	π^-	36.1 ± 0.7	4140 ± 510	2.22 ± .32
Pb	π^+	37.9 ± 0.7	6060 ± 560	3.92 ± .45
Pb	π^-	39.0 ± 0.7	4170 ± 450	3.01 ± .38
		2.10 GeV/A α		
C	π^+	47.9 ± 1.1	555. ± 67.	.83 ± .12
C	π^-	44.6 ± 1.9	750 ± 130	.87 ± .20
Al	π^+	49.5 ± 1.2	990 ± 120	1.63 ± .23
Al	π^-	46.8 ± 1.7	1320 ± 180	1.82 ± .33
Cu	π^+	52.5 ± 0.8	1850 ± 140	3.69 ± .34
Cu	π^-	49.1 ± 0.8	2330 ± 190	3.75 ± .37
Sn	π^+	53.2 ± 1.2	2660 ± 270	5.53 ± .68
Sn	π^-	49.7 ± 0.9	3670 ± 330	6.15 ± .67
Pb	π^+	54.2 ± 1.1	4370 ± 400	9.6 ±1.1
Pb	π^-	50.5 ± 0.9	5590 ± 470	9.9 ±1.0
		0.40 GeV/A C		
C	π^+	30.0 ± 0.6	255. ± 23.	.0628± .0094
C	π^-	28.3 ± 1.1	312. ± 38.	.059 ± .013
Cu	π^+	30.3 ± 0.7	1150. ± 94.	.296 ± .039
Cu	π^-	27.3 ± 0.6	1560 ± 120	.248 ± .032
Pb	π^+	32.1 ± 1.0	2240 ± 210	.74 ± .12
Pb	π^-	26.5 ± 0.7	4200 ± 370	.578 ± .091

TABLE XXVII (continued).

Target	Fragment	Slope Parameter (MeV)	Intercept Parameter $\left[\frac{mb-GeV}{sr-(GeV/c)^3}\right]$	Integrated Cross Section (mb/sr)
		1.05 GeV/A C		
C	π^+	33.0 ± 1.2	2620 ± 460	.98 ± .23
C	π^-	35.5 ± 0.4	1990 ± 130	.998 ± .080
Al	π^+	34.7 ± 1.1	4390 ± 660	2.01 ± .40
Al	π^-	35.9 ± 0.4	4250 ± 290	2.23 ± .18
Cu	π^+	37.6 ± 1.0	7710 ± 960	4.84 ± .78
Cu	π^-	41.9 ± 0.6	4170 ± 370	3.91 ± .40
Sn	π^+	37.8 ± 1.2	11500 ± 1700	7.4 ±1.4
Sn	π^-	41.1 ± 0.6	7670 ± 650	6.71 ± .67
Pb	π^+	38.3 ± 1.1	18200 ± 2400	12.3 ±2.1
Pb	π^-	42.2 ± 0.6	11100 ± 910	10.7 ±1.0
		2.10 GeV/A C		
C	π^+	58.0 ± 1.7	704. ± 93.	1.71 ± .28
C	π^-	47.5 ± 0.6	1450. ± 91.	2.10 ± .16
Al	π^+	49.8 ± 0.9	3000 ± 230	5.06 ± .49
Al	π^-	49.8 ± 0.8	2760 ± 230	4.66 ± .45
Cu	π^+	52.6 ± 0.7	5990 ± 370	12.00 ± .89
Cu	π^-	50.8 ± 0.5	6450 ± 310	11.60 ± .66
Sn	π^+	52.4 ± 0.9	9560 ± 700	19.0 ±1.7
Sn	π^-	53.3 ± 0.9	8880 ± 730	18.6 ±1.8
Pb	π^+	53.2 ± 0.9	16300 ± 1100	33.9 ±3.0
Pb	π^-	53.7 ± 0.5	15000 ± 890	32.1 ±1.7
		1.05 GeV/A Ar		
C	π^+	43.4 ± 1.7	1690 ± 290	1.80 ± .39
C	π^-	39.1 ± 1.5	2640 ± 460	1.92 ± .44
Al	π^+	36.6 ± 1.5	6900 ± 1300	3.93 ± .96
Al	π^-	37.1 ± 1.3	6900 ± 1200	4.12 ± .89
Cu	π^+	40.5 ± 0.9	11600 ± 1300	9.6 ±1.3
Cu	π^-	39.2 ± 0.9	13400 ± 1500	9.9 ±1.4
Sn	π^+	39.4 ± 1.1	20500 ± 2600	15.4 ±2.5
Sn	π^-	40.7 ± 1.1	19800 ± 2500	16.7 ±2.7
Pb	π^+	43.8 ± 0.9	25200 ± 2300	27.2 ±3.2
Pb	π^-	42.8 ± 0.8	29000 ± 2700	28.9 ±3.3

TABLE XXVII (continued).

Target	Fragment	Slope Parameter (MeV)	Intercept Parameter $\left[\frac{\text{mb-GeV}}{\text{sr-(GeV/c)}^3}\right]$	Integrated Cross Section (mb/sr)
		1.83 GeV/A Ar		
C	π^+	47.2 ± 1.1	3120 ± 330	4.41 ± .58
C	π^-	43.5 ± 0.9	4500 ± 460	4.82 ± .61
Al	π^+	48.2 ± 0.9	6170 ± 590	9.4 ± 1.1
Al	π^-	52.2 ± 0.9	5080 ± 400	9.95 ± .95
Cu	π^+	51.0 ± 0.7	12600 ± 790	22.9 ± 1.8
Cu	π^-	51.0 ± 0.7	13300 ± 820	24.2 ± 1.8
Sn	π^+	54.7 ± 0.8	15100 ± 1100	34.2 ± 2.8
Sn	π^-	49.7 ± 0.7	24300 ± 1600	40.7 ± 3.3
Pb	π^+	54.4 ± 0.7	30900 ± 1900	68.8 ± 5.0
Pb	π^-	53.3 ± 0.7	33900 ± 2100	70.9 ± 5.2
		0.40 GeV/A Ne		
Cu	π^+	32.8 ± 2.4	1080 ± 210	.38 ± .14
Sn	π^+	31.9 ± 2.3	1590 ± 320	.51 ± .19
Pb	π^+	34.6 ± 2.3	2320 ± 400	1.05 ± .34

TABLE XXVIII. π^-/π^+ ratios. $\left(\frac{d\sigma}{d\Omega} = \int_{100}^{800} \frac{d^2\sigma}{d\Omega dp} dT\right)$

	.800 GeV/A	1.05 GeV/A	2.1 GeV/A	4.89 GeV/A
p+A				
Ag	.30 ± .12			
C	.31 ± .13	.39 ± .10	.52 ± .12	.78 ± .12
Al		.32 ± .18	.65 ± .12	
Cu	.25 ± .08	.44 ± .07	.56 ± .08	.93 ± .09
Sn		.38 ± .14	.58 ± .10	
Pb	.29 ± .10	.47 ± .08	.65 ± .09	.94 ± .09
α+A				
C		.89 ± .29	1.06 ± .29	
Al		.89 ± .22	1.12 ± .26	
Cu		.87 ± .14	1.02 ± .14	
Sn		.94 ± .18	1.11 ± .18	
Pb		.77 ± .13	1.02 ± .16	
	.400 GeV/A	1.05 GeV/A	1.83 GeV/A	2.1 GeV/A
C+A				
C	.94 ± .25	1.02 ± .25		1.23 ± .22
Al		1.11 ± .24		.92 ± .13
Cu	.84 ± .18	.81 ± .15		.97 ± .09
Sn		.91 ± .20		.98 ± .13
Pb	.78 ± .18	.87 ± .17		.95 ± .10
Ar+A				
C		1.07 ± .34	1.09 ± .20	
Al		1.05 ± .34	1.08 ± .16	
Cu		1.02 ± .20	1.06 ± .11	
Sn		1.08 ± .25	1.19 ± .14	
Pb		1.06 ± .17	1.03 ± .11	

TABLE XXIX. Isobar model yield factors.

	C	Al	Cu	Sn	Pb
p					
π^+	7.903	16.00	33.83	57.04	92.08
π^0	4.315	9.111	20.46	37.62	64.78
π^-	0.7197	1.556	3.607	6.898	12.20
α					
π^+	12.80	25.21	51.98	85.95	136.8
π^0	12.81	26.01	56.01	98.99	165.6
π^-	12.82	26.81	60.13	112.0	194.4
C					
π^+	31.45	60.45	121.5	198.1	311.1
π^0	31.47	62.38	131.2	228.1	376.6
π^-	31.50	64.31	140.8	258.2	442.1
Ar					
π^+	80.21	150.1	293.2	468.5	723.5
π^0	87.57	168.7	344.4	585.9	949.5
π^-	94.94	188.7	401.6	721.9	1215.

TABLE XXX. Upper bounds at the ninety percent confidence level of the K^+ cross section.

Momentum (MeV/c)	$\frac{d^2\sigma}{d\Omega dp}$ $\left(\frac{\text{mb}}{\text{sr-GeV/c}}\right)$
4.89 GeV p + Cu	
233	0.15
248	0.11
268	0.11
279	0.11
298	0.09
319	0.10
2.1 GeV/A α + C	
188	5.9
196	2.4
207	1.7
365	0.11
389	0.10
419	0.12
2.1 GeV/A α + Cu	
188	7.8
195	3.1
207	2.2
365	0.11
389	0.10
419	0.12
2.1 GeV/A C + Cu	
275	0.95
293	0.81
315	0.94

TABLE XXXI. π^+ production cross sections from 0.80 GeV protons, for Ag target.

Mom (MeV/c)	Ag $\frac{d^2\sigma}{d\Omega dp}\left[\frac{mb}{sr-GeV/c}\right]$
267	8.16±.78 E0
269	5.88±.67 E0
276	3.78±.62 E0
285	3.60±.52 E0
288	3.55±.47 E0
297	2.57±.50 E0
308	2.25±.43 E0
311	2.12±.37 E0
323	2.14±.48 E0
433	1.04±.61 −1
440	1.27±.72 −1
452	2.00±.97 −1
472	7.0 ±5.8 −2
474	1.04±.40 −1

TABLE XXXII. π^- production cross sections from 0.80 GeV protons, for CD_2 and Ag targets.

Mom (MeV/c)	CD_2 $\frac{d^2\sigma}{d\Omega dp}\left[\frac{mb}{sr-GeV/c}\right]$	Ag
190		8.00±.75 E0
191	9.9 ±1.2 −1	
200		6.61±.65 E0
202	1.10±.14 E0	
212		5.82±.60 E0
214	9.1 ±1.3 −1	
284	7.9 ±1.6 −2	
286		6.44±.93 −1
298	6.9 ±1.3 −2	
301		4.06±.70 −1
314	3.3 ±1.3 −2	
316		2.74±.64 −1

TABLE XXXIII. π^- production cross sections from 4.89 GeV protons, for CH_2 and CD_2 targets.

Mom (MeV/c)	CH_2 $\frac{d^2\sigma}{d\Omega dp}\left(\frac{mb}{sr-GeV/c}\right)$	CD_2
188	6.48±.71 E0	7.91±.81 E0
200	7.90±.82 E0	9.03±.89 E0
214	8.09±.90 E0	9.10±.98 E0
235		4.93±.49 E0
238	4.25±.44 E0	
250	3.68±.41 E0	4.58±.47 E0
267	3.11±.41 E0	4.25±.48 E0
282		2.70±.25 E0
283	2.10±.24 E0	
283	1.92±.19 E0	2.64±.28 E0
300	1.65±.23 E0	
300	1.69±.18 E0	1.97±.25 E0
300		2.22±.22 E0
319		1.66±.17 E0
320	1.52±.21 E0	
320	1.36±.16 E0	1.62±.22 E0
377	5.86±.59 −1	
378		7.10±.70 −1
400	5.11±.53 −1	
401		5.34±.56 −1
425	3.66±.45 −1	
428		3.47±.45 −1

TABLE XXXIV. Subtracted π^- production cross sections from 0.80 GeV protons for CD_2 target.

Mom (MeV/c)	"d" $\frac{d^2\sigma}{d\Omega dp}\left(\frac{mb}{sr-GeV/c}\right)$
191	7.0±8.5 −2
202	9.5±9.6 −2
214	−3.5±9.9 −2
284	−0.1±1.1 −2
298	−5.5±9.2 −3
314	−5.0±9.2 −3

TABLE XXXV. Subtracted π^- production cross sections from 4.89 GeV protons for CH_2 and CD_2 targets.

Mom (MeV/c)	"p" $\frac{d^2\sigma}{d\Omega dp}\left(\frac{mb}{sr-GeV/c}\right)$	"d"
188	−2.0±5.0 −1	5.2 ±5.4 −1
200	3.7±5.5 −1	9.3 ±5.8 −1
214	3.0±6.0 −1	8.1 ±6.2 −1
235		6.4 ±3.1 −1
236	3.0±2.9 −1	
250	1.3±2.8 −1	5.8 ±3.0 −1
267	3.0±2.7 −1	8.3 ±3.0 −1
283	1.1±1.0 −1	4.4 ±1.2 −1
300	1.8±1.0 −1	3.8 ±1.0 −1
320	9.5±8.7 −2	1.95±.90 −1
377	−1.5±4.3 −2	
378		4.7 ±4.7 −2
400	2.3±3.8 −2	
401		3.4 ±3.8 −2
425	0.2±3.2 −2	
426		−0.8 ±3.2 −2

LIST OF FIGURES

FIG. 1. Data from Baldin, *et al.*[4(a)], for the reaction 8.4 GeV/c $p+A\rightarrow\pi^-(180°)$. The targets are (a) C, (b) Al, (c) Cu, and (d) Pb. (e) Dependence of n on T/T_{max}, where n is the exponent from a fit to the cross section R of the form $R=R_1A^n$. The figures are reprinted with the permission of the American Institute of Physics.

FIG. 2. Data from Papp, *et al.*[3] for the reaction $B+C\rightarrow\pi^-(2.5°)+X$, for beams of (a) p, (b) d, and (c) α. The invariant cross section is plotted against the scaling parameter x'. The solid line is the prediction of the SB[2] model, normalized to the data.

FIG. 3. (a) Generalized Feynman diagram for hard scattering models. The amplitude ψ_A (ψ_B) refers to finding an off-shell nucleon a (b) within A (B); $T_{ab\pi x}$ is the off-shell scattering matrix for the reaction $a+b\rightarrow\pi+x$; and Ω represents distortions due to final state interactions. X are the undetected particles after final state interactions have occurred.

(b) Simplified Feynman diagram for hard scattering models. The symbols are the same as in the preceding figure, except that now $X=\alpha+\beta+x$, where α and β are the remnants of A and B.

FIG. 4. Models of the pseudo-probability distribution used by various hard scattering models. (a) The completely coherent model of Schmidt and Blankenbecler[2]. (b) The frozen cluster model of Landau and Gyulassy[12]. (c) The cluster with internal motion model of Landau and Gyulassy[12].

FIG. 5. Diagrams for quasi-two-body scaling (QTBS). (a) For the $p+A\rightarrow p+X$ case, showing nomenclature. (b) Quasi-two-body kinematics, showing definition

of k_{min}. (c) Extension of QTBS to $p+A\to\pi+X$. (d) Extension of QTBS to $B+A\to\pi+X$.

FIG. 6. (a) Fireball geometry. (b) Firestreak geometry.

FIG. 7. (a) and (b) are the data from Ref. 23 and show invariant cross section versus rapidity at fixed transverse momentum for negative pions for 800 MeV/A Ne on (a) Pb and (b) NaF. Error bars (not shown) range from 20% for the large cross sections to 100% for the small ones. The solid lines represent the predictions of the firestreak model. (c) and (d) are the data are from Ref. 24 and show laboratory cross section versus kinetic energy for positive pions for 800 MeV/A Ne on (c) Pb and (d) NaF. The firestreak predictions (lines) have been multiplied by a factor of 1/2.

FIG. 8. Comparisons of the BK model with the data of (a) Ref. 29 and (b) Ref. 3. The full line represents the BK model, the dashed line represents their firestreak simulation.

FIG. 9. A peripheral nucleus-nucleus collision (a) viewed from the laboratory frame; (b) viewed from the projectile frame; (c) showing the definition of the area a_1; (d) showing the definition of the thickness t_1. The figure is from Ref. 30(a), and is reprinted with the permission of Meng Ta-Chung.

FIG. 10. Data from Refs. 3, 4(a), and 4(b), plotted according to the prescription of Meng Ta-Chung. (a) $(d^3\sigma/dp^3)_{lab}$ vs $e^{kin}_{lab}/\varepsilon$, for $p+C\to\pi^-+X$ at $\vartheta_{lab}=2.5°$ and $\varepsilon=1.05$, 1.73, 2.10, 2.66, 3.50, 4.20, and 4.80 GeV (from Ref. 3);

(b) $s_1^{-1}(d^3\sigma/d$, $)_{lab}$ vs $e^{kin}_{lab}/\sqrt{s_1}\varepsilon$, for $(p,d,\alpha)+C\to\pi^-+X$ at $\vartheta_{lab}=2.5°$ and $\varepsilon=1.05$ and 2.10 GeV/nucleon (from Ref. 3);

(c) $s_2^{-1}(d^3\sigma/dp^3)_{proj}$ vs $e^{kin}_{proj}/\sqrt{s_2}\varepsilon$, for $p+(d,C,Al,Cu,Pb)\to\pi^-+X$ at $\vartheta_{lab}=180°$ and incident proton momentum $P_p=6.4$ and 6.0 Gev/c (from Ref. 4(a));

(d) $s_2^{-1}(d^3\sigma/dp^3)_{proj}$ vs $e^{kin}_{proj}/\sqrt{s_2}\varepsilon$, for $d+(d,{}^6Li,{}^7Li,C,Al,Cu,{}^{144}Sm,Pb)\to\pi^-+X$ at

ϑ_{lab} =180° and incident deuteron momentum P_d=8.4 Gev/c (from Ref. 4(b)). The figures are from Ref. 30(a), and are reprinted with the permission of Meng Ta-Chung.

FIG. 11. (a) Plan view of spectrometer. (b) Elevation view of spectrometer.

FIG. 12. Results of scan of target across beam.

FIG. 13. Plot of pulse height versus time-of-flight, for 2.1 GeV/A C + $\frac{1}{8}$" Cu, long gate configuration at 300 MeV/c.

FIG. 14. Diagram of electronics used to produce a trigger signal. The delays incurred in processing by each component are shown, as are the threshold settings of the discriminators ("Disc"). TDC stands for time-to-digital converter, ADC for analog-to-digital converter, and MT for Master Trigger.

FIG. 15. Plot of invariant cross section versus kinetic energy for the reaction 2.1 GeV/A C + Cu → π^- (180°) + X.

FIG. 16. Plot of T_0 versus T_{beam}/A_{beam}, for protons, alphas, carbon, and argon on copper. The dashed line is hand drawn and illustrates the trend of the data.

FIG. 17. The T_0 dependence on beam and target, for beam energy fixed at 1.05 GeV/A.

FIG. 18. Integrated cross section versus beam energy for carbon beams on all targets.

FIG. 19. π^-/π^+ ratios as a function of beam energy, for all beam and target combinations.

FIG. 20. Integrated pion cross section versus the product of the beam and target masses for the 1.05 GeV → π^+ data.

FIG. 21. Comparison of mock-up with data. (a) 1.05 GeV/A alpha beam. (b) 1.05 GeV/A argon beam. (c) 2.1 GeV/A alpha beam.

FIG. 22. Integrated cross section plotted against the isobar yield factors, for the 1.05 GeV/A beams. Straight lines have slope of one.

FIG. 23. As above, but broken down by momentum: (a) 1.05 GeV/A, and 200 MeV/c; (b) 1.05 GeV/A, and 500 MeV/c.

FIG. 24. Data from Anderson, *et al.*[47], for the reaction $C + C \rightarrow \pi^-(0°)$ at (a) 1.05 and (b) 2.1 GeV/A.

FIG. 25. Figure 3 from Schroeder, *et al.*[15(b)], showing integrated cross section versus x' for p+Cu$\rightarrow\pi^k(180°)+X$. The lines are fits of the form $(1-x')^N$. The SB model predicts N=373.

FIG. 26. Invariant cross section versus x', with the curves of Landau and Gyulassy superimposed. (a) p+Cu$\rightarrow\pi^-$. (b) α+Cu$\rightarrow\pi^-$.

FIG. 27. Invariant cross section versus x_H for (a) p+Cu$\rightarrow\pi^-$; (b) Cu+C$\rightarrow\pi^-$.

FIG. 28. Plot of $|p-q|\,\frac{d^3\sigma}{dp^3}$ versus k_{min}, for p+Cu$\rightarrow\pi^-$.

FIG. 29. Plot of the firestreak model[21] and the rows-on-rows model of Bohrmann and Knoll[26] compared with the data.

FIG. 30. Graphs of $s_2^{-1}(d^3\sigma/dp^3)_{proj}$ versus $e^{kin}_{proj}/\sqrt{s_2}\varepsilon$, for (a) $p+A\rightarrow\pi^-$, (b) Ar$+A\rightarrow\pi^-$, and (c) $p+A\rightarrow\pi^+$. The dashed line illustrates the trend of the 2.1 GeV data.

FIG. 31. Plot of T_0 versus T_{beam} for proton-induced pions. The prediction of Meng Ta-Chung, normalized to the point for 4.89 GeV protons on copper, is superimposed.

FIG. 32. Histogram of the time-of-flight channels for a K^+ run. Statistical error bars are shown. The expected location of the kaon peak is indicated. Superimposed are the results of the corresponding "long gate" (proton and positive pion) run.

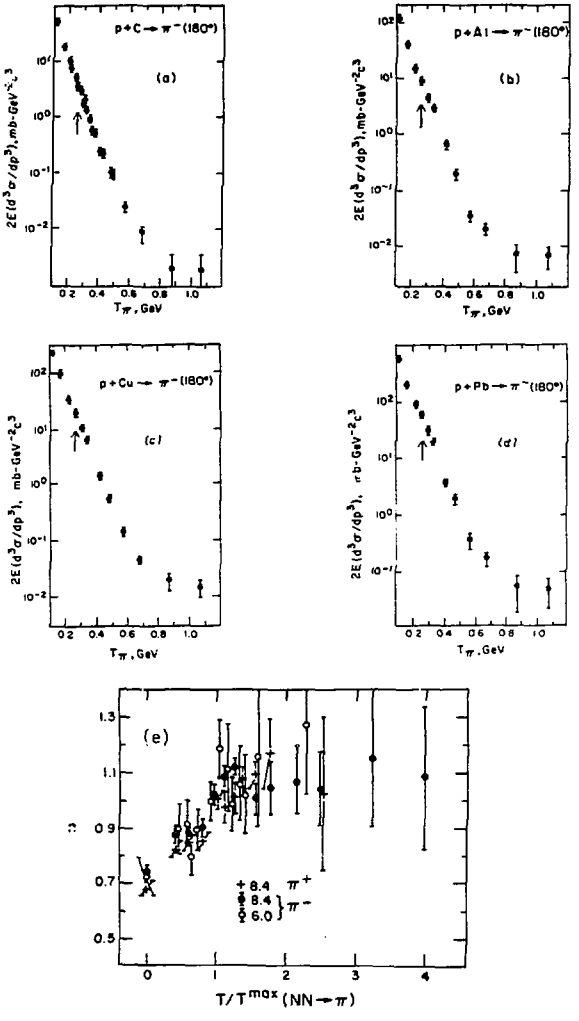

XBL 824-317A

Fig. 1

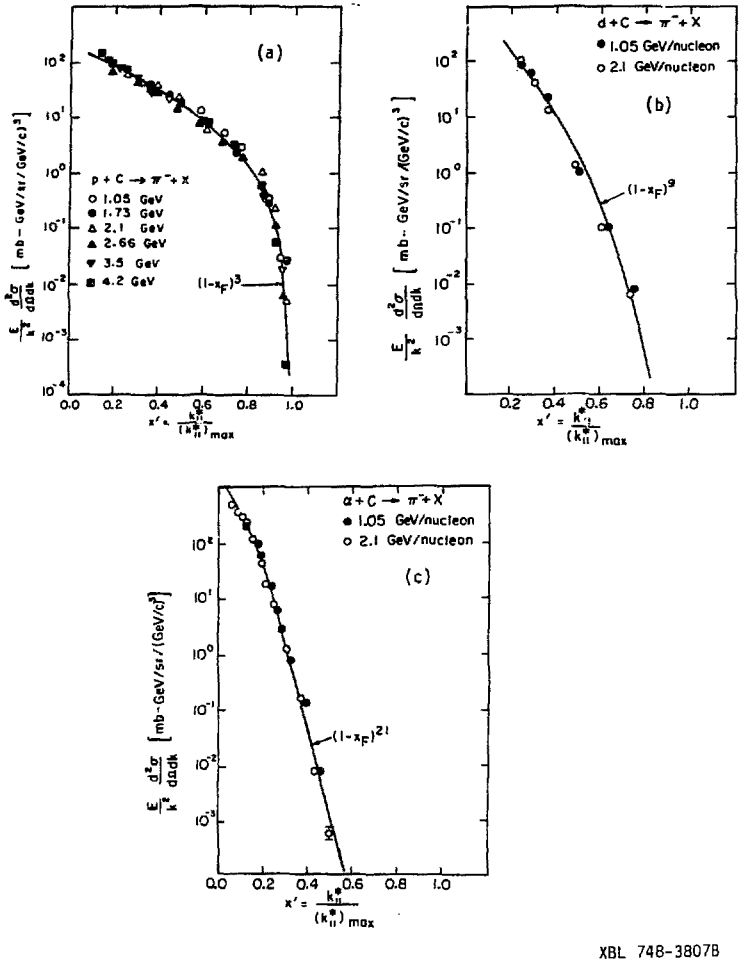

XBL 748-3807B

Fig. 2

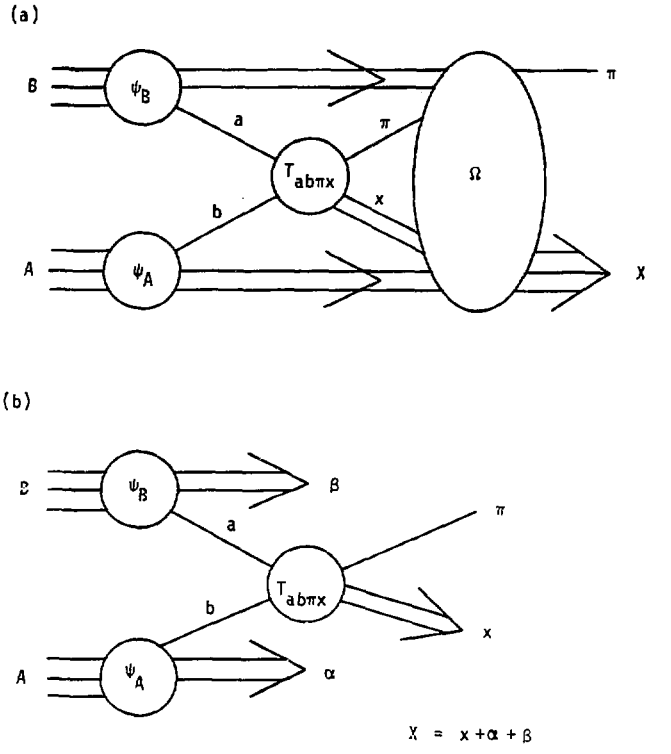

XBL 829-9674

Fig. 3

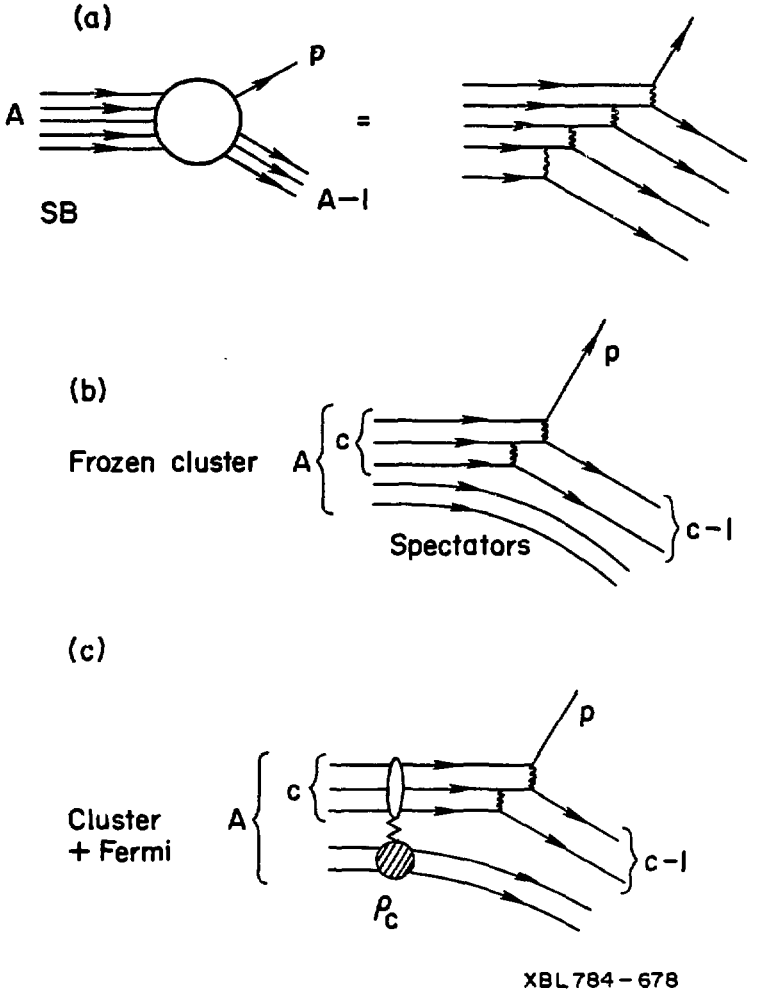
(a)
p
A
=
SB
A−1
(b)
p
Frozen cluster
A
c
c−1
Spectators
(c)
p
Cluster
+ Fermi
A
c
c−1
ρ_c
XBL 784-678

Fig. 4

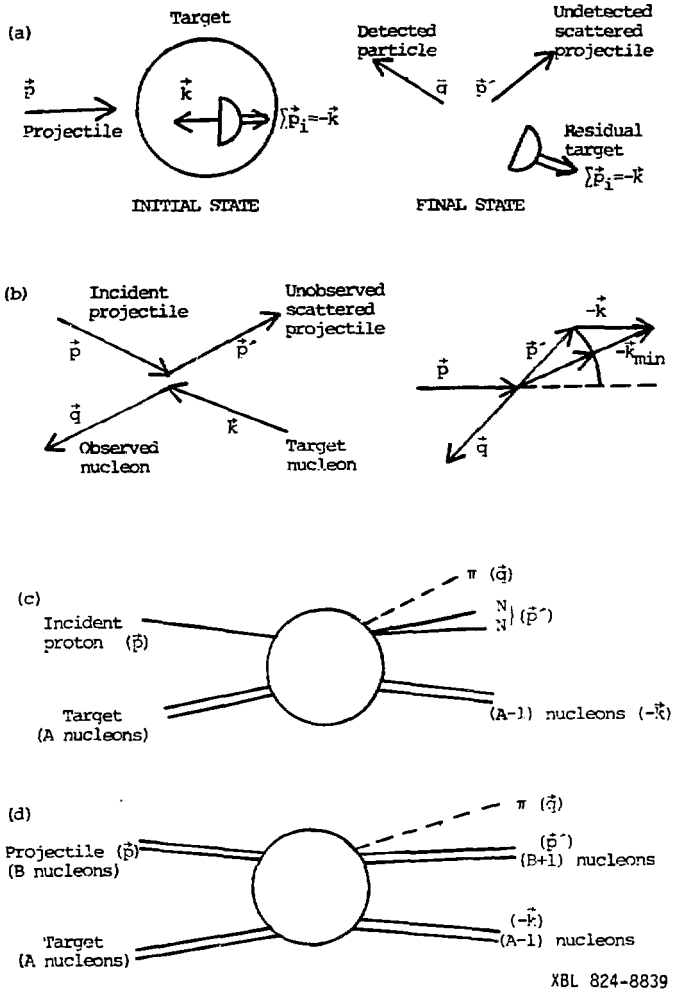
(a)
Target
$\vec{p}$
Projectile
$\vec{k}$
$\sum\vec{p}_i=-\vec{k}$
INITIAL STATE
Detected particle
$\vec{q}$
$\vec{p}'$
Undetected scattered projectile
Residual target
$\sum\vec{p}_i=-\vec{k}$
FINAL STATE
(b)
Incident projectile
$\vec{p}$
Unobserved scattered projectile
$\vec{p}'$
$\vec{q}$
Observed nucleon
$\vec{k}$
Target nucleon
$-\vec{k}$
$\vec{p}'$
$-\vec{k}_{min}$
$\vec{p}$
$\vec{q}$
(c)
Incident proton ($\vec{p}$)
Target (A nucleons)
π ($\vec{q}$)
N N ($\vec{p}'$)
(A-1) nucleons ($-\vec{k}$)
(d)
Projectile ($\vec{p}$) (B nucleons)
Target (A nucleons)
π ($\vec{q}$)
($\vec{p}'$) (B+1) nucleons
($-\vec{k}$) (A-1) nucleons
XBL 824-8839

Fig. 5

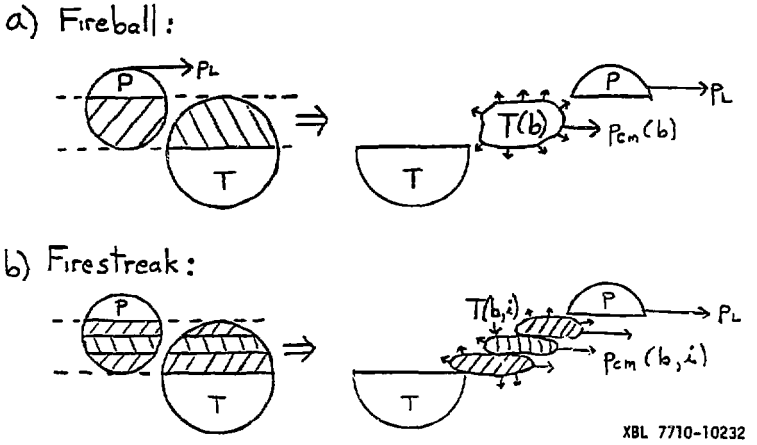
a) Fireball:
P
P_L
T
T
T(b)
$P_{cm}(b)$
P
P_L
b) Firestreak:
P
T
T
T(b,i)
P
P_L
$P_{cm}(b,i)$
XBL 7710-10232

Fig. 6

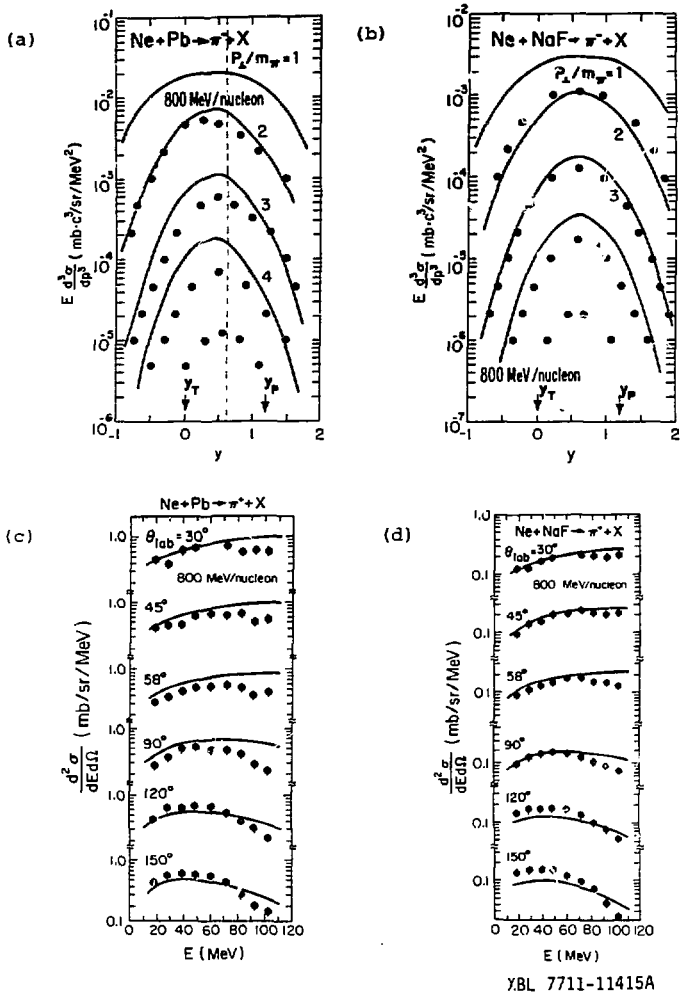
(a)
Ne+Pb→π⁻+X
P⊥/mπ=1
800 MeV/nucleon
2
3
4
yT
yP
y
(b)
Ne+NaF→π⁻+X
P⊥/mπ=1
800 MeV/nucleon
(c)
Ne+Pb→π⁺+X
θlab=30°
45°
58°
90°
120°
150°
E (MeV)
(d)
Ne+NaF→π⁺+X
YBL 7711-11415A

Fig. 7

(a)

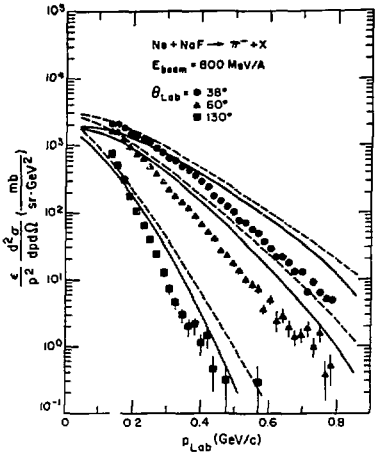

(b)

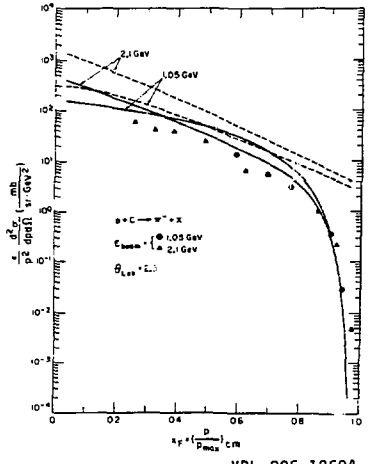

XBL 806-1269A

Fig. 8

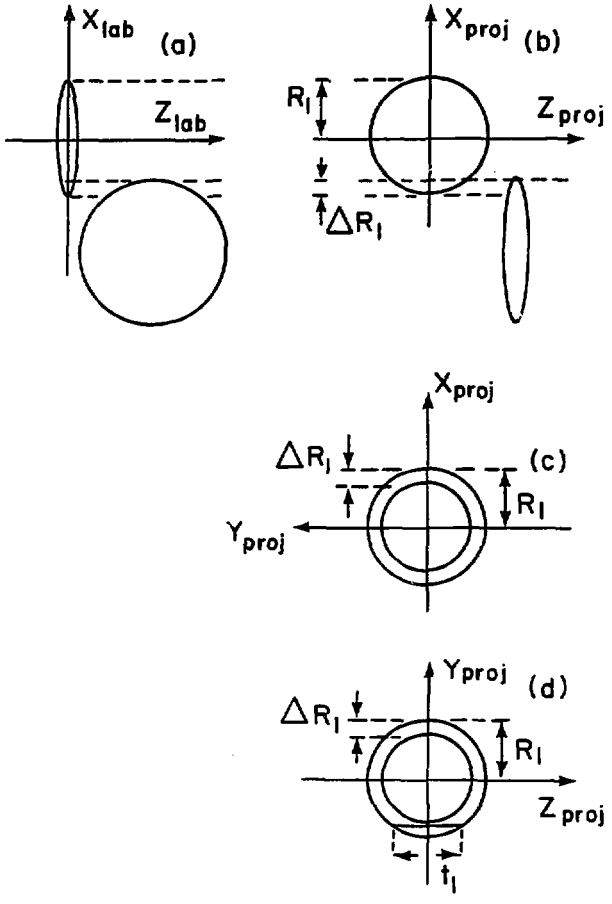

XBL 824-314

Fig. 9

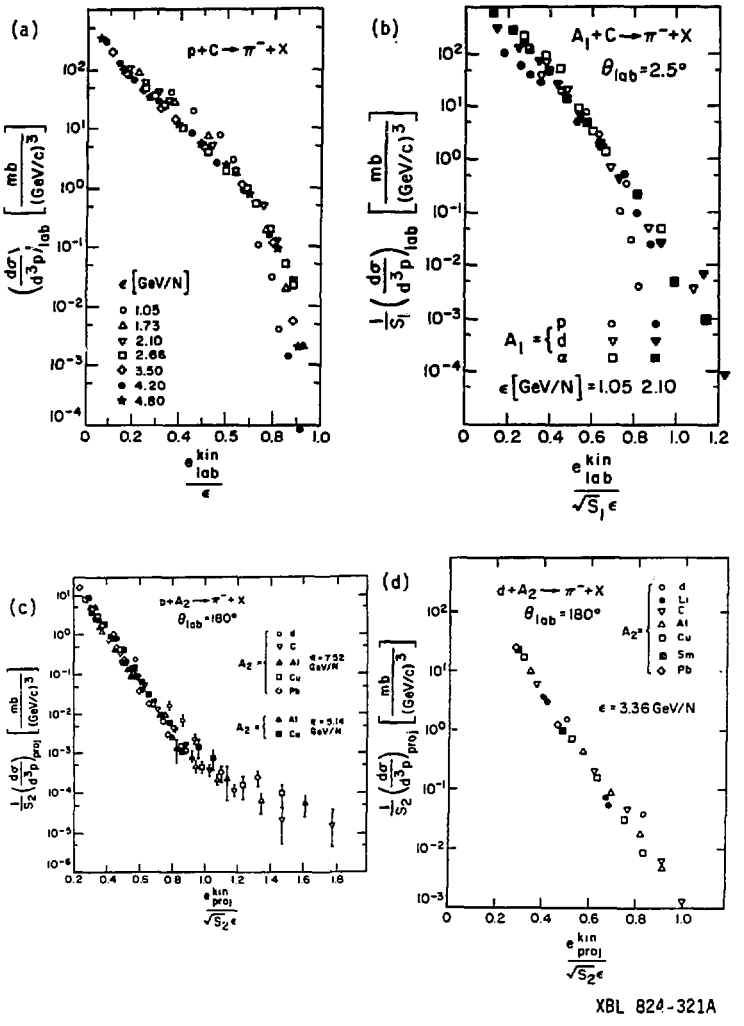

XBL 824-321A

Fig. 10

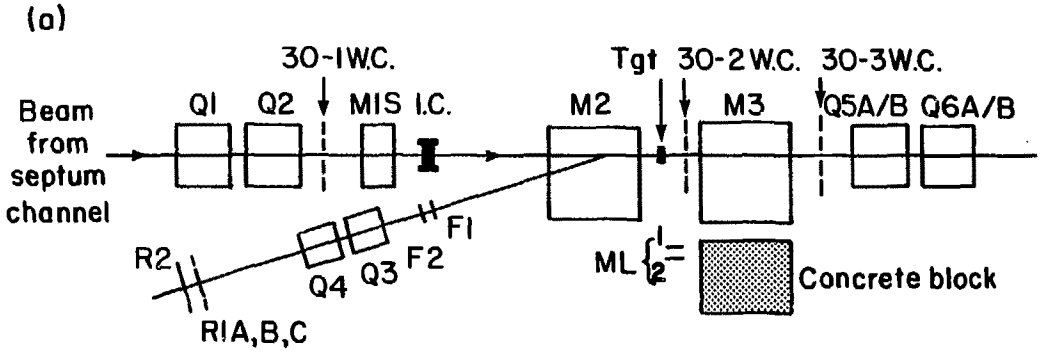

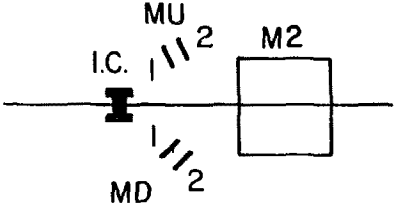

XBL 824-315

Fig. 11

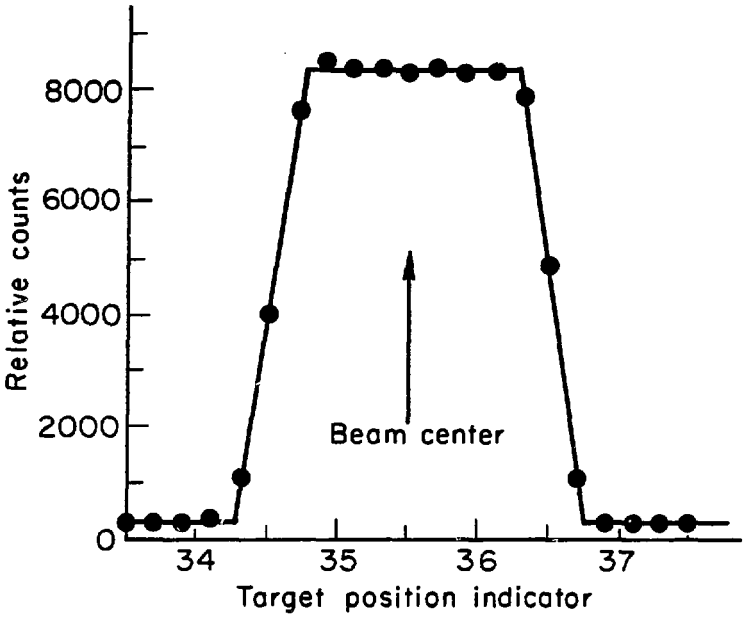

XBL823-3703

Fig. 12

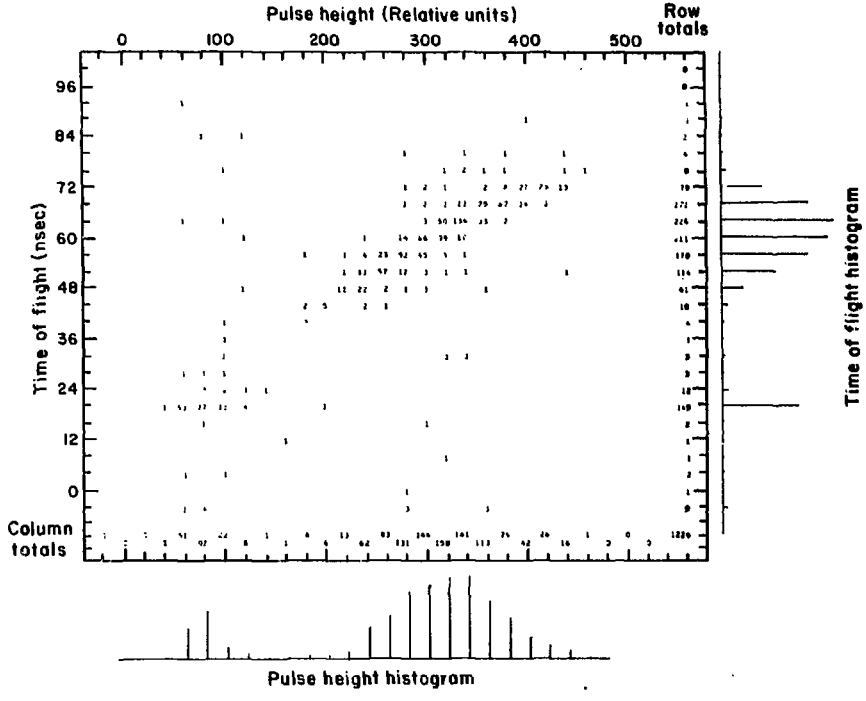

XBL 824-316

Fig. 13

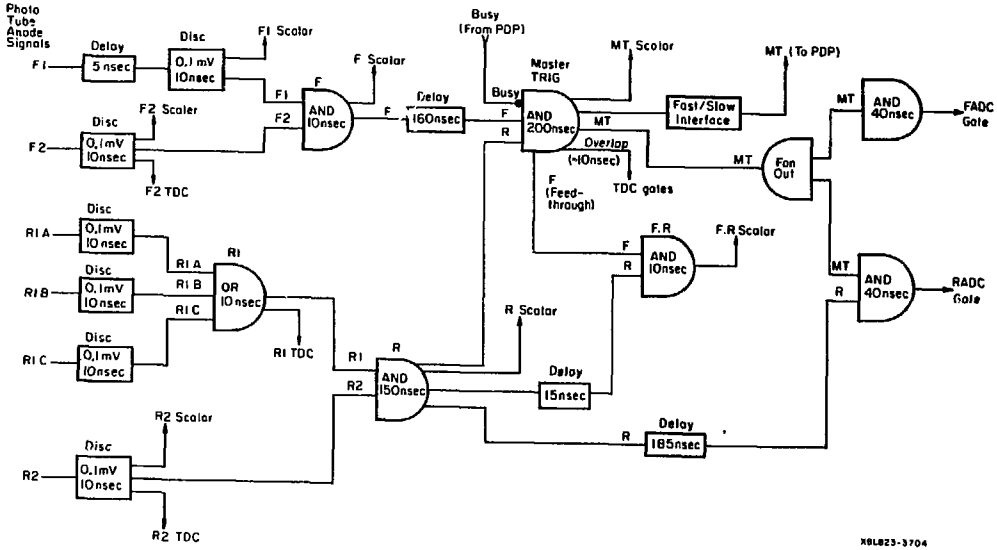
Photo Tube Anode Signals
F1
Delay 5 nsec
Disc 0.1 mV 10nsec
F1 Scalar
F1
F2 Scaler
F2
Disc 0.1mV 10nsec
F2 TDC
F
AND 10nsec
F Scalar
F
Delay 160nsec
Busy (From PDP)
Busy
F
R
AND 200nsec
Master TRIG
MT Scalar
MT
Overlap (~10nsec)
TDC gates
F (Feed-through)
Fast/Slow Interface
MT (To PDP)
MT
Fan Out
MT
AND 40nsec
FADC Gate
MT
R
AND 40nsec
RADC Gate
F.R
AND 10nsec
F.R Scalar
F
R
R Scalar
Delay 15nsec
R
Delay 185nsec
R1 A
Disc 0.1mV 10nsec
R1 B
Disc 0.1mV 10nsec
R1 C
Disc 0.1mV 10nsec
R1
R1 A
R1 B
R1 C
OR 10nsec
R1 TDC
R1
R2
R
AND 150nsec
R2 Scalar
R2
Disc 0.1mV 10nsec
R2 TDC
X8L823-3704

Fig. 14

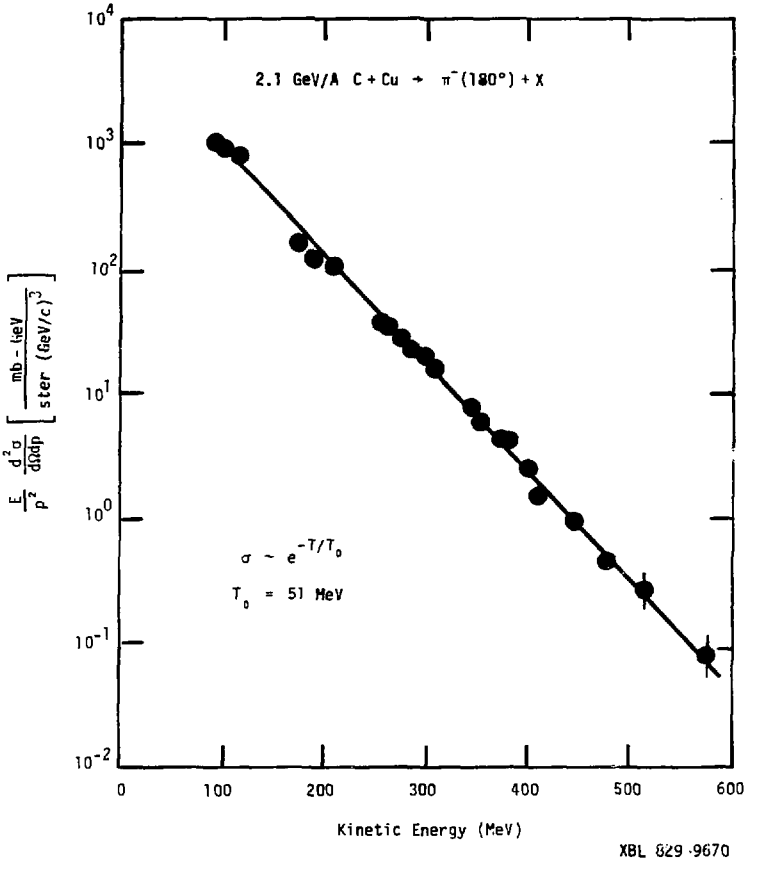
2.1 GeV/A C + Cu → π⁻(180°) + X
σ ~ e^(-T/T₀)
T₀ = 51 MeV
E/p² d²σ/dΩdp [mb - GeV / ster (GeV/c)³]
10⁴
10³
10²
10¹
10⁰
10⁻¹
10⁻²
0
100
200
300
400
500
600
Kinetic Energy (MeV)
XBL 829-9670

Fig. 15

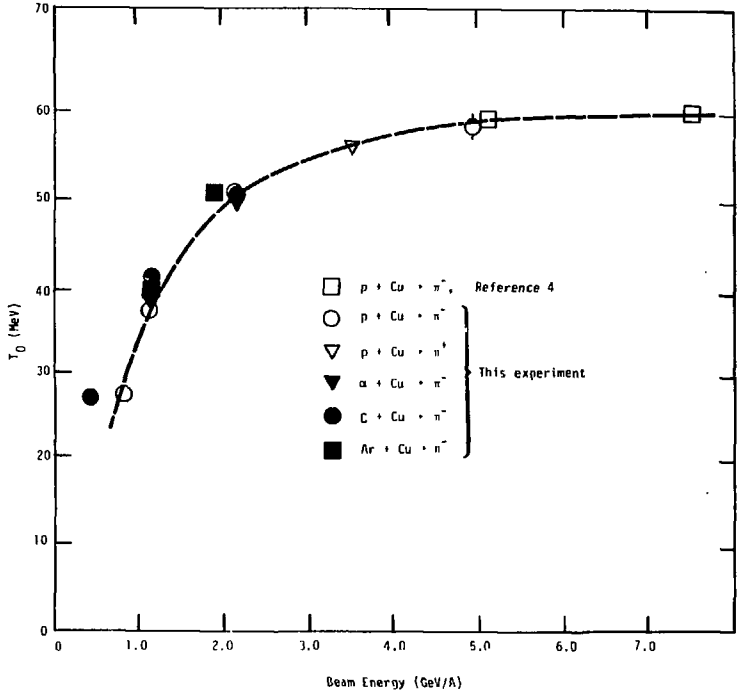

XBL 829-9671

Fig. 16

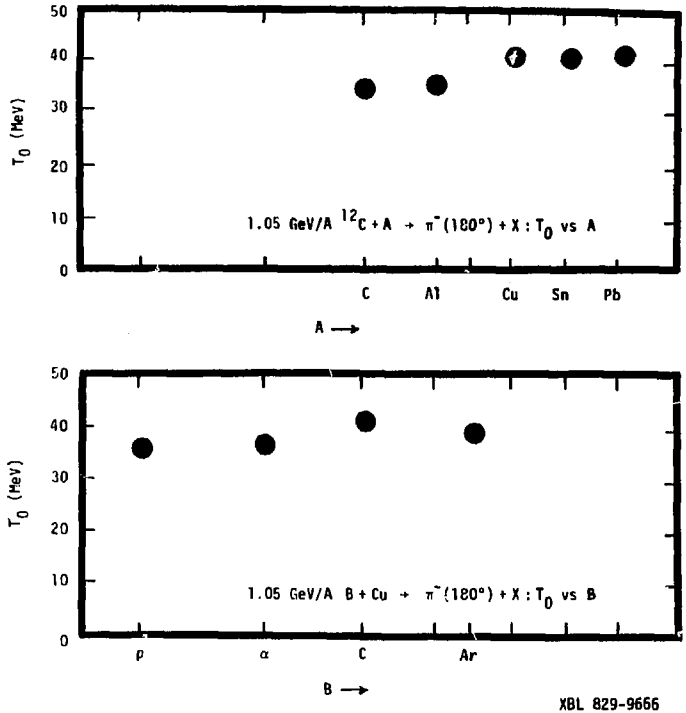

XBL 829-9666

Fig. 17

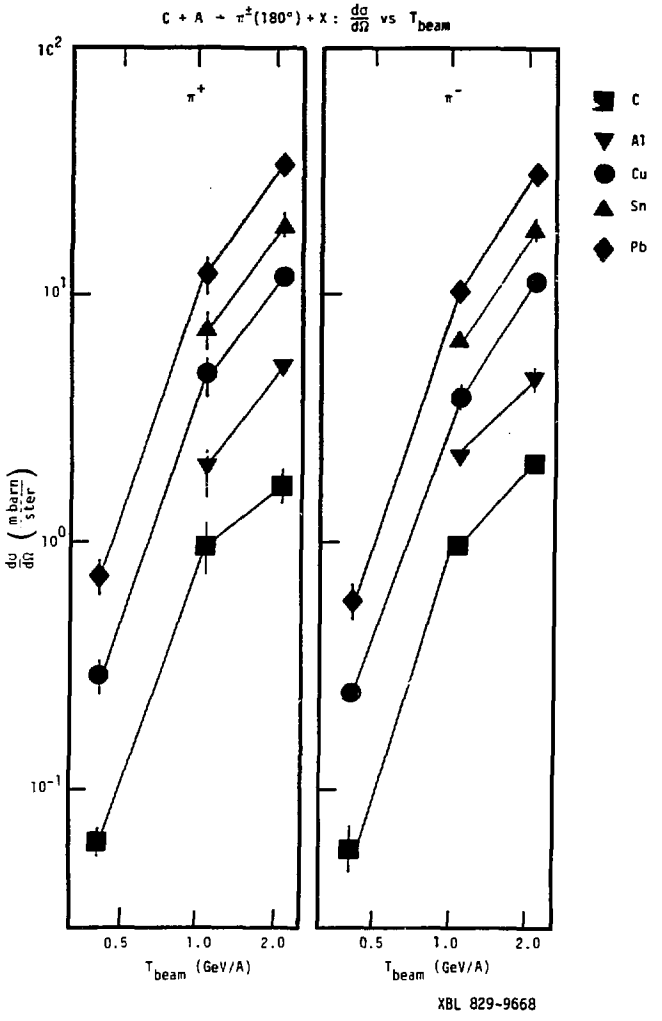
C + A → π±(180°) + X : dσ/dΩ vs T_beam
π+
π−
C
Al
Cu
Sn
Pb
10^2
10^1
10^0
10^-1
dσ/dΩ (mbarn/ster)
0.5
1.0
2.0
T_beam (GeV/A)
XBL 829-9668

Fig. 18

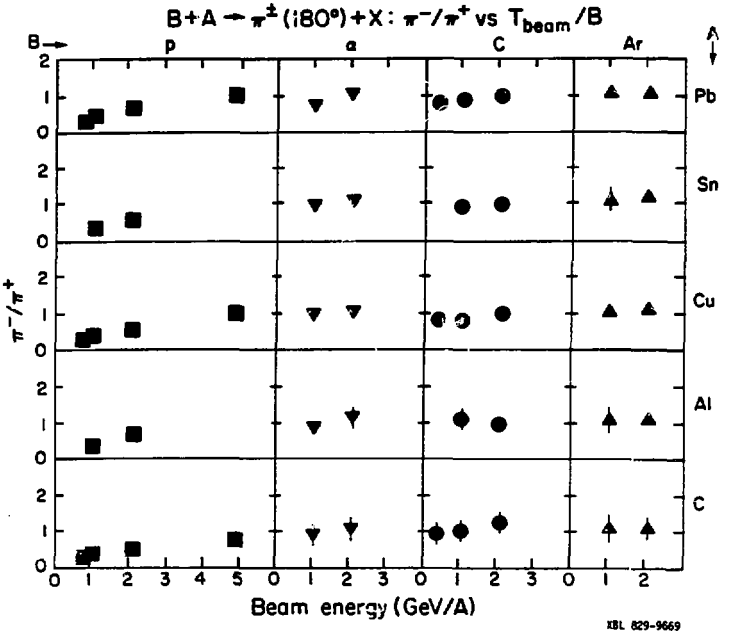
B+A → π±(180°)+X: π⁻/π⁺ vs T_beam/B
B →
p
α
C
Ar
A
Pb
Sn
Cu
Al
C
π⁻/π⁺
Beam energy (GeV/A)
XBL 829-9669

Fig. 19

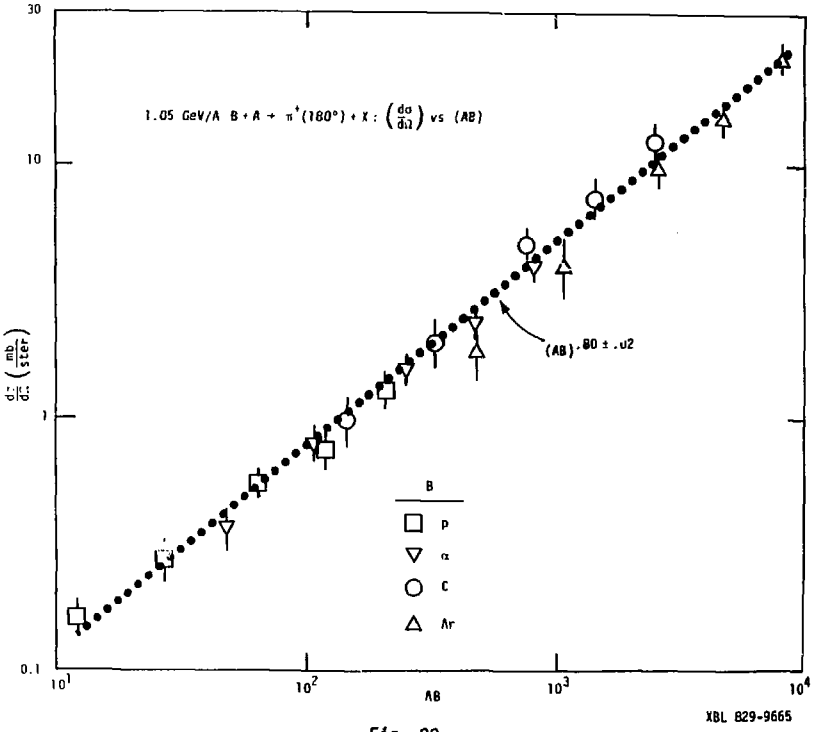
1.05 GeV/A B + A → π+(180°) + X : (dσ/dΩ) vs (AB)
(AB)^.80 ± .02
B
p
α
C
Ar
dσ/dΩ (mb/ster)
AB
30
10
1
0.1
10^1
10^2
10^3
10^4
XBL 829-9665

Fig. 20

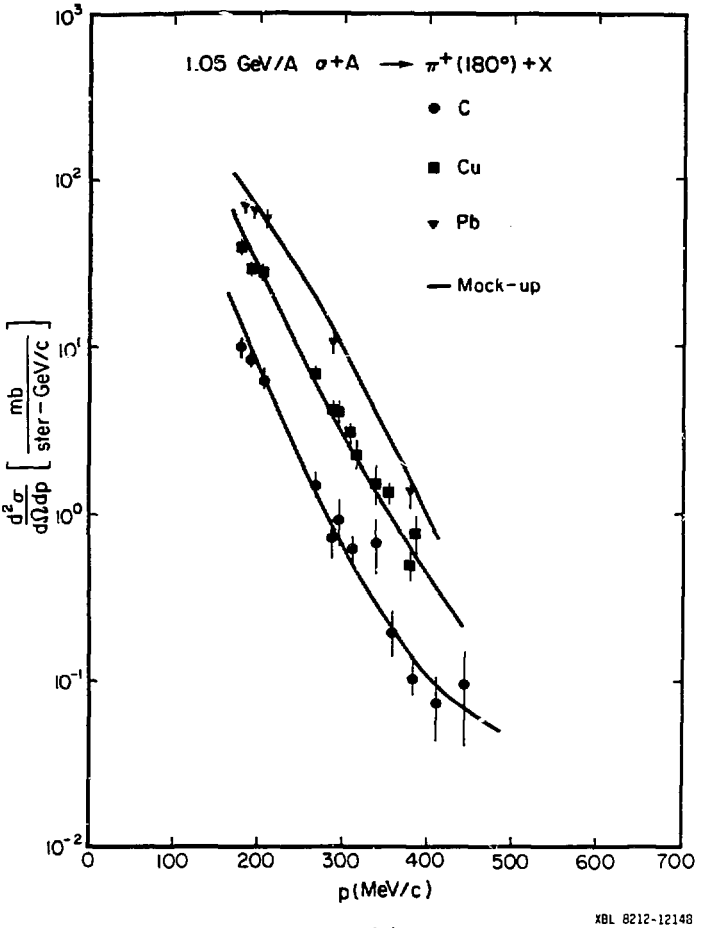

XBL 8212-12148

Fig. 21(a)

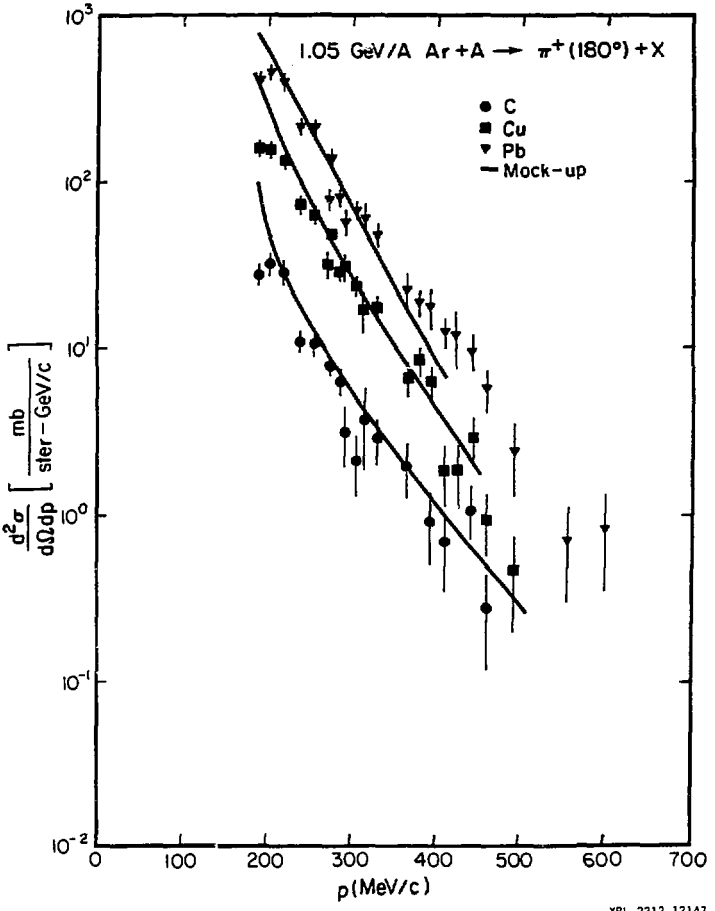
1.05 GeV/A Ar+A → π+(180°)+X
C
Cu
Pb
Mock-up
$\frac{d^2\sigma}{d\Omega dp}\left[\frac{mb}{ster-GeV/c}\right]$
p(MeV/c)
XBL 8212-12147

Fig. 21(b)

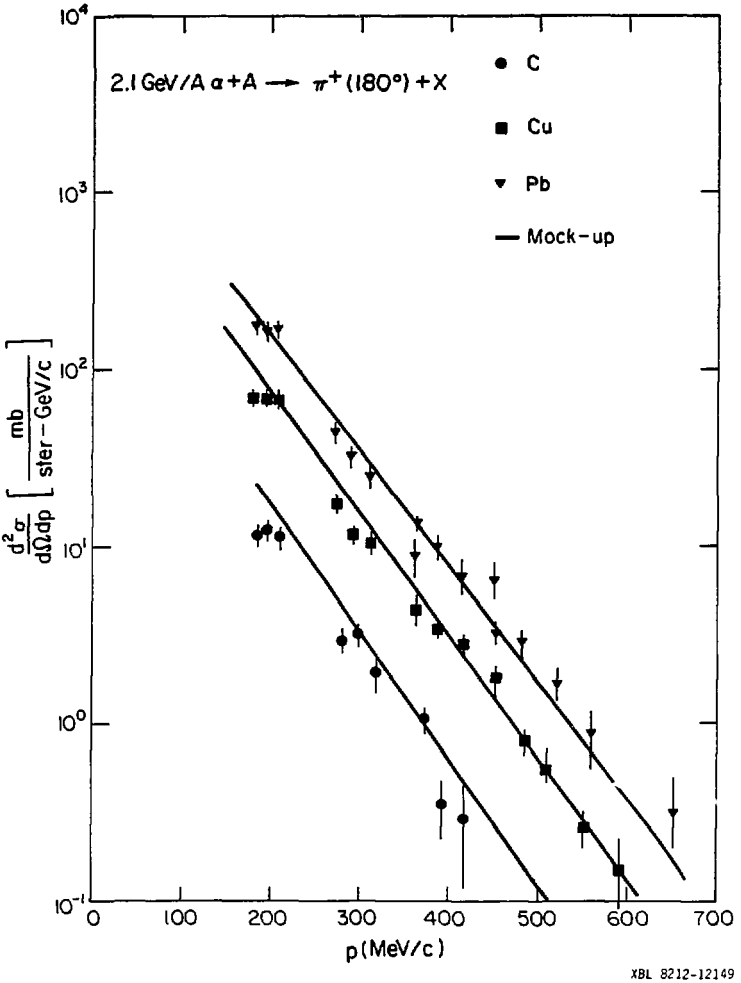

XBL 8212-12149

Fig. 21(c)

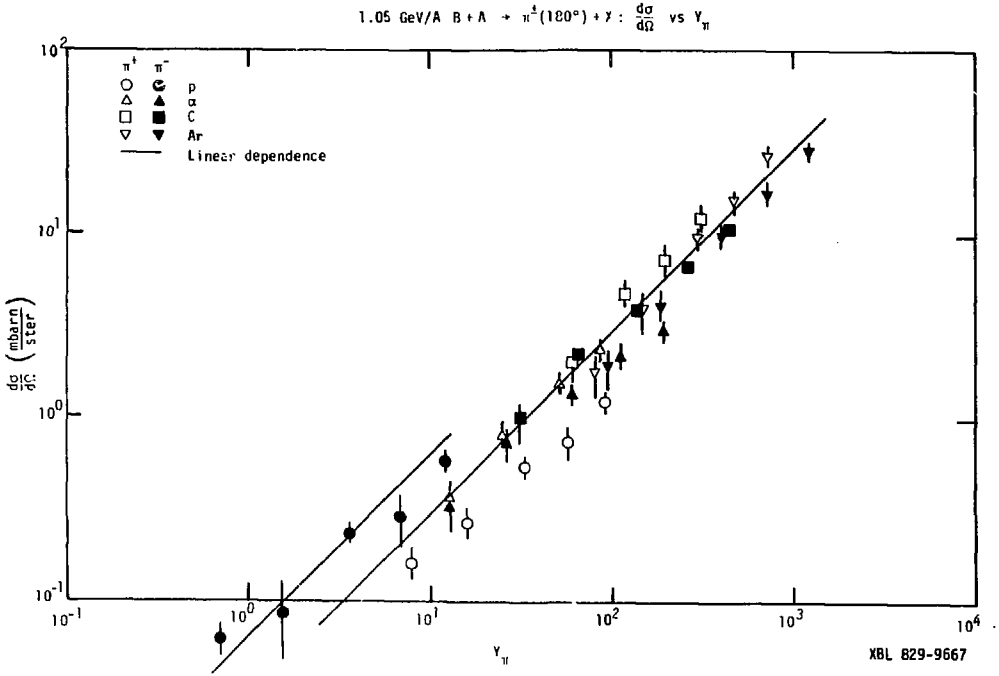
1.05 GeV/A B + A → π±(180°) + X : dσ/dΩ vs Y_π
π+ π−
p
α
C
Ar
Linear dependence
dσ/dΩ (mbarn/ster)
Y_π
XBL 829-9667

Fig. 22

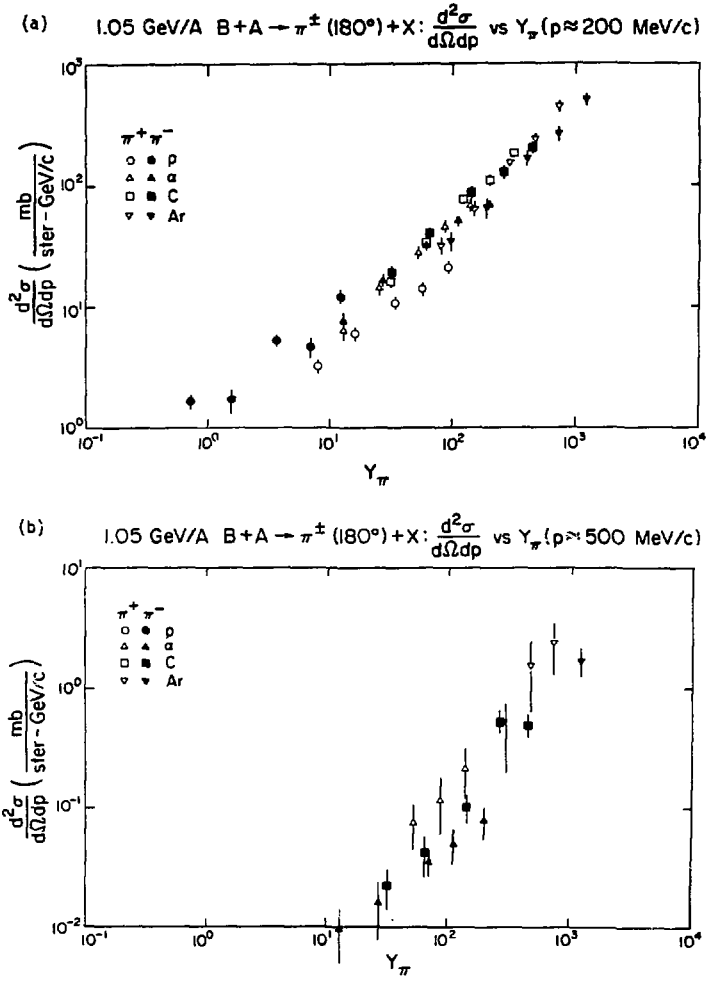

XBL 8212- 12151A

Fig. 23

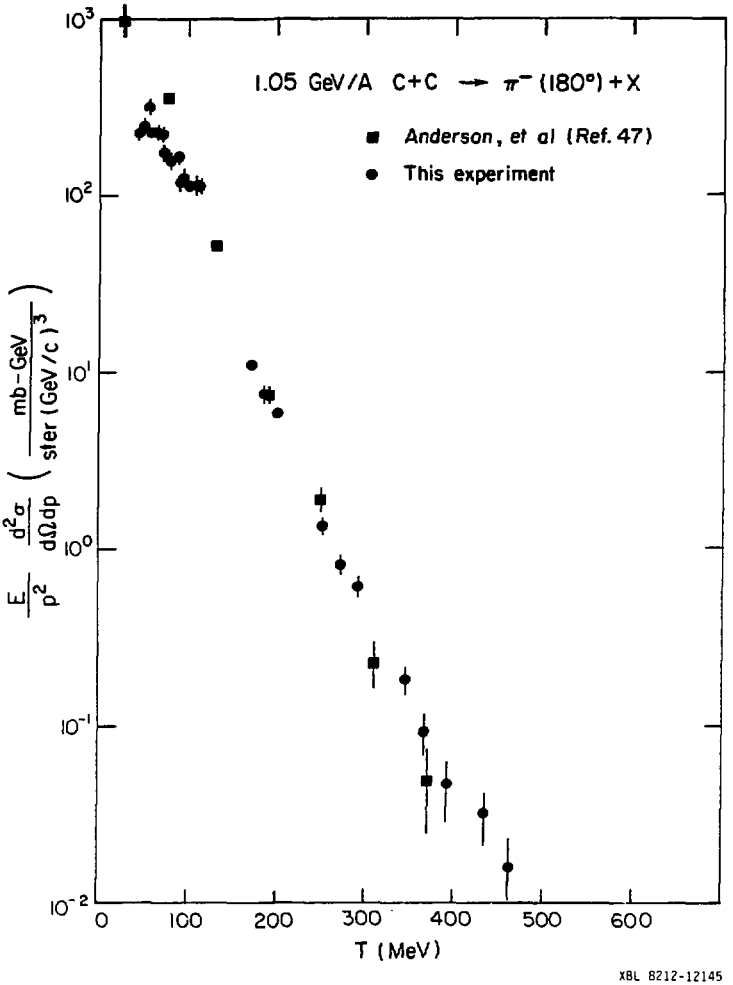
1.05 GeV/A C+C → π⁻ (180°) + X
Anderson, et al (Ref. 47)
This experiment
$\frac{E}{p^2}\frac{d^2\sigma}{d\Omega dp}\left(\frac{mb-GeV}{ster\,(GeV/c)^3}\right)$
10^3
10^2
10^1
10^0
10^{-1}
10^{-2}
0
100
200
300
400
500
600
T (MeV)
XBL 8212-12145

Fig. 24(a)

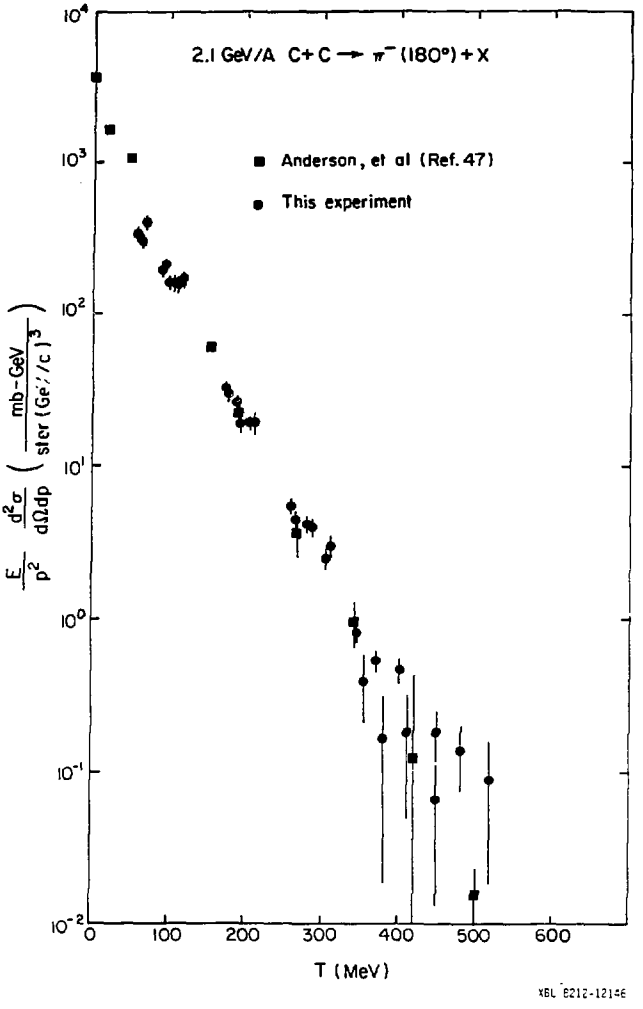
2.1 GeV/A C+C → π⁻ (180°) + X
Anderson, et al (Ref. 47)
This experiment
$\frac{E}{p^2}\frac{d^2\sigma}{d\Omega dp}\left(\frac{mb\text{-}GeV}{ster\,(GeV/c)^3}\right)$
T (MeV)
XBL 8212-12146

Fig. 24(b)

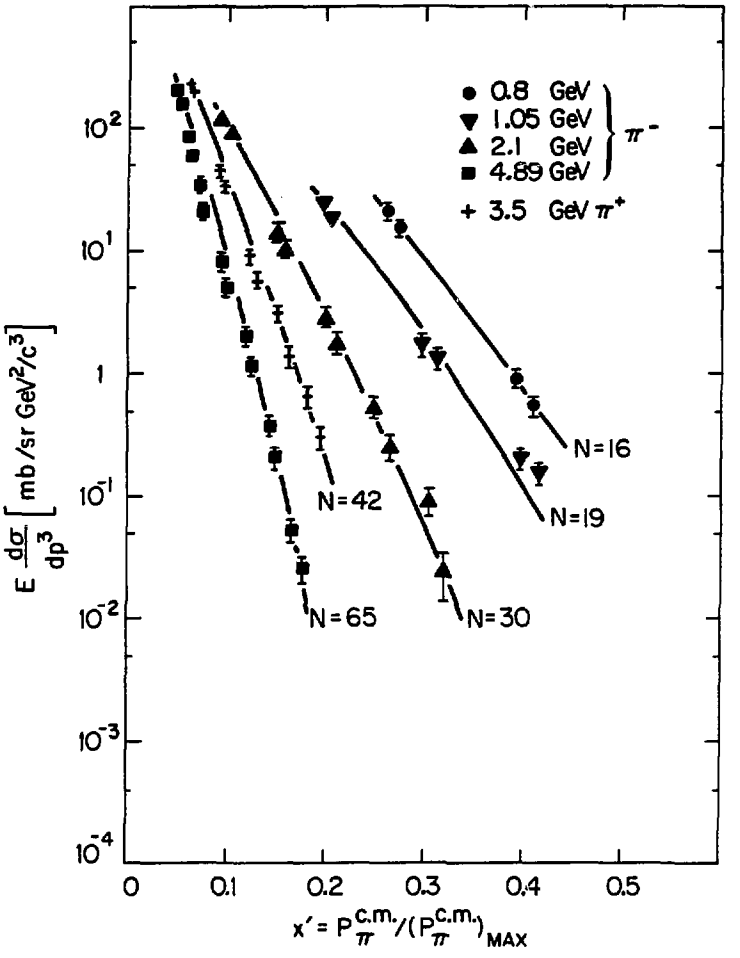

XBL 798 - 2505

Fig. 25

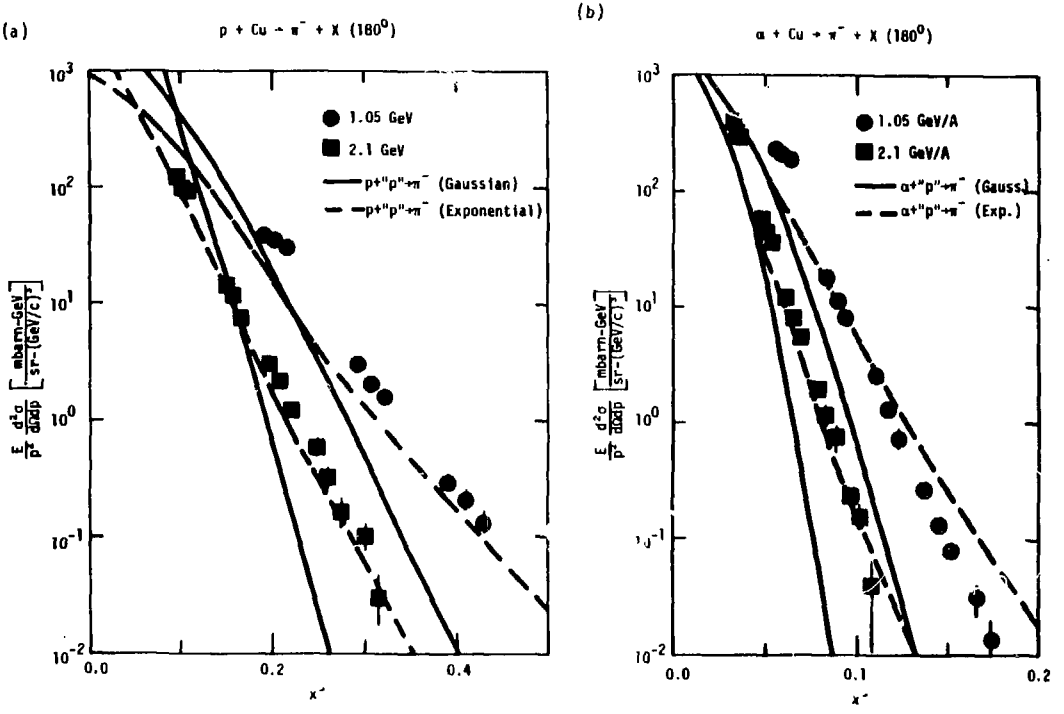

XBL 829-11440

Fig. 26

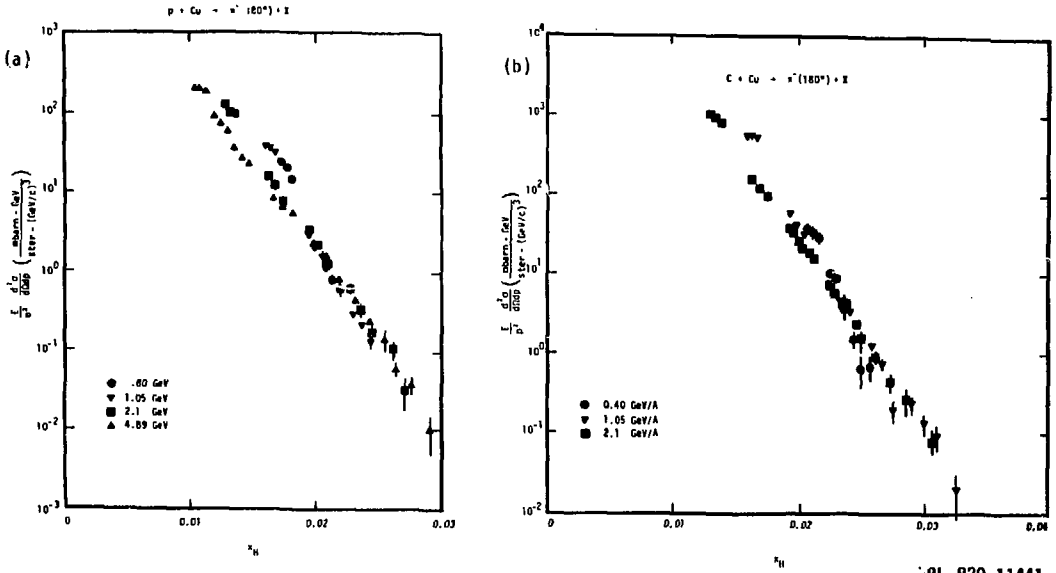

XBL 829-11441

Fig. 27

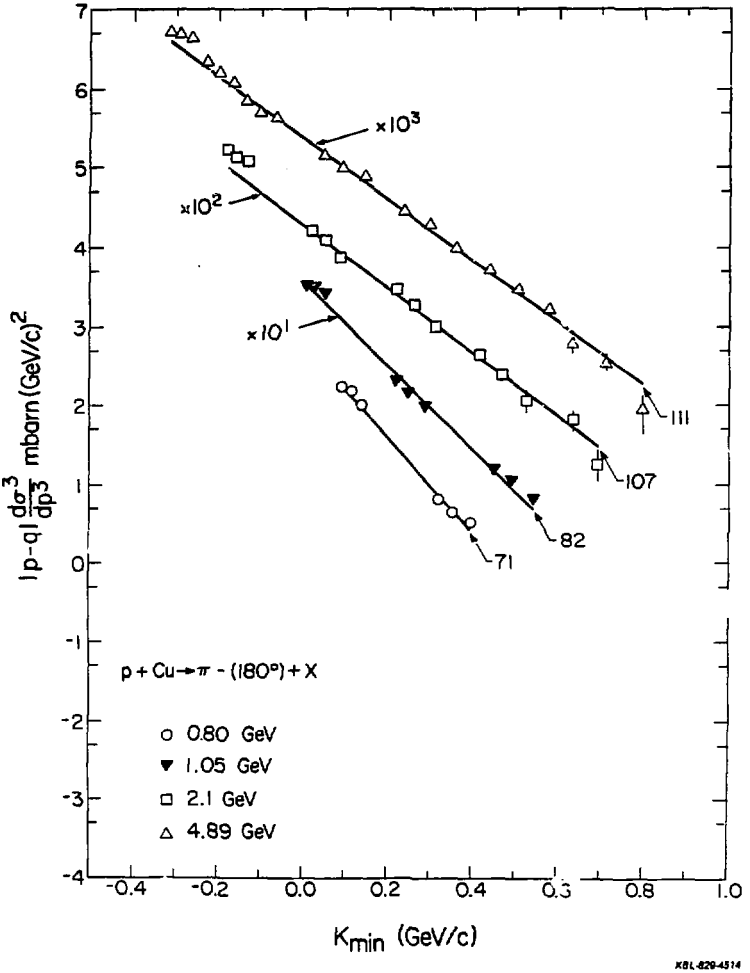
$|p-q| \frac{d\sigma^3}{dp^3}$ mbarn (GeV/c)^2
K_{min} (GeV/c)
$\times 10^3$
$\times 10^2$
$\times 10^1$
111
107
82
71
p + Cu → π - (180°) + X
0.80 GeV
1.05 GeV
2.1 GeV
4.89 GeV
XBL-829-4514

Fig. 28

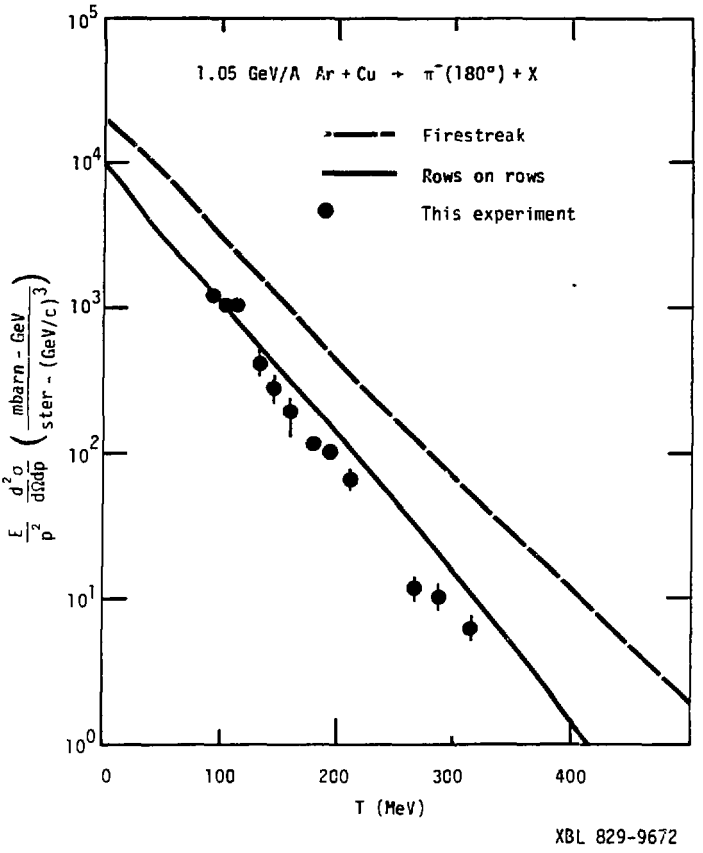
1.05 GeV/A Ar + Cu → π⁻(180°) + X
Firestreak
Rows on rows
This experiment
$\frac{E}{p^2}\frac{d^2\sigma}{d\Omega dp}\left(\frac{mbarn - GeV}{ster - (GeV/c)^3}\right)$
10^5
10^4
10^3
10^2
10^1
10^0
0
100
200
300
400
T (MeV)
XBL 829-9672

Fig. 29

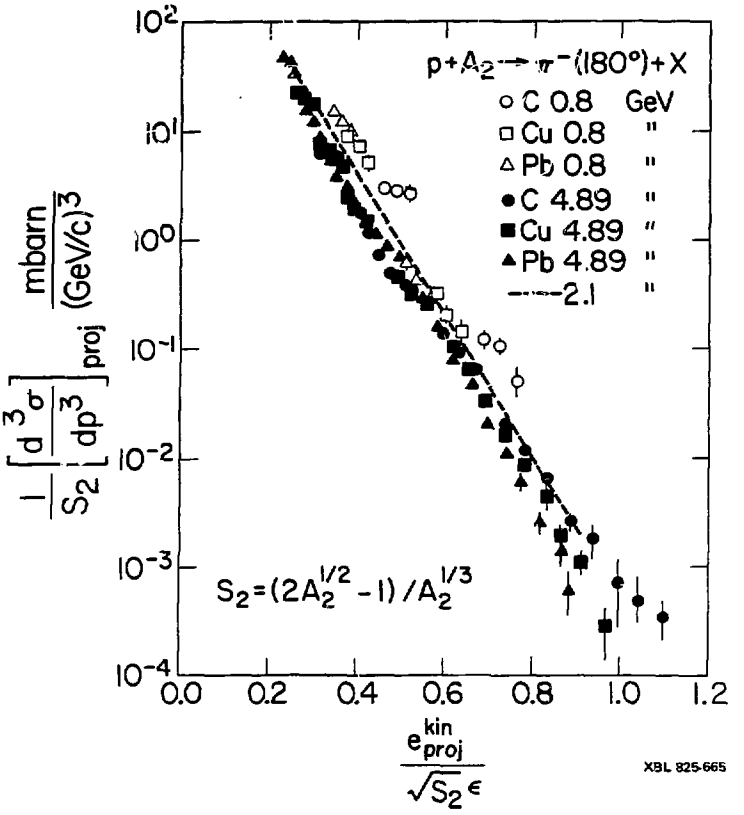
p+A2 → π⁻(180°)+X
C 0.8 GeV
Cu 0.8 "
Pb 0.8 "
C 4.89 "
Cu 4.89 "
Pb 4.89 "
2.1 "
S2=(2A2^1/2 -1)/A2^1/3
mbarn / (GeV/c)³
1/S2 [d³σ/dp³]proj
e^kin_proj / √S2 ε
XBL 825-665

Fig. 30(a)

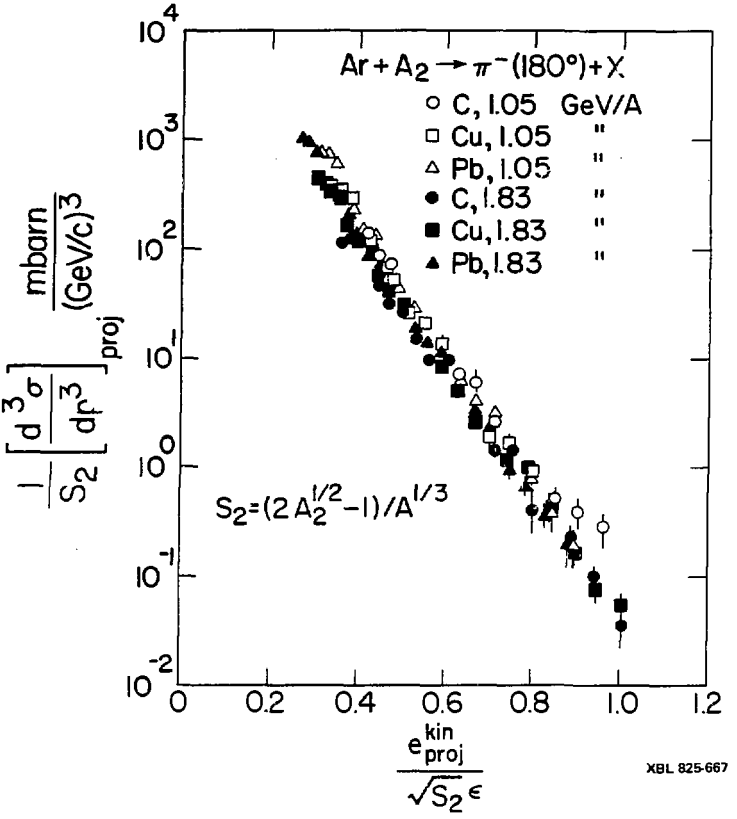
Ar + A2 → π⁻(180°) + X
C, 1.05 GeV/A
Cu, 1.05 "
Pb, 1.05 "
C, 1.83 "
Cu, 1.83 "
Pb, 1.83 "
S2=(2 A2^1/2 − 1)/A^1/3
1/S2 [d³σ/dp³]proj mbarn/(GeV/c)³
e^kin proj / √S2 ε
XBL 825-667

Fig. 30(b)

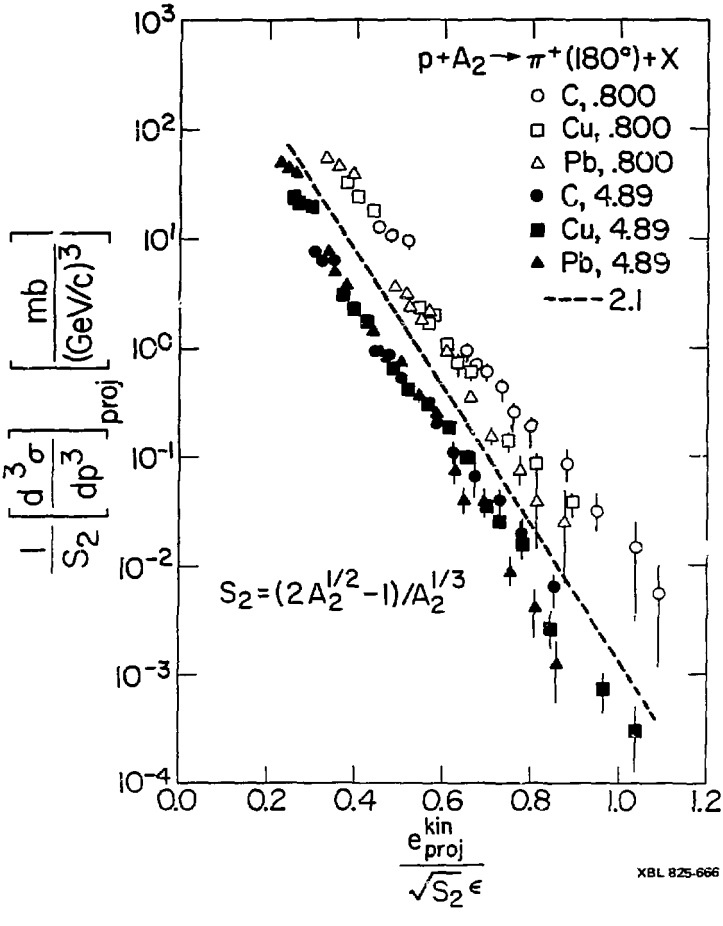
p+A2 → π+(180°)+X
C, .800
Cu, .800
Pb, .800
C, 4.89
Cu, 4.89
Pb, 4.89
2.1
S2=(2A2^1/2-1)/A2^1/3
10^3
10^2
10^1
10^0
10^-1
10^-2
10^-3
10^-4
0.0
0.2
0.4
0.6
0.8
1.0
1.2
1/S2 [d^3σ/dp^3]proj [mb/(GeV/c)^3]
e_proj^kin / √S2 ε
XBL 825-666

Fig. 30(c)

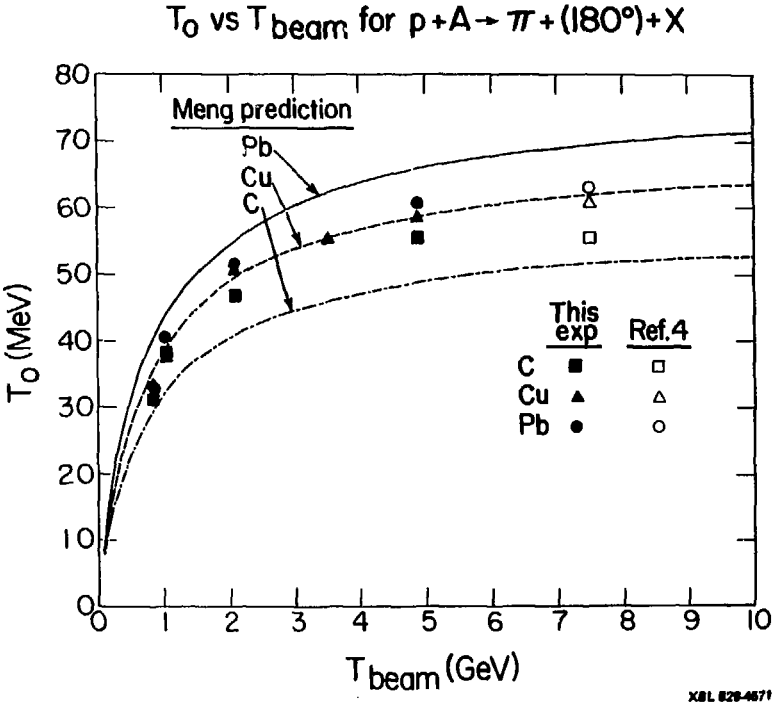

XBL 829-4571

Fig. 31

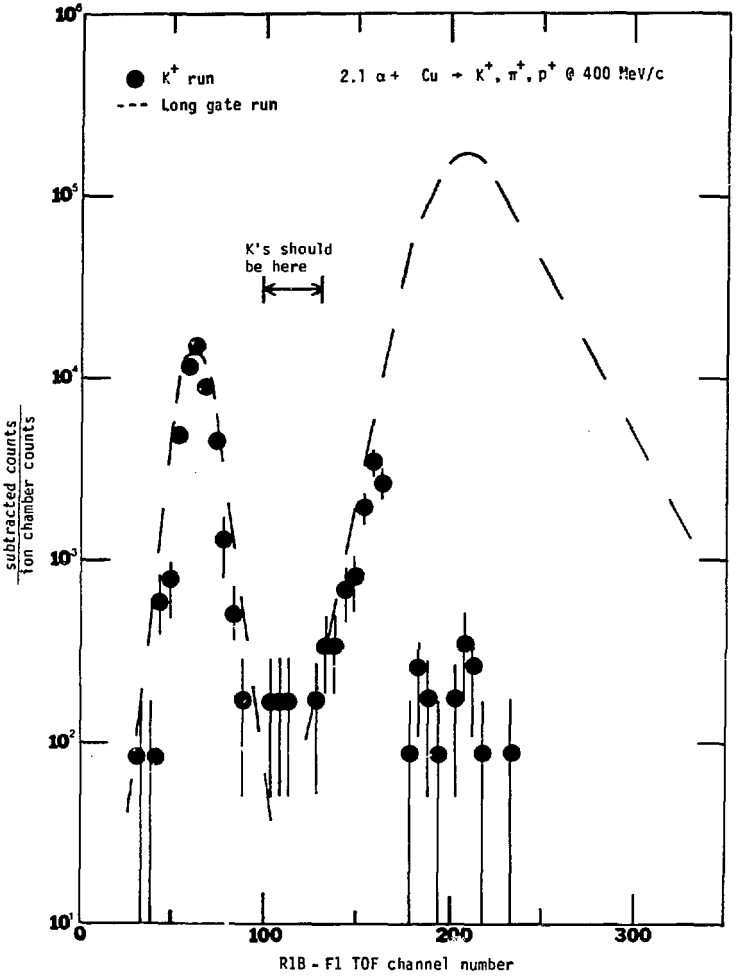

XBL 829-9673

Fig. 32

This report was done with support from the Department of Energy. Any conclusions or opinions expressed in this report represent solely those of the author(s) and not necessarily those of The Regents of the University of California, the Lawrence Berkeley Laboratory or the Department of Energy.

Reference to a company or product name does *not imply approval or recommendation of the* product by the University of California or the U.S. Department of Energy to the exclusion of others that may be suitable.